Physical and numerical modeling of shear resistance of cast-in-place post-tensioned bridge girders

By

ZHELUN ZHANG

DISSERTATION

Submitted in partial satisfaction of the requirement for the degree of

DOCTOR OF PHILOSOPHY

in

Civil and Environmental Engineering

in the

OFFICE OF GRADUATE STUDIES

of the

UNIVERSITY OF CALIFORNIA

DAVIS

Approved:

_____

Sashi K. Kunnath, Chair

_____

John E. Bolander

_____

Dawn Cheng

Committee in charge

2021

Abstract

This research investigates the consequences of two amendments by the California Department of Transportation (Caltrans) of current AASHTO (2017) guidelines related to the determination of the shear resisted by concrete in a post-tensioned (PT) girder containing grouted ducts. Experimental studies by previous researchers have either been limited to small-scale testing or comprise configurations that do not resemble typical Caltrans practice. In this study, load testing to failure of the specimens was carried out on near full-scale cross-sections that represent typical Caltrans PT girders. The experimental testing is further supplemented with numerical simulations to provide additional insight into the effect of grouted ducts in PT girders.

Two large-scale specimens were fabricated to achieve the goals of the project and represented a prototype bridge from the Caltrans bridge inventory. Reinforcing details of the specimen were modified so as to induce shear failure prior to flexural yielding of the specimen. Considerable effort was dedicated to the design of a reaction system so that the imposed loading at shear failure of the specimen could be safely distributed to the strong floor of the laboratory. The primary goal of the first test was to examine the consequence of the Caltrans amendment related to the effective web width in calculating the shear resistance of a PT girder with grouted ducts whereas the second test investigated Caltrans practice of bundling more than three ducts that is currently disallowed in the AASHTO bridge design specifications.

Findings from the experimental testing indicate that the shear resistance of PT girders with grouted ducts have significant reserve strength beyond the AASHTO-predicted shear capacity.

For the specimens tested in this study, the concrete contribution (V_c) to shear resistance varies between 15 – 25% of the nominal shear capacity and the difference in V_c resulting from the Caltrans amendment for establishing the effective width of the web affects the nominal shear capacity of the girder by less than 5% and consequently has a minor effect in the design of PT girders with fully grouted ducts. There was no visible distress around the duct region at the end of testing for specimen #1 indicating that the corrugated metal duct bonds well to the concrete and remains intact even at loads approaching shear failure of the girder. Minor to moderate distress was observed on the concrete surface along the duct lines for specimen #2, which experienced a dramatic shear failure. The inclination of shear cracks for both specimens during testing varied between 25 - 30 degrees, which is slightly lower that AASHTO estimates, with the angle of newly forming cracks tending to decrease with increasing load. These findings are also supported by the numerical simulations of additional girders with varying duct sizes and number of ducts.

Acknowledgments

I wish to thank Professor Sashi K. Kunnath for being my academic advisor throughout my studies at UC Davis and guiding me through the research project. I would like to especially express my gratitude for his confidence in my abilities and devoting significant time and energy to both myself and members of the research team – dealing with the challenges we endured during the pandemic.

I would like to thank Professor John E. Bolander not only for serving on my dissertation committee but also providing technical guidance and valuable advice throughout the project. I also want to thank Professor Dawn Cheng for spending her precious time to serve on the dissertation committee and reviewing my dissertation.

I am grateful to my colleagues Ahmed Al Jasar and Emmanuel Vazquez who contributed to the success of this project and assisted with the heavy burden of fabricating the specimens, helping with the experimental set up and developing the data acquisition system. I would also like to thank my friends who encouraged and supported me during the past seven years: Han Yang, Jin Zhou, HeXiang Wang, Xun Wang, Kanotha Kamau-Devers and Krishen Parmar.

Finally, I want to thank my parents for their constant guidance and the expectations placed on me. Without their support, I would not have the opportunity to study in the US for both my graduate degrees.

The work presented in this dissertation was made possible through funding provided by the California Department of Transportation. I am really honored to have been a member of the research team and contribute to this project.

Table of Contents

List of Figures

List of Tables

1.0 INTRODUCTION

1.1 Background

Box girder bridges have been constructed in California since the early 1950's. Later, with rapid advances in prestressed concrete technology, post-tensioned (PT) multi-cell box girder bridges became more popular given their ability to accommodate wider sections as well as larger spans. Post-tensioning also enables the design of thinner superstructures. Additionally, a continuous bridge girder increases the stiffness of the bridge in the longitudinal direction, and when the columns of continuous bridges are fully restrained at both the superstructure and foundation levels, the moment demands in the column are reduced which in turn can reduce foundation costs. Modern cast-in-place (CIP) PT bridges have much deeper sections than older bridges and also contain multiple PT ducts than used in the past to facilitate the design of bridges with significantly higher design loads resulting from allowances for permit trucks.

An issue that has risen from the issues described above is the need to assess current California Department of Transportation (Caltrans) design procedures, particularly when Caltrans design amendments deviate from current AASHTO (2017) guidelines. Caltrans began developing amendments to the AASHTO LRFD Bridge Design Specifications in 1999 to facilitate adoption of those specifications into California's bridge design practice. Since then, Caltrans has routinely adopted each new edition of the AASHTO LRFD specifications though the Caltrans amendments would supersede corresponding AASHTO provisions. Two specific issues that arise from the Caltrans amendments concern the effective web width for fully grouted ducts and the number of ducts that can be bundled in a girder section. The first of these two issues affects the calculation

of shear strength of the girder member. The research presented in this report addresses both issues through large-scale testing of shear resistance of PT girders and associated numerical simulations.

1.2 Previous Studies

It is now well acknowledged that the shear capacity of concrete girders can be estimated using the modified compression-field theory (MCFT) proposed by Collins et al. (2008). The theory has been validated by both laboratory and field testing of bridge girders. Due to the way MCFT considers the shear behavior of cracked concrete, an iterative process is required to establish the shear capacity of the critical girder cross-section, involving equilibrium equations, strain compatibility, and material constitutive relationships (Vecchio and Collins 1986). To address the needs of engineering practice, a simplified non-iterative version of MCFT was introduced by Bentz, Vecchio, and Collins (2006) for assessing shear capacity of concrete members. The non-iterative procedure for shear design of PT girders is specified in AASHTO (2017) and adopted with modifications by Caltrans. Details of the AASHTO specifications and Caltrans amendments are presented in the next section of this report.

While Caltrans adopts most of the AASHTO (2017) provisions for design of bridges, one of the Caltrans amendments related to the effective width of cast-in-place fully grouted PT girders has not been evaluated by independent experiments. The presence of the duct(s) in the web of a girder may have an influence on the strength of the section. Whereas this effect is generally negligible for the bending and axial compressive strength of post-tensioned girders, the consequence of the duct on the shear strength of the section is not well understood. The AASHTO specifications, based on testing reported in the literature, acknowledge that the presence of a prestressing duct may reduce the diagonal compressive strength of the web and that this reduction

may be indirectly incorporated into the design process by assuming a reduced web width, termed the effective web width. Current AASHTO specifications for the effective web width are based primarily on simple compression tests on panels carried out in the US, Canada and Europe. These tests suggest the presence of PT ducts can negatively effect the shear capacity of the section. The effect of the PT ducts were generally assessed using the following ratio:

$$\delta = \frac{\sum \phi_d}{b_w} \tag{1.1}$$

Where $\sum \phi_d$ is the sum of diameters of the PT ducts at the same level and b_w is the full width of the girder web. The presence of PT ducts was shown in panel testing (Campbell et al. 1979) to influence the shear capacity of the girder, particularly for large values of δ (usually much larger than 0.2).

The basis for panel testing to study the influence of PT ducts can be traced to the well-known truss analogy for a reinforced concrete beam subjected to shear, wherein it is assumed that following the development of diagonal tensile cracking, the concrete in the web functions as the diagonal strut of a truss system (Figure 1 a). Hence the web crushing strength of a beam, which is governed by the strength of the diagonal compressive members, is related to the compressive strength of the web concrete. Many investigators (Leonhardt, 1969; Campbell and Batchelor, 1981; Muttoni et al. 2006; Ruiz and Muttoni, 2008; Wald 2012) have thus used plain concrete prisms loaded in axial compression, as shown in Fig. l b, to simulate the behavior of the diagonal strut.

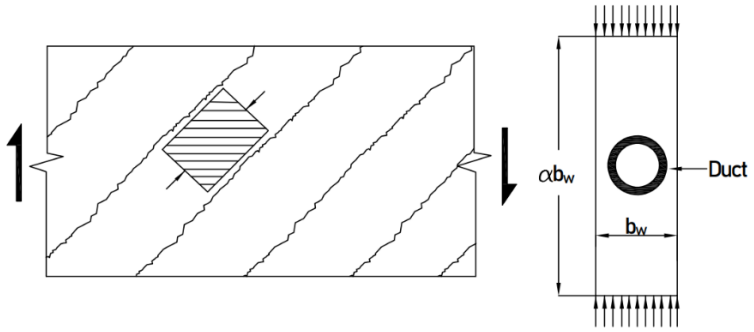

Figure 1.1 Assessing the influence of ducts in post-tensioned members

Leonhardt (1969) tested as many as 52 panels, including some with a lateral eccentricity of the duct as well as varying duct angles, and recommended expressions for the effective web width b_e in the presence of ducts as follows:

$$b_e = b_w - \sum \phi_d \qquad \text{for ungrouted ducts} \qquad (1.2\text{ a})$$

$$b_e = b_w - \frac{2}{3}\sum \phi_d \qquad \text{for grouted ducts} \qquad (1.2\text{ b})$$

The two parameters, i.e. duct eccentricity and duct inclination, were found to have little influence on the strength of the tested panels.

Campbell and Batchelor (1981) analyzed data from tests carried out on axially loaded concrete prisms at the Cement and Concrete Association (C & CA), England and at Queen's University, Canada. In both test programs, the prisms had a square cross section. Most of the prisms tested at Queen's University had a 6 in. x 6 in. (152 mm x 152 mm) cross section. All prisms in the C & CA tests had cross-sectional dimensions of 100 mm. The height to width ratio of the prisms α was 5 in the C & CA tests and 3 in the Queen's University tests. They used a nonlinear fit to the experimental data and proposed the following expression for the effective web width for grouted ducts:

$$b_e = b_w - \frac{1}{3}\phi_d - \frac{1}{2}\frac{\phi_d^{\,2}}{b_w} \tag{1.3}$$

For ungrouted ducts, a modified form of the above expression was suggested:

$$b_e = b_w - 2\phi_d - \frac{\phi_d^{\,2}}{b_w} \tag{1.4}$$

The above expressions assume a single duct at a given level, however, it is assumed that $\sum \phi_d$ should be used when multiple ducts are placed at the same level. More importantly, they also noted that concrete prisms containing transverse ducts and loaded in axial compression do not simulate accurately the behavior of a beam web that is in diagonal compression. Prism tests, they concluded. give an effective web width less than that from beam tests and, therefore, lead to conservative predictions of strength. They also recommended that web crushing strength be computed using a variable angle truss model rather than the 45 degree angle implied in the prism-based testing. These findings by Campbell and Batchelor are significant in the context of examining the Caltrans amendments of the AASHTO specifications for the estimation of the effective web width.

Muttoni et al. (2006) examined the behavior of web girders with PT ducts using both steel and high-density polyethylene (plastic) ducts. They carried out tests on 12 specimens cast in the laboratory and 4 panels cut from an existing bridge with dimensions of approximately 24 x 24 x 5 in (600 x 600 x 125 mm) to investigate the effect of the presence of various types of post-tensioning ducts on the strength of the shear-induced compression struts. An additional aspect of the influence of the presence of PT ducts presented in the study, that was also alluded to in the research by Leonhardt (1969), was the disturbance in the flow of stresses introduced by the ducts.

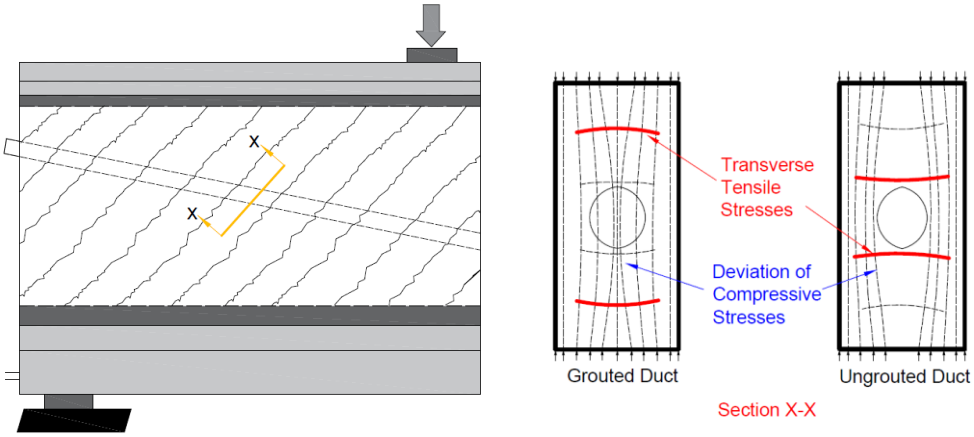

Figure 1.2: Effect of presence of ducts in webs on the compressive stress field (Leonhardt 1969, Muttoni et al. 2006).

As shown in Figure 1.2, the deviation of the compressive stress flow around the ducts results in the development of tensile stresses which may cause a reduction in shear strength compared to a cross-section without a PT duct within the web of a girder. The results of this study showed that the use of grouted plastic ducts resulted in as much as a 40 percent reduction in strength compared to similar panels containing grouted steel ducts. These findings had a direct impact on Eurocode provisions resulting in a drastic reduction is shear strength estimations of the code equations for grouted plastic post-tensioning ducts. However, some researchers argue that this may not be justified as the small-scale panel tests were never verified with full-scale post-tensioned beam tests on girders with plastic post-tensioning ducts.

Ruiz and Muttoni (2008) investigated the strength of thin-webbed PT beams where failure resulted from web crushing. As suggested in the previous study by Muttoni et al. (2006), it was assumed that the shear strength in these members was reduced because of the state of cracking in the web and due to the disturbance in the flow of stresses introduced by the PT ducts. Based on the results of six full-scale tests performed on actual prestressed beams extracted from a girder

bridge, it was found that the average shear capacity of the beams was approximately 15% higher than the AASHTO predicted capacity. Failure by concrete crushing in the post-tensioned girders was accompanied by spalling of the concrete cover along the duct. The spalling of the cover led to significant tensile stresses in the concrete cover. However, no spalling was observed in the panel testing indicating the difficulty in correlating panel tests to actual beam tests.

Moore et al. (2015) evaluated the strength and serviceability of post-tensioned girders loaded in shear by investigating how a post-tensioning duct located in the web of a girder affects the shear transfer mechanism of a bulb-tee cross-section. Eleven tests were performed on full-scale bulb-tee post-tensioned girders – of these tests, ten were conducted on specimens that contained a post-tensioning duct within their web and additional pre-tensioning reinforcement in their bottom and top flanges and the remaining shear test was conducted on a control specimen that did not have a posttensioning tendon but contained the same pre-tensioning reinforcement as the post-tensioned girder specimens. The five primary experimental variables included: the presence of a post-tensioning duct, post-tensioning duct material (plastic or steel), web-width, duct diameter, and the transverse reinforcement ratio. Based on findings from the experimental study, they conclude that there was no significant difference in the ultimate or service level shear behavior in girders containing plastic grouted ducts when compared to those containing steel grouted ducts and that the current procedure of reducing the effective web width to account for the presence of a post-tensioning duct is ineffective because it addresses an incorrect shear transfer mechanism. Since the observed failure mode of the vast majority of tests (which included specimens tested by other researchers) was the crushing of compression struts, Moore et al. suggest a shear strength reduction

factor in the current AASHTO procedure that reduces the transverse reinforcement contribution to shear strength (V_s) and consequently removes the 0.4 limit on the duct diameter-to-web width ratio. The proposed expression for shear strength provided by the vertical stirrups is as follows:

$$V_s = \frac{\lambda_{duct} A_v f_y d_v \cot\theta}{s} \tag{1.5}$$

$$\lambda_{duct} = 1 - \delta\left(\frac{\phi_{duct}}{b_w}\right)^2 \tag{1.6}$$

In the above expression, A_v is the area of the transverse reinforcement, f_y is the yield strength of the transverse reinforcement, d_v is the effective shear depth measured perpendicular to the neutral axis between the compressive and tensile resultants due to flexure subject to the condition that it not be less than the greater of *0.9 x* (transformed steel area's depth) or 0.72 *h*, θ is the angle of inclination of the diagonal compressive stresses, *s* is the spacing of the transverse reinforcement, δ is a factor set equal to 2.0 for grouted ducts based on the calibration of Equation (1.6), ϕ_{duct} is the duct diameter and b_w is the width of the web. All units are in psi and inches. The authors indicate that the revised expression provides a better estimate of shear capacity for girders with grouted ducts.

1.3 AASHTO-Based Shear Design of Bridge Girders

An overview of the shear design procedure adopted in AASHTO (2017) is summarized in this section followed by a discussion of the Caltrans amendments so that the research context is better understood. The review is limited to so-called B-regions where the Bernoulli hypothesis of plane sections is valid and forms the basis for the design of shear reinforcement at an appropriate distance

away from supports or other discontinuities. The critical section at which shear failure is expected to initiate is assumed to lie within a B-region. The nominal shear resistance V_n is estimated as:

$$V_n = V_c + V_s + V_p \quad \leq \quad 0.25 f_c' \, b_v d_v \tag{1.7}$$

where:

$$V_c = 0.0316 \beta \lambda \sqrt{f_c'} \, b_v d_v \tag{1.8}$$

$$V_s = \frac{A_v f_y d_v \cot \theta}{s} \text{ (for vertical stirrups)} \tag{1.9}$$

V_p = component of prestressing force in the direction of the shear force, which is positive if resisting the applied shear

b_v = effective web width, as discussed later

d_v = effective shear depth as discussed in the previous section

β = factor indicating ability of diagonally cracked concrete to transmit tension and shear as discussed below

λ = concrete density modification factor, which is set to 1.0 for normal weight concrete

The effective web width b_v is determined from:

$$b_v = b_w - k \cdot \phi_{duct} \tag{1.10}$$

where b_w is the gross web width, *k* is the web width reduction factor to account for the presence of ducts. AASHTO stipulates a value of *k* = 0.25 for grouted ducts and 0.5 for ungrouted (or empty) ducts. The AASHTO reduction factors are based primarily on the findings by Muttoni et al. (2006) and Ruiz and Muttoni (2008). However, researchers have questioned the validity of such a

reduction based on simple panel tests that do not account for numerous factors that influence the response of full-scale post-tensioned girders.

The Caltrans amendment to the AASHTO procedure allows for the computation of the shear resistance of post-tensioned concrete girders to be based on assuming $b_v = b_w$ or $k = 0$. It is clearly of interest to bridge engineers on whether the Caltrans amendment is a safe and reasonable assumption for the design of CIP-PT box girders.

1.4 Objectives of Study

The primary objective of the proposed research is to provide a basis for rational and accurate estimation of the shear resistance of CIP-PT box girders. This objective will be accomplished through a combined experimental and numerical study that investigates the shear resistance of CIP-PT girders that contain different sizes and arrangements of grouted ducts. As noted previously, the Caltrans amendments currently allows for deviation from AASHTO requirements on (a) the effective width of the web containing grouted ducts when estimating the shear capacity of the girder, and (b) number of ducts that can be bundled.

The proposed research study will provide insight into the shear resistance of cast-in-place post-tensioned box girders and the influence of multiple ducts on the shear capacity of the girders. Research findings can be used to assess the difference between Caltrans and AASHTO provisions for determining the shear capacity of a PT box girder as well as optimize the web thicknesses of the bridge girders – the former will justify continuation of the Caltrans amendments to current AASHTO specifications while the latter will minimize construction costs.

While there are several experiments reported in the literature examining the shear capacity of post-tensioned girders, most of them are either small-scale tests or comprise configurations that

do not resemble typical Caltrans practice. Hence it was of critical importance that the testing to evaluate the shear capacity of the PT girder be carried out on large-scale or near full-scale cross-sections that represent typical Caltrans girders. Additionally, given the high cost of large-scale testing, it is necessary to supplement the experimental testing with numerical simulations wherein the numerical models have been validated against response data from the experiments.

1.5 Scope of Work

The research objectives will be accomplished through a combination of large-scale experiments and nonlinear finite element simulations. The main tasks to be undertaken to achieve the project objectives are summarized below:

(a) Selection of prototype bridge – This task is critical to the project since the goal is to test a specimen whose depth represents either a full-scale or near full-scale bridge girder. The effects of using a scaled model in the context of investigating shear capacity is not fully known. Once a prototype bridge is identified, the development of an appropriate test specimen should consider a configuration that induces shear failure prior to flexural yielding of the specimen.

(b) Design of the experimental setup – Considering the physical constraints in the laboratory, it is essential that the test of the selected prototype bridge girder can be accomplished wherein the girder fails under the imposed shear. This task includes the design of the reaction system subjected to the limitations of the strong floor in the laboratory.

(c) Preliminary test of girder to validate Caltrans shear design – The first test will be performed on a section of the selected prototype girder representing an interior support of a multi-span bridge. The cross-section of the girder will be at full-scale. The load-displacement response

will be recorded and the shear in the critical section at failure will provide information on the margin of safety against the code-based design. Furthermore, findings from this first phase of testing will establish the validity of the Caltrans amendment related to the effective web width in calculating the shear resistance of a PT girder.

(d) Phase 2 test to verify Caltrans practice of allowing bundled ducts – An additional Caltrans amendment that will be investigated is the effect of allowing more than 3 ducts in the cross-section that is currently disallowed by AASHTO. Caltrans is also interested in reducing the web width from 12” (standard current practice) to 10”. Hence it was decided that the phase 2 test would incorporate 4 ducts within a 10” web.

(e) Numerical simulations to supplement experimental testing – While the two large-scale tests may provide confidence in the current state of practice for shear design of cast-in-place PT girders, additional data to further corroborate the experimental findings will be generated through numerical simulations using detailed finite element analysis of PT bridge girders with varying duct diameters as well as different configurations of bundled ducts.

2.0 DESIGN OF EXPERIMENTAL STUDY

Two large-scale experiments were carried out in the structural testing facility at UC Davis to accomplish the goals of the project. There were numerous challenges in developing the test program since detailed specifications of the strong floor were unavailable and no prior tests of similar large-scale specimens have been carried out at the facility. Preliminary load testing was conducted on the strong floor to establish a basis for the ultimate load carrying capacity of the floor. This was followed by numerical simulations to confirm the ability of the strong floor to facilitate the proposed testing at loads that induce shear failure in the specimen. In this chapter, the selection of the prototype specimens and the design of the reaction system is described.

2.1 Selection of Prototype Bridge

Several drawings of existing cast-in-place post-tensioned box girder bridges in the Caltrans inventory were reviewed. Eventually, a widening project of an existing bridge was selected as the prototype bridge. The selection of the bridge was dictated primarily by the constraints in the laboratory which limited (a) the maximum depth of the specimen; and (b) the maximum force to be exerted on the strong floor through the distribution beams that transferred the reaction forces. An elevation view of the bridge is shown in Figure 2.1. The total depth of the girder is 5 feet which is the maximum possible dimension that can be constructed and tested in the lab due to limitations imposed by the ceiling height and the presence of ceiling-mounted devices in the laboratory. Additional details of the girder section including the reinforcement are displayed in Figure 2.2. The center-to-center distance between the two internal webs is 91 inches. The specimen to be tested will preserve the full specimen height and web width though the flange

width will be reduced. The placement of additional reinforcement in the reduced flange sections will ensure that the original flexural capacity is retained.

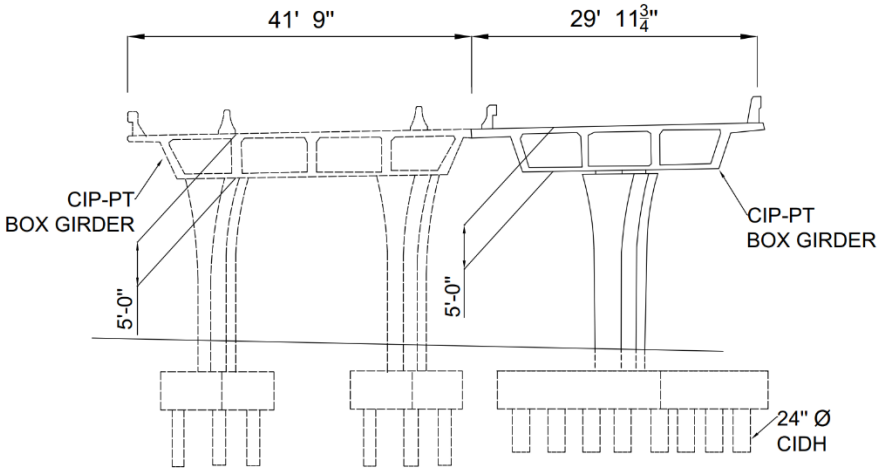

Figure 2.1: Elevation view of selected prototype bridge

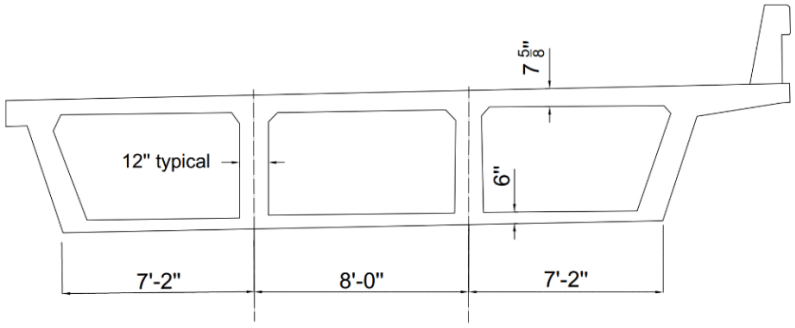

(a)

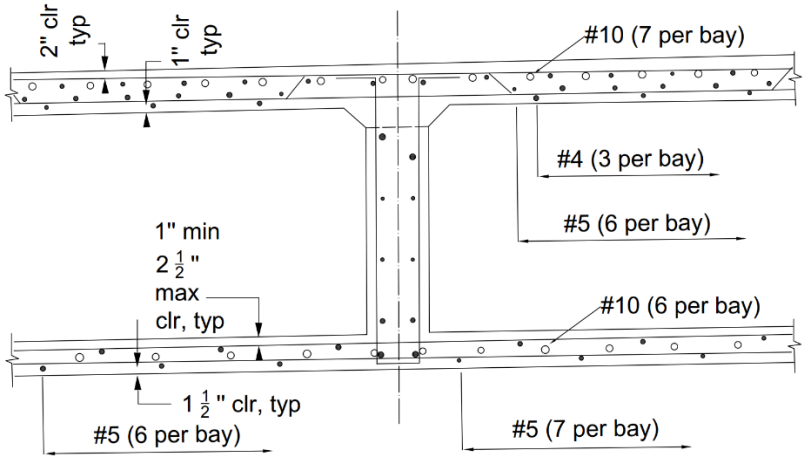

(b)

Figure 2.2: Girder cross-section: (a) overall configuration; (b) reinforcement details

2.2 Specimen #1: Full-Scale Model Details

The prototype bridge consists of two spans with the right span (~ 120 ft.) being slightly longer than the left span (~ 100 ft.). A cross-section of the girder along the span lengths is shown in Figure 2.3 which also shows the profile of the PT tendons. The section considered for the experimental testing is the region over the interior bent as shown in the figure. This region will experience negative bending under gravity loads and the tendons across a 32-feet longitudinal section will be nearly horizontal. Hence, a straight horizontal tendon was used for the laboratory specimen.

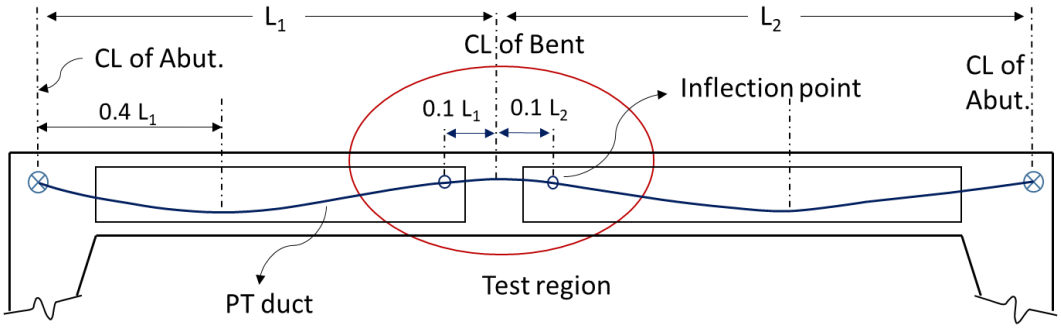

Figure 2.3: Longitudinal section through girder showing PT tendon profile

As previously indicated, the design of the test specimen was dictated by the constraints in the structural testing facility on campus. Figure 2.4 shows the plan view of the laboratory where the strong floor is identified on the left section. The strong floor area is 600 sq. ft. (30 x 20 ft.) and is equipped with five steel tracks (each composed of two parallel railroad rails) to provide a tie-down capacity of approximately 50 kips/ft. Based on the expected shear capacity of the girder, it was essential that the reaction system be designed to distribute the applied load to the strong floor through distribution beams. The overall length of the girder specimen was 32 ft.

(allowing an overhang of 1 feet on either side of the 30 ft. steel rails) with a center-to-center distance between supports of 30 ft.

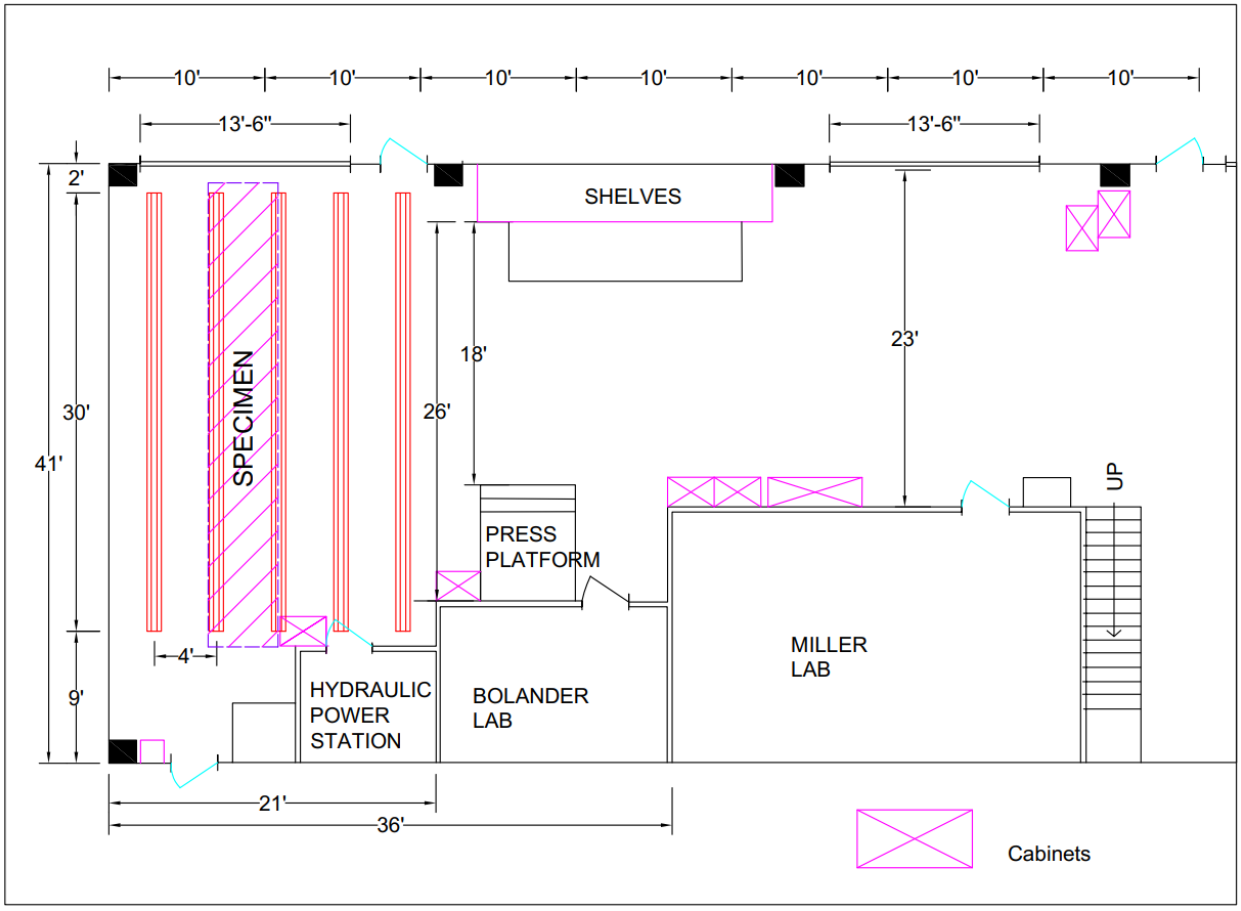

Figure 2.4: Structural testing facility at UC Davis showing strong floor on left

Under the constraints discussed above, a girder specimen was designed with the objective of inducing shear failure in the B-region to the left of the load application point (Figure 2.5). The specimen cross-sections were varied across the length to create two distinct regions: a region that represented the typical prototype girder with shear reinforcement that would yield under the imposed loading and adjacent regions with significantly higher shear reinforcement to preclude shear yielding. Shear yielding is expected to occur only in the region corresponding to Section

B-B. Sections A-A, C-C and D-D are designed with wider webs to ensure that they remain essentially undamaged prior to shear yielding in Section B-B. Complete details of the final girder specimen are illustrated in Figure 2.5. Sectional and reinforcement details of the other cross-sections are shown in Figures 2.6 and 2.7, respectively.

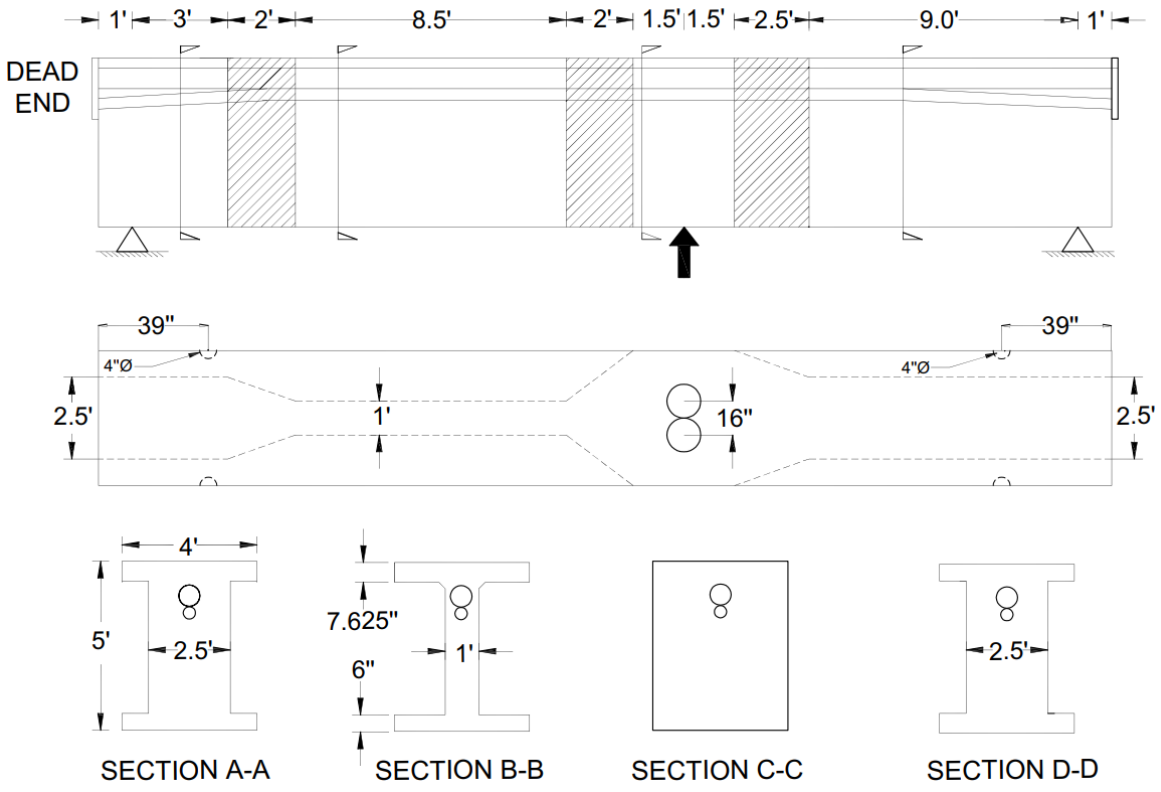

Figure 2.5: Dimensional details of girder specimen #1

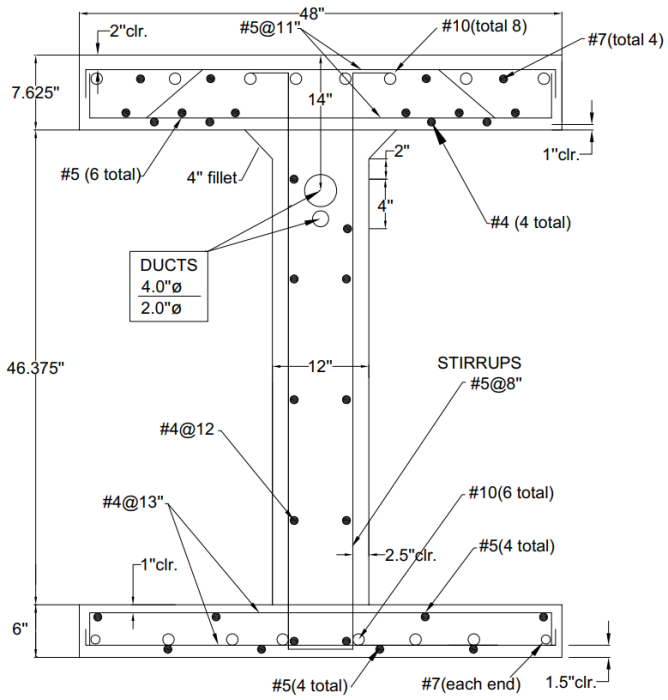

Figure 2.6: Reinforcement details at critical section B-B

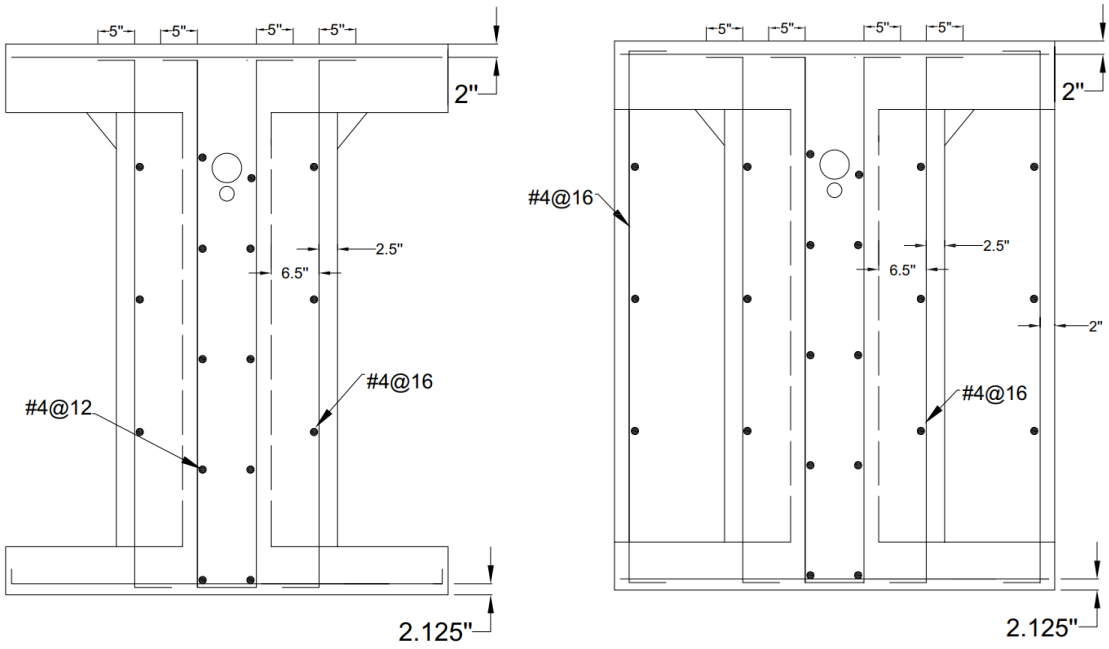

(a) (b)

Figure 2.7: Reinforcement details at (a) Section A-A and (b) Section C-C

2.2.1 Post-Tensioning Force

All cast-in-place box girders in California are post-tensioned (PT) which involves installing and stressing the tendons after the concrete has been placed, cured and hardened. Ducts are placed inside the concrete so that the tendons can be threaded through them after the concrete hardens. Once in place, the tendons are tensioned by jacks and anchored against the hardened member using anchorage devices cast into the concrete. Since the region under consideration in the present study is the negative moment region across a support and the girder dimension along the span is only 16 feet on either side of the support, the tendon is expected to be nearly horizontal. The actual PT forces applied are displayed for 29 typical California box-girder bridges in Figure 2.8. The resulting stress in the cross-section varies from a minimum of 0.1 to a maximum of 0.3 f_c, where f_c is the design compressive strength of the concrete, A_g is the gross cross-sectional area, and F is the applied prestressing force. In the present study, the target PT force was based on the average of these axial stress limits.

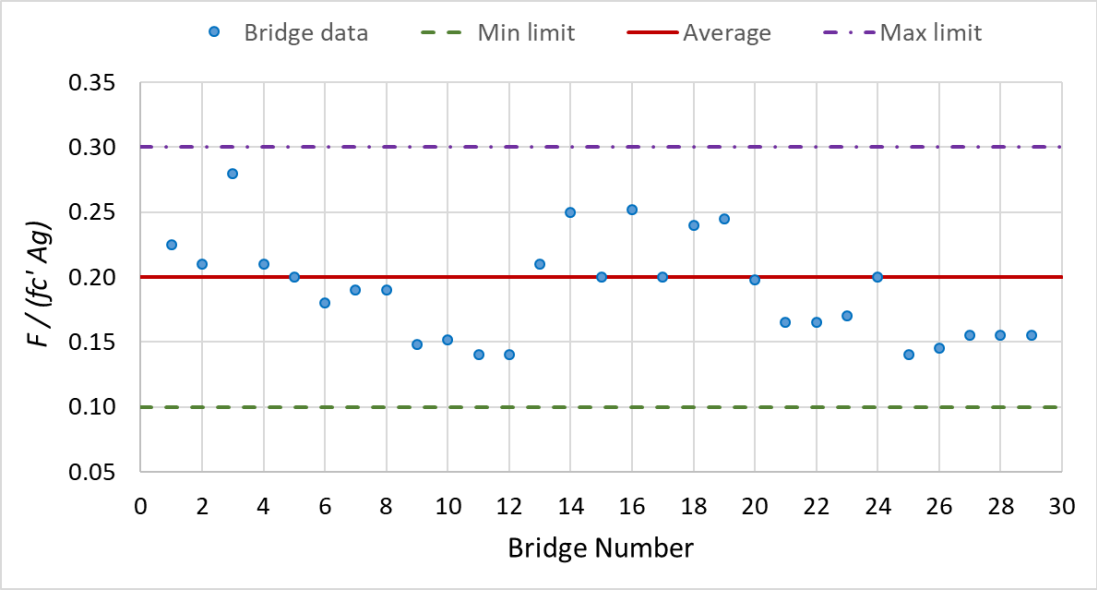

Figure 2.8: Typical post-tensioning stresses in California bridges

2.2.2 Construction and Instrumentation

The finalized girder specimen shown in Figure 2.5 was cast in-place on the strong floor of the structural testing facility at UC Davis. Figure 2.9 and 2.10 shows various stages of the formwork construction. In both figures, the PT ducts are visible. The top duct with a diameter of 4.5" is the primary duct comprising 26 strands whereas the 2" duct below contained a single strand. Based on cylinder tests, the concrete strength at the time of post-tensioning was 4.2 ksi. Hence the projected jacking force to attain the average axial stress of 0.2 f_c (Figure 2.8) was 1020 kips. The formwork was constructed to facilitate an effective concrete pour that avoids air pockets in the web and lower flange. The lower flange was fully exposed as evident in Fig. 2.9 to allow for vibration and compaction during the pour. The top flange is shown in Figure 2.10.

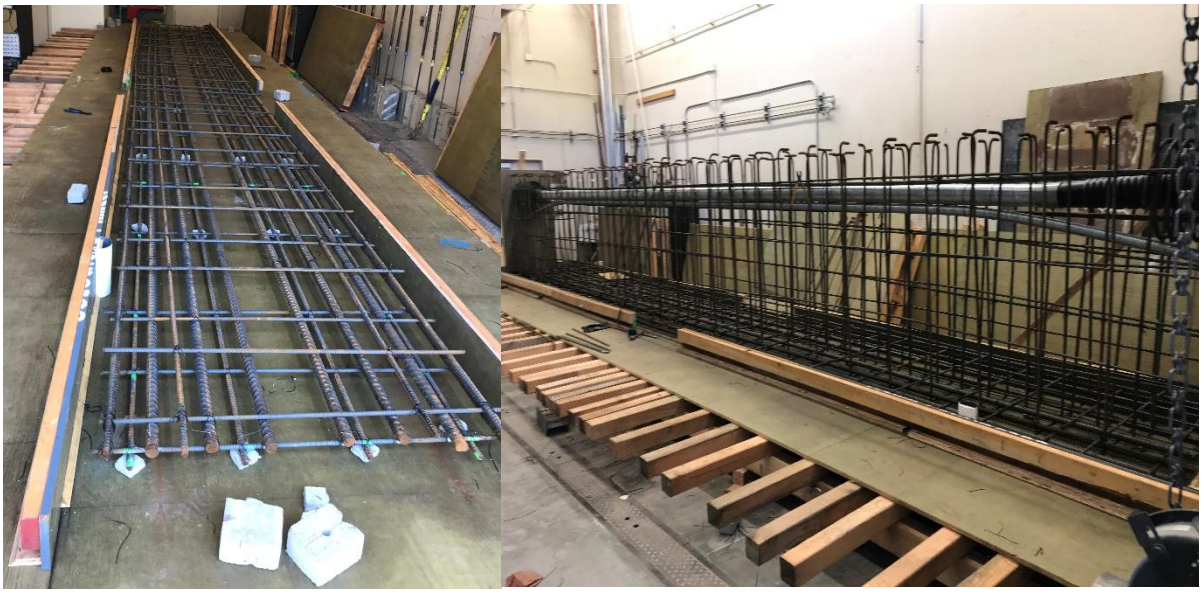

Figure 2.9: Initial stages of formwork construction for specimen #1

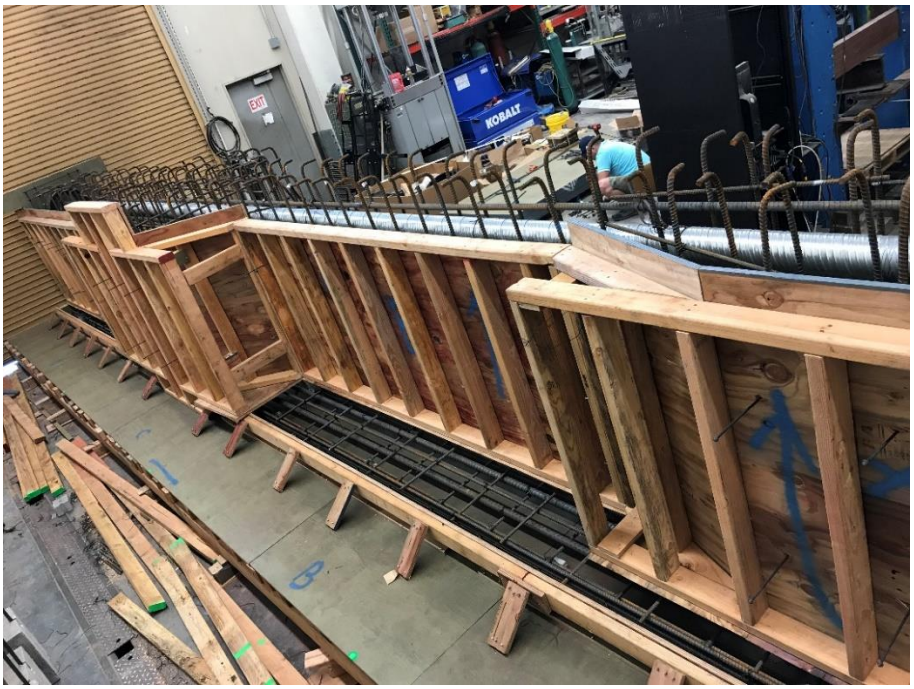

(a)

(b)

(c)

Figure 2.10: Formwork construction for specimen #1

The specimen was instrumented with nine strain gauges – five on the shear reinforcement in the critical region and four on longitudinal reinforcement. The strain gauge locations are identified in Figure 2.11. The gauges on the shear reinforcement were installed to monitor yielding of the stirrups whereas the gauges at P1 and P2 would provide data to estimate the strain at the centroid of the tension reinforcement (a critical quantity in the estimation of the shear strength of the section using AASHTO bridge design specification). Additionally, displacement transducers (LVDTs) were installed at three locations as shown to monitor movement under the supports and at the centroidal location of the applied load.

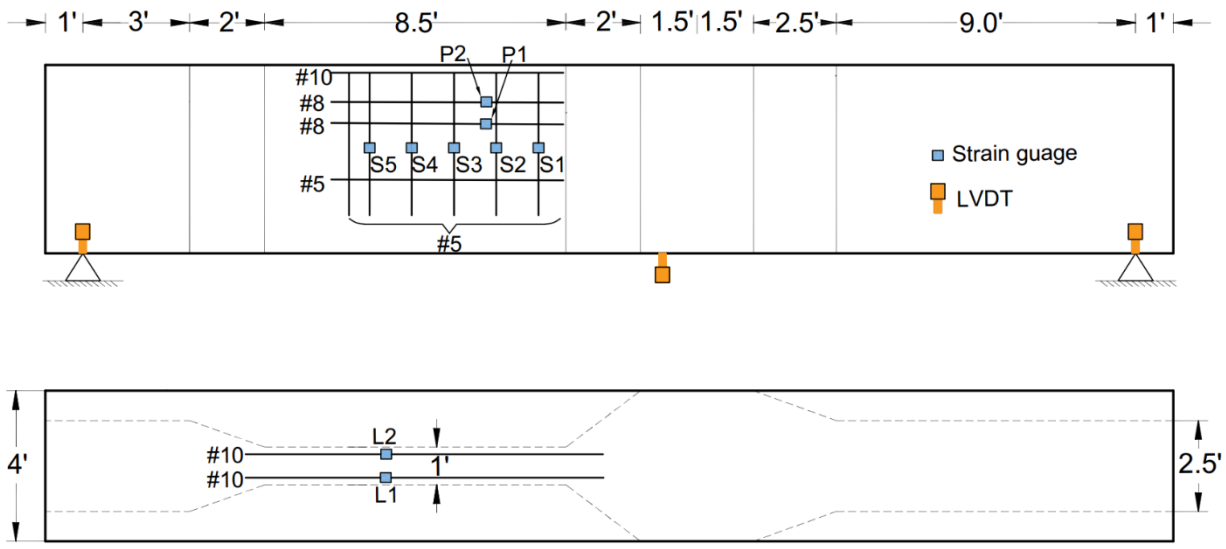

Figure 2.11: Location of strain gauges and LVDTs in specimen #1

The Caltrans-approved concrete mixture with a target compressive strength of 3600 psi is shown in Table 2.1. The mixture includes 1.5% entrained air and a water : cementitious materials ratio of 0.47. Data provided by the concrete supplier on this mixture indicates an average strength of 4760 psi with a standard deviation of 410 psi.

Table 2.1: Concrete mixture (for 1 cubic yard) used in specimen #1

Material	*Specific Gravity*	*Volume (ft^3/yd^3)*	*Quantity ($lb./yd^3$)*
Coarse aggregate	2.68	10.46	1750
Fine aggregate	2.63	8.37	1373
Portland cement	3.15	2.11	415
Fly ash (ASTM C 618)	2.38	1.18	175
Water	1.00	4.48	279.4

The required concrete for the specimen alone was approximately 15 cubic yards. When considering additional concrete for cylinder testing and making an allowance for waste, the total

quantity of concrete ordered for the pour was 16 cubic yards. Hence the concrete was supplied in two trucks. Photographs taken during the concrete pour are displayed in Figure 2.12. Concrete cylinders were cast from both batches. Table 2.2 summarizes the evolution of concrete strength in both batches (based on the average of 3-cylinder tests) until the day of testing. Though the concrete strength varied considerably between the two batches, it was still within the standard deviation of the mean strength provided by the concrete supplier for the selected mixture design.

Table 2.2: Evolution of compressive strength of concrete used in specimen #1

Age at test (days)	**Batch 1**	**Batch 2**	**Average**
	f_c' (psi)	f_c' (psi)	f_c' (psi)
3	2007	2802	2405
7	3599	3493	3546
21	3860	4297	4005
28	4293	4226	4270
Day of test	4881	5517	5199

(a)

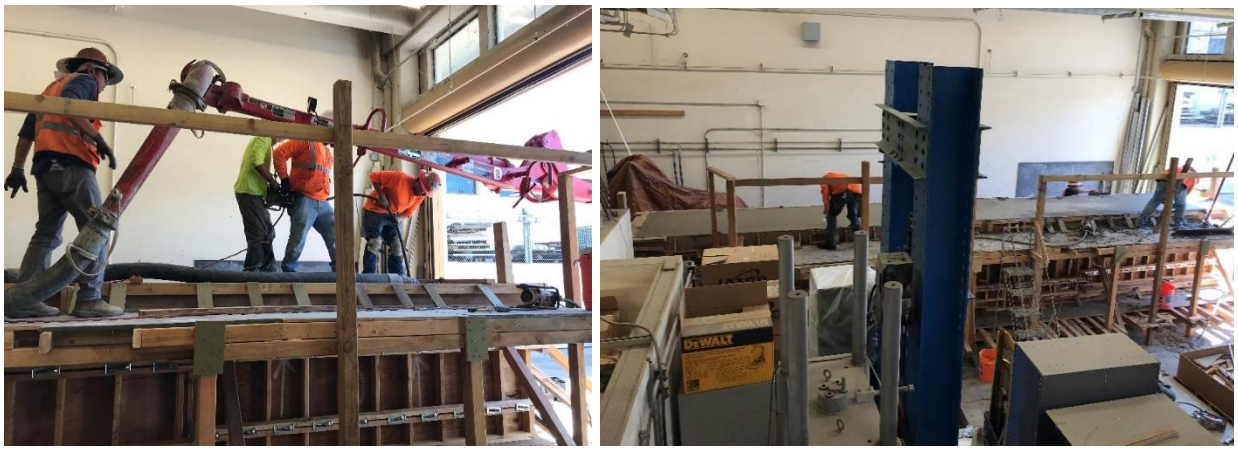

(b) (c)

Figure 2.12: Concrete pour (specimen #1)

Forms were stripped approximately 1 week after the pour. The effectiveness of the casting operation and formwork design is shown in Figure 2.13 (a) where the specimen is seen to be free of any air pockets or delamination. Based on the concrete strength requirements for post-tensioning, it was evident from the cylinder tests that the specimen was ready for post-tensioning after 21 days. Post-tensioning of the specimen was carried out on Day 24 after the pour. Cylinder tests carried out on the day of post-tensioning indicate a concrete compressive strength of 4200 psi.

To achieve the target average post-tensioning (PT) stress of 0.2 f_c, the required PT force was 1018 kips. In order to allow for losses due to anchor set, the jacking force applied on the specimen was 1186 kips. Figure 2.13 (b) shows the 26 strands placed in the main 4.5 inch duct as well as the equipment used to simultaneously apply the PT forces on the tendons. At the total jacking force of 1186 kips, the elongation of the tendons was measured to be 2.625 inches. The elongation at anchor set was 2.375 inch which resulted in an effective jacking force of 1020 kips.

A single strand was placed in the lower 2” duct and stressed to $0.7 f_{pu}$ = 189 ksi, where f_{pu} is the ultimate strength of the prestressing steel. After applying the PT forces, the ducts were grouted with a cement paste in accordance with Caltrans specifications. Tests on 2” x 2” cubes indicated an average strength of 8050 psi on the day of load testing of the girder.

(a)

(b)

(c)

Figure 2.13: Post-tensioning operation (specimen #1)

Following the successful post-tensioning of the specimen, the services of a professional moving and handling company was utilized to raise the specimen and place it on concrete support blocks (Figure 2.14 a). Recalling specimen details from Figure 2.5 where the load is to be applied upwards to simulate the negative moment across a support, heavy reaction beams were placed at the ends of the beams to simulate support conditions. Additional details on the design of the reaction system are outlined in Section 2.4. The reaction beams are tied to the strong floor of the laboratory using high strength rods connected to distribution beams. Each reaction beam is connected to four floor distribution beams (only two of these beams are visible on one side of the specimen in Figures 2.14 b and c), which in turn are tied to the strong floor of the laboratory through high-strength DYWIDAG bars.

(a)

(b)

(c)

Figure 2.14: Specimen #1 prior to testing

(a) Girder on support blocks; (b)Reaction beam on top and distribution floor beam at bottom to the left of specimen; (c)Reaction and floor beams on right

2.3 Specimen #2

Following the successful test of Specimen #1, the objectives of the test on the second specimen shifted to an additional concern with respect to Caltrans practice in the design of CIP-PT girders. Current AASHTO provisions restrict the number of ducts that may be bundled through specification 5.9.5.1.1 which states that "ducts may be bundled together in groups not exceeding three…" Caltrans currently allows up to four bundled ducts in PT box girders. Consequently, it was decided that the second test would investigate the presence of four bundled ducts. Another issue being considered by Caltrans is the potential savings in bridge construction through the possible reduction in the web width. The standard web width for box girders is currently 12" and there is considerable interest in possibly reducing the width of the web to 10" (which is common in bulb-T sections in other parts of the US). Hence, the current study was extended to consider both issues simultaneously: a reduced web width that accommodated up to four ducts.

The details of the girder are displayed in Figure 2.15. The primary girder dimensions, as evident from the figure, comprised a total length of 28 feet and a depth of 4.5 feet. Section B-B is the critical region, spanning 6 feet, where the specimen is expected to fail in shear. The arrangement of the four ducts in the critical region is shown in Figure 2.16 (a) where the profile of the ducts is horizontal. The cross-section of the girder on either side of the critical region is shown in Figure 2.16 (b) – both the section size and reinforcement was increased to preclude shear or flexural failure in these regions. To accommodate the anchor plates at the ends of the girder, the bottom ducts would require a tapered profile. Based on the required PT force to achieve the Caltrans average stress (see Figure 2.8) due to post-tensioning, tendons were placed only in the top two PT ducts (diameters of 85 and 75 mm, respectively).

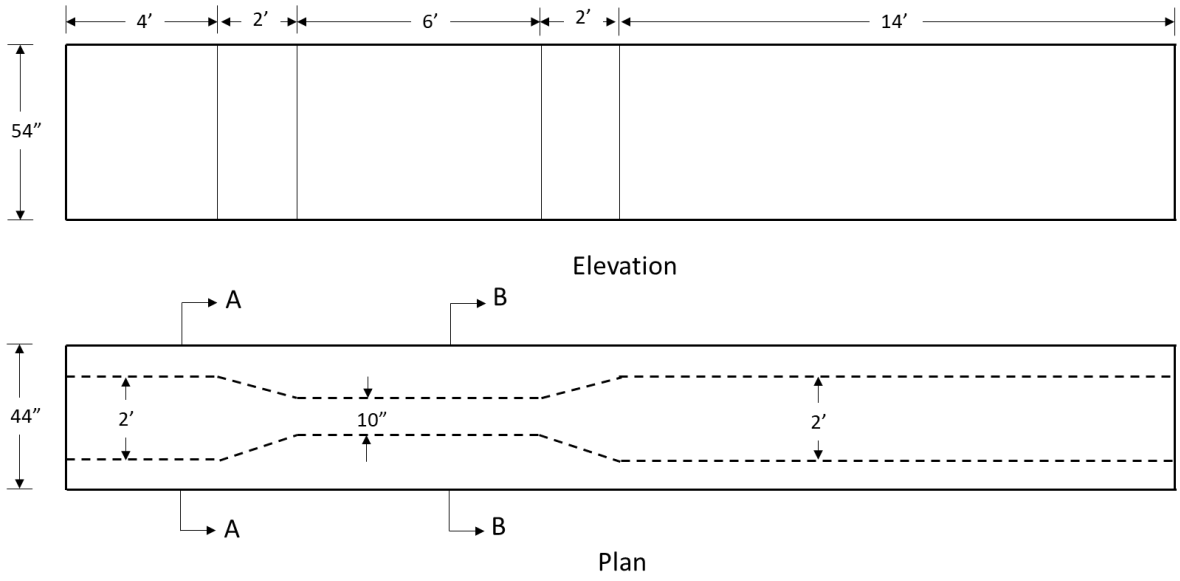

Figure 2.15: Basic configuration of specimen #2

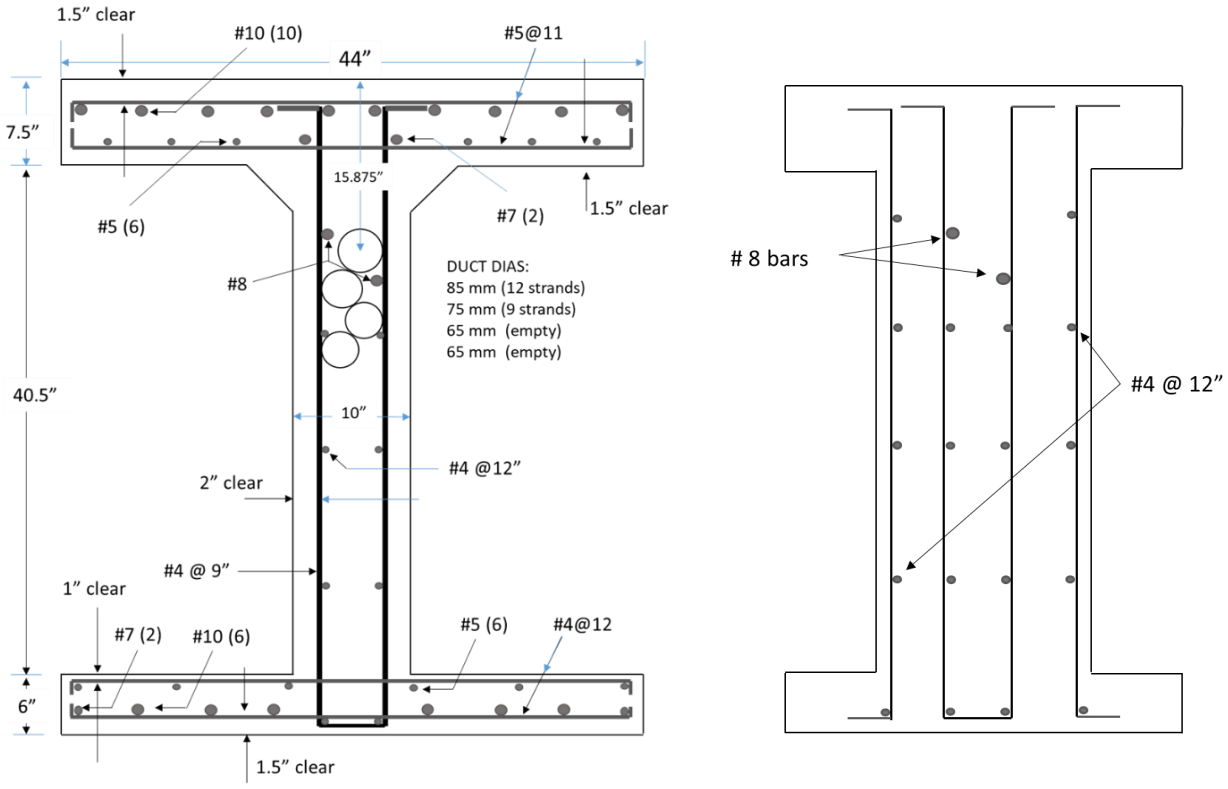

(a) Section B-B (b) Section A-A

Figure 2.16: Cross-sectional details of specimen #2

(Note: Section A-A is not to scale)

The lower two ducts (diameter 65 mm each) were grouted without any tendons. The resulting duct profiles, from an elevation perspective, are shown in Figure 2.17.

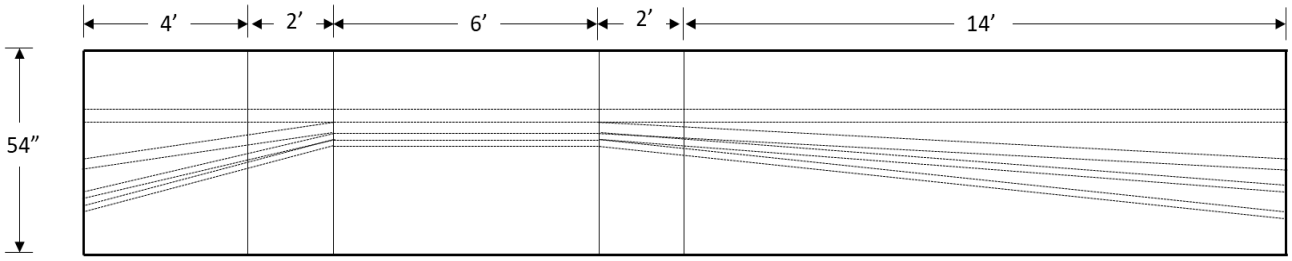

Figure 2.17: Projected duct profiles

2.3.1 Construction and Instrumentation

Figure 2.18 shows sequential stages of the formwork construction. The placement of the multiple ducts are visible in these figures. The top two ducts have diameters of 85 mm and 75 mm though the anchor plates for both ducts can accommodate up to 12 strands each. As previously noted in Figure 2.16 (a), the diameter of the bottom ducts are 65 mm each.

This specimen was instrumented with thirteen strain gauges – seven on the shear reinforcement in the critical region and six on longitudinal reinforcement. The strain gauge locations are identified in Figure 2.19. The gauges on the shear reinforcement were installed to monitor yielding of the stirrups – with two redundant gauges placed closest to the critical section. Two gauges (L1 and L2) were placed on the #8 bars on either side of the top duct and 4 gauges (L5 – L8) were installed on the top longitudinal bars (an additional gauge on each bar for redundancy).

Figure 2.18: Formwork construction for specimen #2

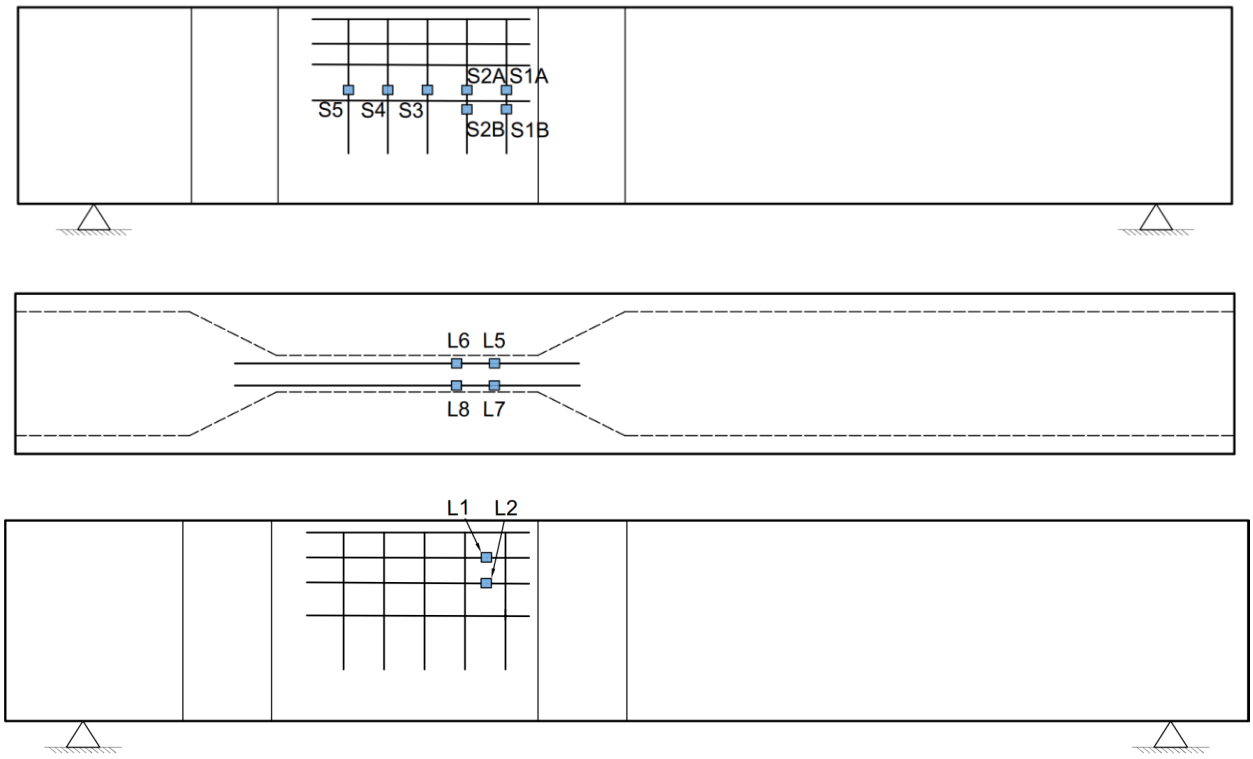

Figure 2.19: Instrumentation of specimen #2

The distribution of the axial strains across the longitudinal bars was adequate to provide data to estimate the strain at the centroid of the tension reinforcement. As in the case of specimen #1, displacement transducers (LVDTs) were installed at three locations as shown to monitor movement under the supports and at the centroidal location of the applied load.

Once again, two truckloads of concrete were required for the pour. One of the photos taken during the concrete pour is shown in Figure 2.20. A total of 15 cylinders (6" diameter) were cast from each batch of concrete. The results of the cylinder testing (average of 3 cylinders) are displayed in Table 2.3.

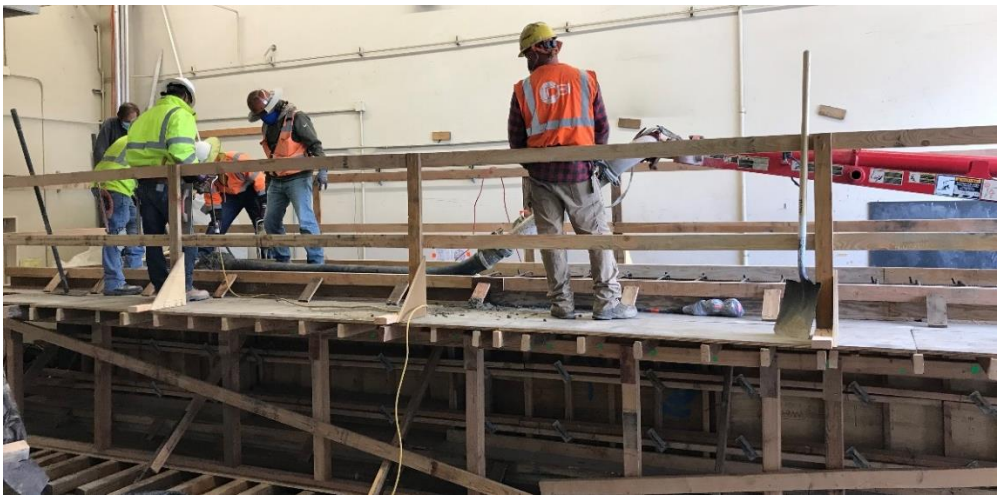

Figure 2.20: Concrete pour

Table 2.3: Evolution of compressive strength of concrete used in specimen #2

Age at test (days)	Batch 1	Batch 2	Average
	f_c' (psi)	f_c' (psi)	f_c' (psi)
3	3049	2602	2825
7	4001	3598	3799
21	4702	4668	4685
28	5376	5110	5243
Day of test	5780	5315	5547

Forms were stripped approximately a week after the pour (Figure 2.21). Based on the cylinder tests, the specimen was ready for post-tensioning after 7 days. However, post-tensioning of the specimen was carried out after the 28-day test. Since the concrete strength at post-tensioning was approximately 5200 psi, the projected jacking force to attain the average axial stress of 0.2 f_c was 1055 kips. It was not possible to achieve this force with 21 strands. Hence, 12 strands were placed in both the 85 mm and 75 mm ducts for a total of 24 strands (see Figure 2.22). Eventually, a total jacking force of 1050 kips was applied resulting in a tendon elongation

of 2.6 inches. The elongation at anchor set was 2.25 inches which resulted in an effective jacking force of about 910 kips and an axial stress of 0.17 f_c.

Figure 2.21: Specimen #2 after stripping formwork and ready for post-tensioning

Figure 2.22: Post-tensioning of specimen #2

Following post-tensioning of the specimen, once again a professional moving and handling company assisted in lifting the specimen onto concrete support blocks. Top reaction beams were placed on the specimen and floor distribution beams were installed and connected to the reaction beam through high-strength rods. The final view of the girder prior to testing is shown in Figure 2.23.

Figure 2.23: Specimen #2 mounted on end blocks with reaction system installed

2.4 Design of Reaction System

One of the major challenges in carrying out the testing of the girders was the design of a reaction system that safely transmitted the reaction from the applied loads to the strong floor. As indicated previously, the strong floor area is equipped with five steel railroad tracks spaced 4 feet center-to-center to provide a per-track tie-down capacity of approximately 50 kips/ft. After considering numerous configurations, the most convenient loading scheme to enable safe transfer of the reaction forces was determined to be one wherein the load was applied from the bottom and reaction beams were placed on top of the specimen as shown in Figure 2.24. This setup also adequately simulates the interior support region of a continuous bridge girder. The center-to-

center distance between the top reaction beams was 30 feet for Specimen #1 and 26 feet for Specimen #2.

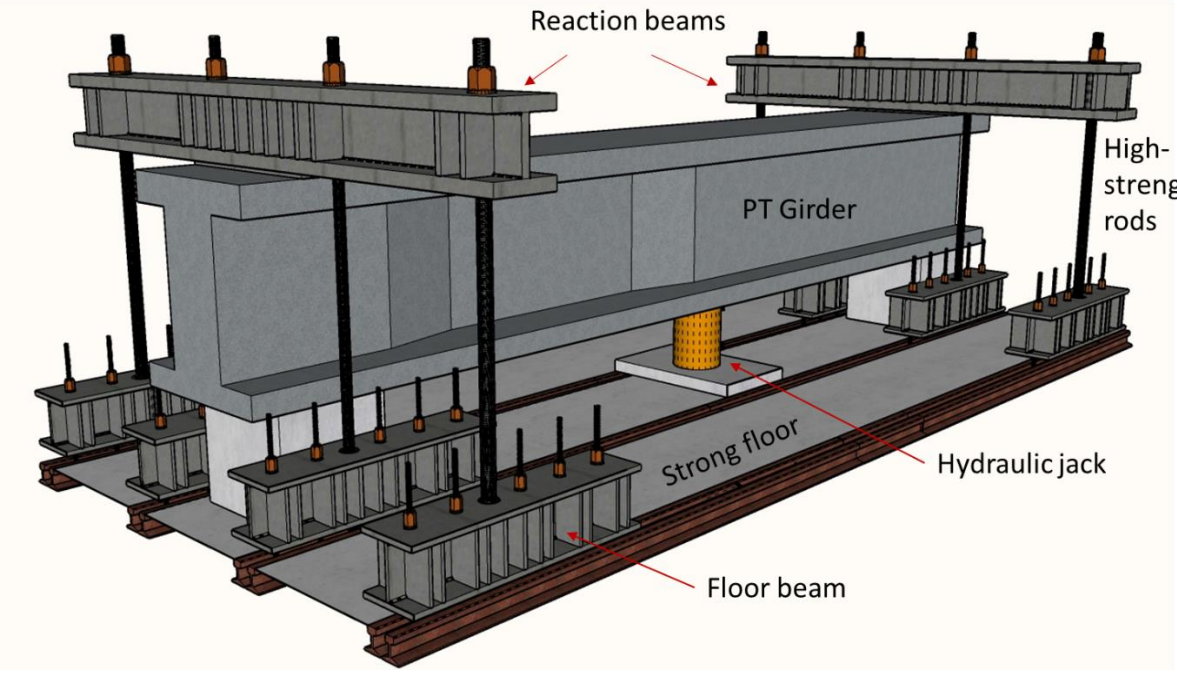

Figure 2.24: Schematic view of reaction system with specimen and loading jack

Both supports allow for the rotation of the reaction beams. The girder specimen itself can both translate and rotate at the support locations though the finite size of the support can introduce additional restraints. The idealization of the girder as a simply supported beam is approximate though not unreasonable to estimate the shear and moments along the span.

Loading is applied to specimen #1 by means of two hydraulic jacks acting simultaneously from a single pump, which can produce a maximum force of 2000 kips. A single hydraulic jack was adequate for specimen #2 due to the its reduced design shear capacity. The reacting forces on the girder from the applied load are resisted by the top reaction beams and then transferred through eight high-strength bars (four on each beam) to distribution beams that are anchored to the floor,

as shown in Figure 2.23. To avoid the concentration of forces on the inner floor beams, the diameters of the outer bars are larger making them stiffer and thereby shifting additional vertical forces to these outer floor beams. The inner high-strength bars have an effective diameter of 2.25" while the outer bars have a diameter of 2.95".

Complete details of the reaction and floor beams are provided in Figures 2.25 to 2.27. The top reaction beam was fabricated from a heavy W14 x 455 section. The beam was stiffened with five 1.5" thick stiffener plates in the central region that reacts directly above the girder specimen. Four holes as shown were drilled to accommodate the high-strength rods. Pipe sections (5XXS and 4XXS at the end section and interior section, respectively) were then welded to the web of the beam. The floor beams were fabricated using W14 x 176 sections also contain stiffener plates. The only difference between the inner and outer floor beams was the size of the welded pipes – based on the diameter of the high-strength bars that were anchored to these beams. The beam cross-sections for both the reaction beams and distribution floor beams were based on extensive finite element analyses of the reaction system described in the next section.

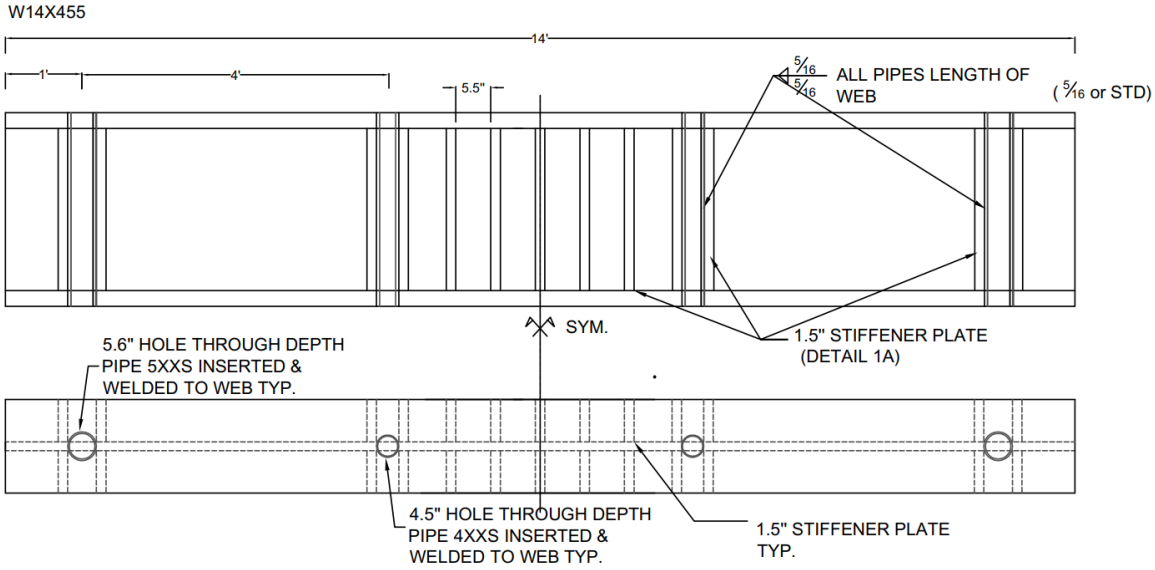

Figure 2.25: Details of reaction beams

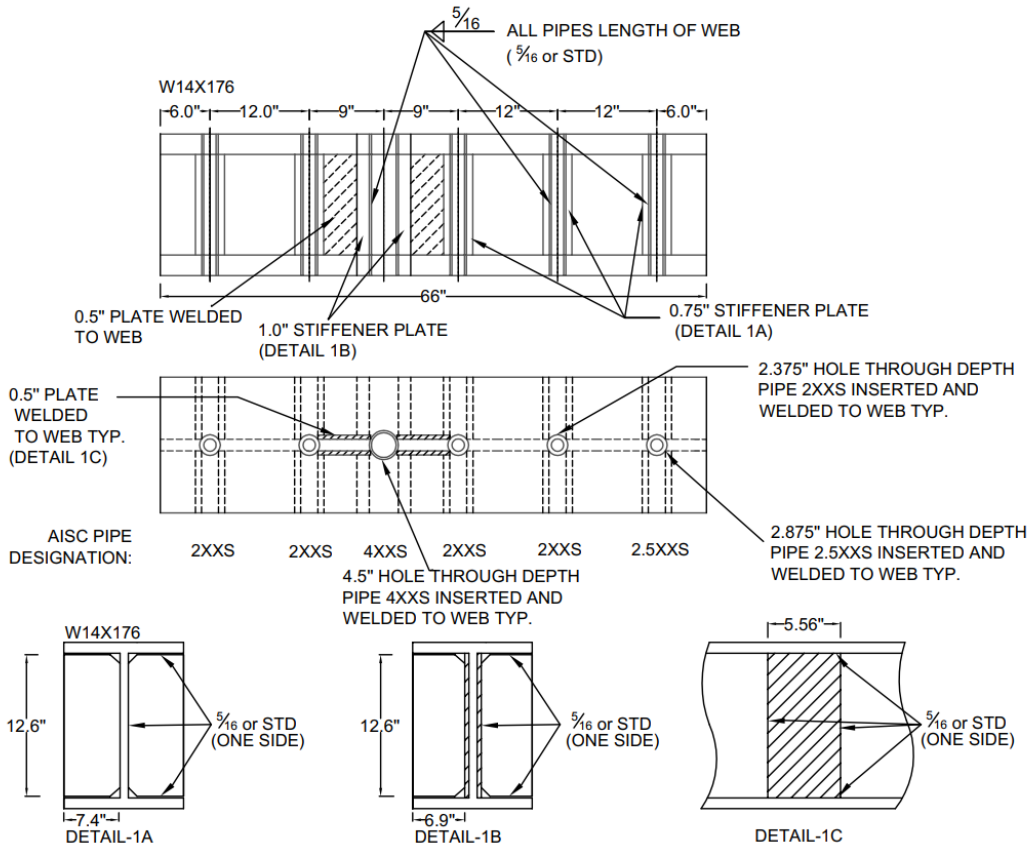

Figure 2.26: Details of inner floor beams

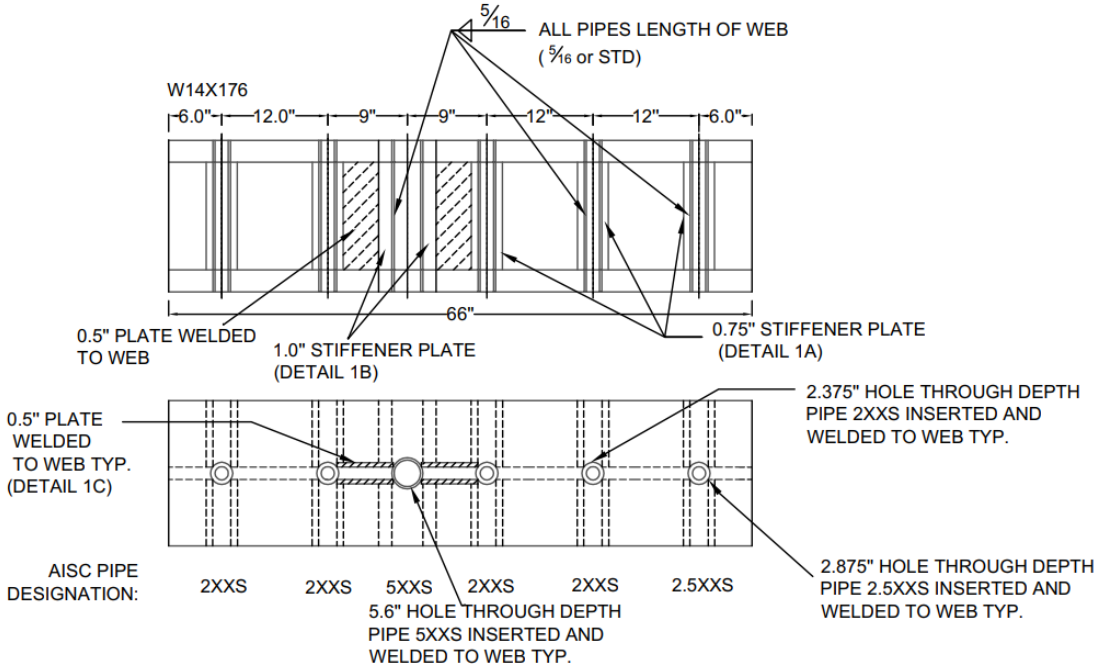

Figure 2.27: Details of outer floor beams

2.4.1 Analysis of the proposed reaction system

A finite element analysis of the reaction system was carried out using the commercial software ATENA (Cervanka et al.. 2020) to assess the integrity of the system so that the maximum applied loads are transferred safely to the strong floor without yielding the steel beams or damaging the strong floor. The material for all W-sections is ASTM A992 with a nominal yield strength of 50 ksi. Pipe sections are ASTM A53 Grade B with an expected yield strength of 60 ksi while plates used as stiffeners are ASTM A572 with a specified yield strength of 50 ksi.

Given the symmetry of the reaction system on either side, only one-half of the system on one side of the girder that resists the larger reaction was analyzed. Given the loading configuration, approximately 55% of the applied load would be resisted by one reaction beam. Assuming a maximum applied load of 1800 kips at failure (based on preliminary analysis of the girder capacity), the reaction on the side resisting the larger force was approximated to be 1000 kips. Therefore, an analysis of the half-segment of the reaction system was conducted by applying a uniformly distributed load as shown in Figure 2.28 corresponding to a total reaction force of 500 kips.

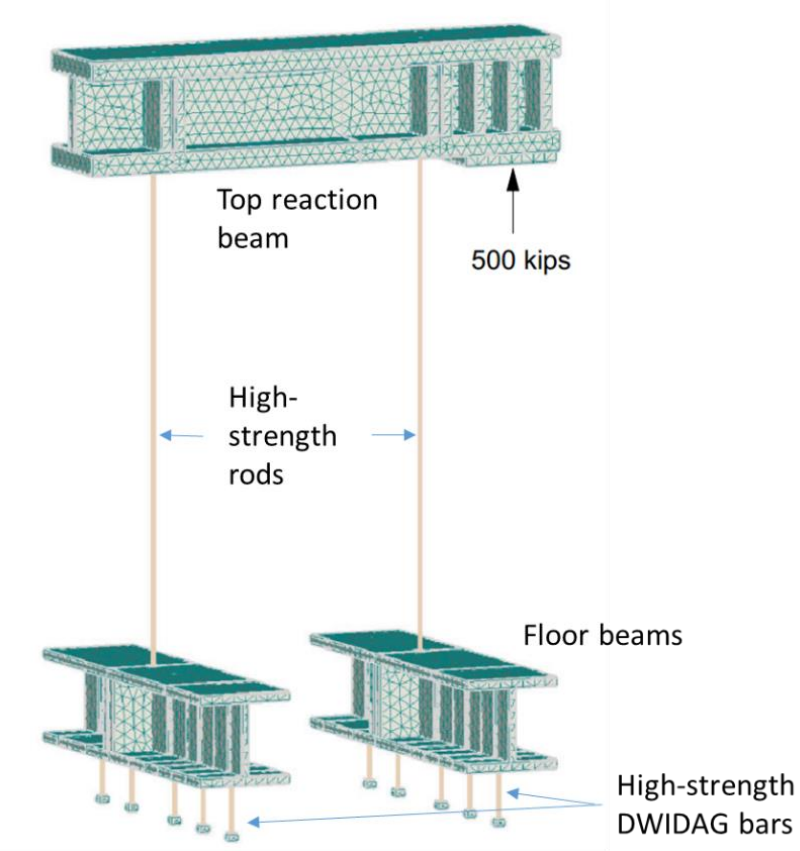

Figure 2.28: Finite element model of half the reaction system on one side of the specimen

Contours of the Von-Mises stress were examined under the imposed loading. For the top reaction beams without stiffener plates, results from the initial ATENA analysis indicated stress concentration near the intersection of the web and top flange where the pipe sections are inserted. Hence, several stiffener plates with a thickness of 1.5 inch were welded on both sides of the inserted pipes as well on the mid-section of the beam where the load is applied, in order to prevent local buckling and reducing stress concentration in the web-flange interface. Following the addition of the stiffener plates, the finite element analysis of the model shown in Fig. 2.28 produced a maximum Von-Mises stress of 36 ksi (shown in Figure 2.29), which is lower than the nominal yield strength of the ASTM A992 W-sections.

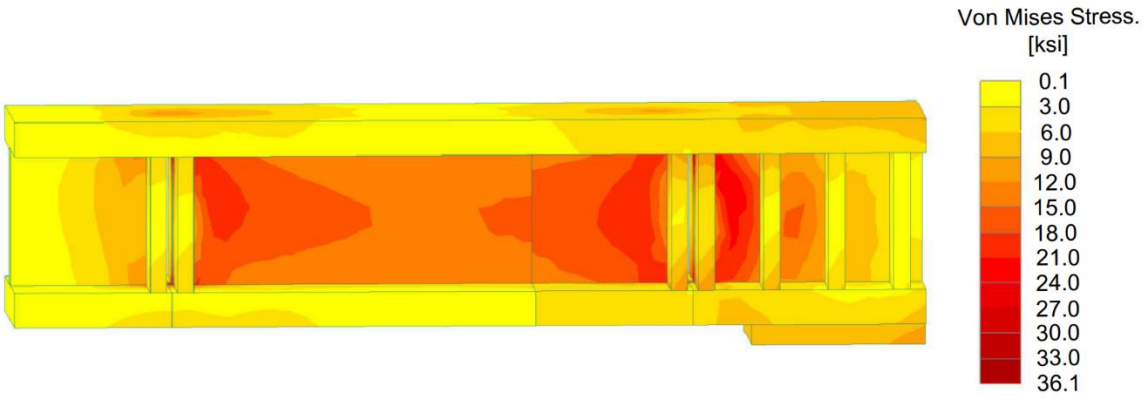

Figure 2.29: Von-Mises stresses on reaction beam

Likewise, for the bottom beams, similar stress concentrations were observed as in the case of the reaction beams in the absence of stiffener plates. The addition of 1.0-inch stiffener plates alleviated the stress concentration and the observed maximum Von Mises stress in the bottom floor beams was approximately 30 ksi, as shown in Figure 2.30. The peak deflection at mid-span of the top reaction beams was approximately 0.3 inches.

An issue of concern that needed additional verification was the rotation and stress concentration in the hexagonal nuts that connected the high-strength rods to the reaction beams. The high-strength rods were modeled as truss elements in the simulations presented above. At a peak displacement of 0.3”, the deflected shape of the reaction beams could induce rotations in the washers and nuts that could result in localized stresses. To address this concern, a separate three-dimensional model was developed representing the high-strength rod, the washers and nut under an imposed rotation corresponding to the peak mid-span displacement of the beam. Figure 2.31 displays the deformed shape of the high-strength rod and the corresponding principal stresses. As evident from the figure, the maximum stress is well below the yield strength of the components.

Hence the reaction system is determined to be adequate to resist the imposed loads without any adverse effects.

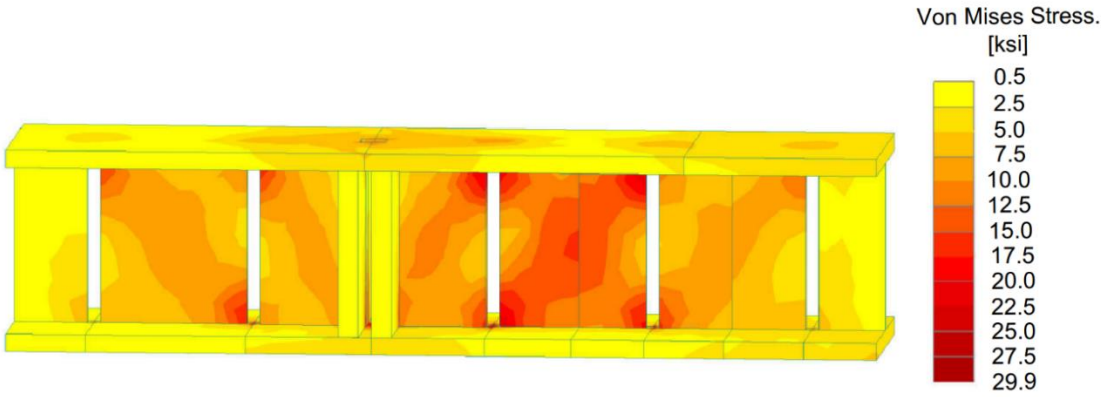

Figure 2.30: Von-Mises stresses on inner floor beam

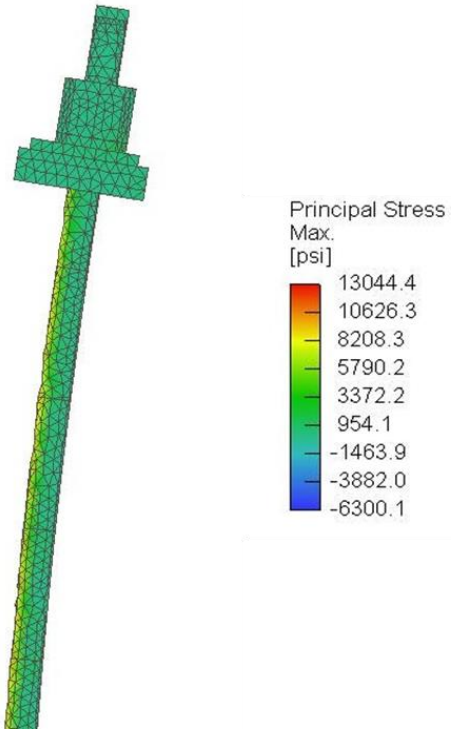

Figure 2.31: Contours of major principal stress on critical high-strength rod

3.0 RESULTS FROM EXPERIMENTAL TESTING OF GIRDER SPECIMENS

The two girder specimens described in the previous chapter were tested to failure in the structural testing facility at the University of California, Davis. Details of the testing and observed behavior under the imposed loading are outlined in the following sections.

3.1 Specimen #1

The first specimen, as described in the previous section, had an overall depth of 5 feet and consisted of a single primary straight duct with a diameter of 4.5 inches and containing 26 tendons. The smaller secondary duct also had a straight profile in the critical region but contained a single PT strand. The specimen, supported on concrete blocks, with the hydraulic jack placed below the loading point is shown in Figure 3.1. Also visible are the reaction beams on top of the girder that transmit the reaction forces through high-strength rods to distribution beams located on the strong floor (shown in Fig. 2.13 in the previous chapter).

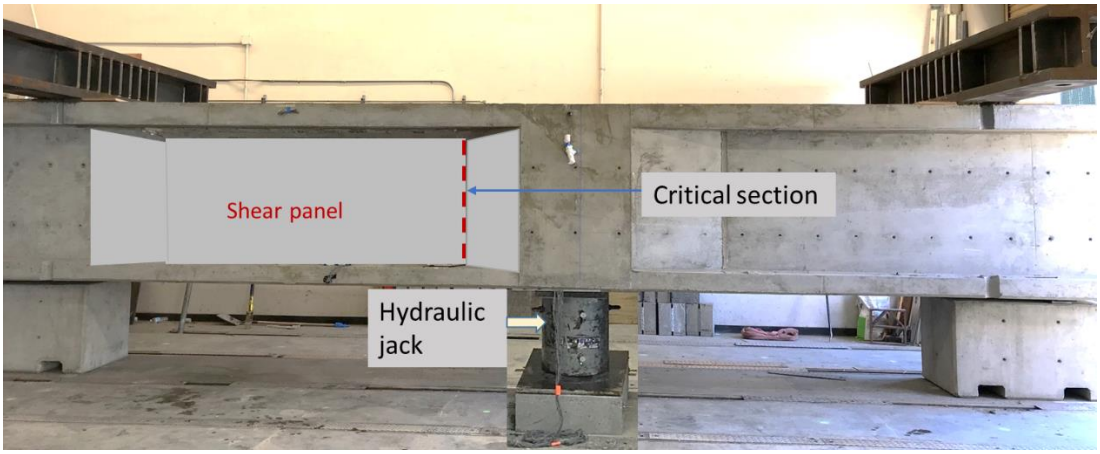

Figure 3.1: Girder specimen #1 ready for testing

3.1.1 Experimental Observations

A monotonically increasing load was applied on the specimen through the hydraulic jacks (shown in Figure 3.1) resulting in tension on the top surface of the girder. The loading was increased in increments of 100 kips up to a load of 400 kips. Following an applied load of 400 kips that resulted in a shear of approximately 180 kips at the critical section, loading was stopped at controlled intervals based on the shear at the critical section. Observed cracking with increased loading is displayed in Figure 3.2. Hairline shear cracks were first observed when the shear in the critical section was approximately 250 kips as shown in Fig. 3.2 (b).

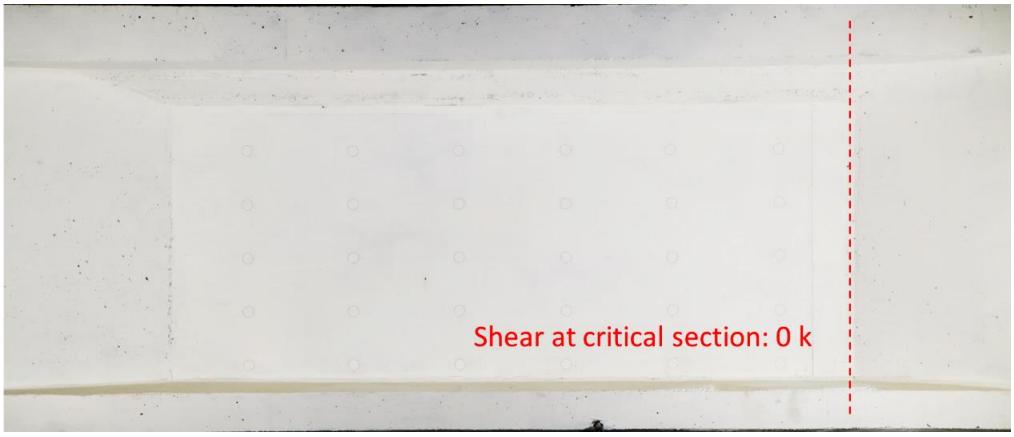

(a)

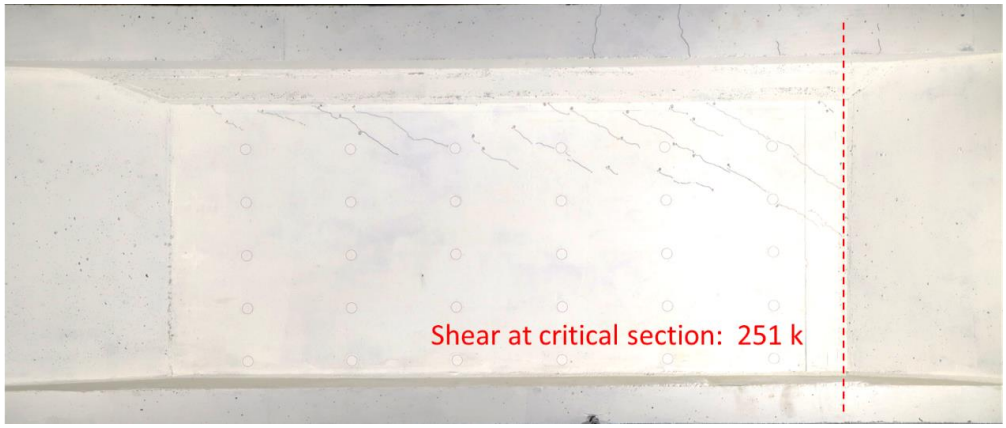

(b)

Figure 3.2: Evolution of damage in the shear-critical region of specimen #1

Minor flexural cracking also occurred when the applied load was approximately 556 kips (and the shear in the critical section reaches 251 kips as shown in Fig. 3.2 b). The maximum crack width was under 1 mm (0.04”). Shear cracking becomes widespread at an applied load of 1100 kips and the shear at the critical section just exceeded 500 kips (Fig. 3.2 c). Note that the predicted shear capacity using AASHTO guidelines is approximately 482 kips at an applied load of about 1000 kips, as will be discussed later in this chapter. Upon further loading, both flexural and shear cracking extended further across the beam as seen in Fig. 3.2 (d) and the maximum crack width just exceeded 1 mm (~ 0.05”).

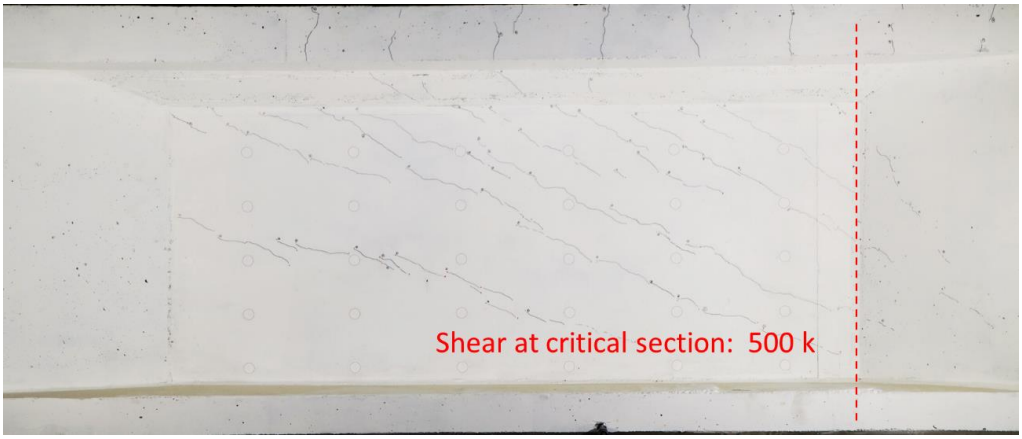

(c)

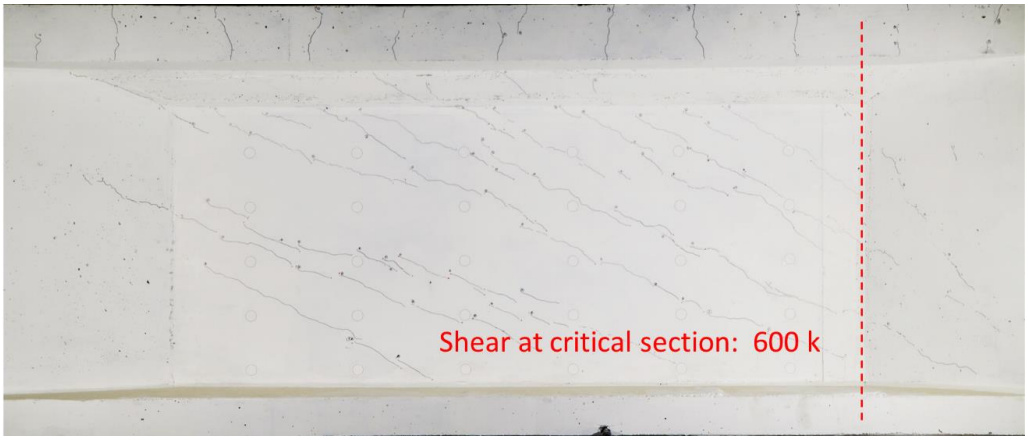

(d)

Figure 3.2 (continued): Evolution of damage in the shear-critical region of specimen #1

(e)

Figure 3.2 (continued): Evolution of damage in the shear-critical region of specimen #1

Loading continued up to a maximum value of 1500 kips and the corresponding shear at the critical section in panel region (also referred to as the shear-critical region) was 677 k. Though extensive shear cracking was observed as displayed in Fig. 3.2 e (and the maximum crack width was approximately 0.1”), the specimen was still resisting vertical loading and there was no indication of impending shear failure. The loading was stopped at this point since the shear resisted by the specimen was significantly larger than the predicted capacity using AASHTO. Moreover, there was some concern about the maximum capacity of the strong floor to resist additional loading.

Following the completion of testing, the girder was separated into two parts by cutting through the critical section. A view of the girder cross-section is displayed in Figure 3.3 where approximately half the tendons are visible while the others are obscured by the grout material. No visible distress around the duct region was observed indicating that the corrugated metal duct bonds well to the concrete and remains intact even at loads approaching shear failure of the post-tensioned girder.

Figure 3.3: View of girder cross-section showing state of duct after testing

The force versus deformation response for the specimen is shown in Figure 3.4. The displacement shown is the measured deflection at the loading point whereas the force corresponds to the shear at the critical section X-X identified in the figure. Since the applied force is significantly greater than the dead load of the specimen, the shear force is almost constant across the panel. Note that the loading was applied in two phases: in phase 1, the total applied load was approximately 1300 kips which resulted in a shear of 585 kips in the critical panel region. The actuators were retracted at this stage at a residual displacement of 0.2 inch indicating that the shear yielding in the panel region had commenced. The shear resisted by the section was already larger than the expected capacity using the AASHTO procedure for estimating the shear capacity of a PT girder. In the next phase, the specimen was loaded up to 1500 kips that induced a shear of approximately 680 kips in the critical region. Though a complete shear failure did not occur, testing was stopped since there was concern that the imposed load was close to the capacity of the strong floor.

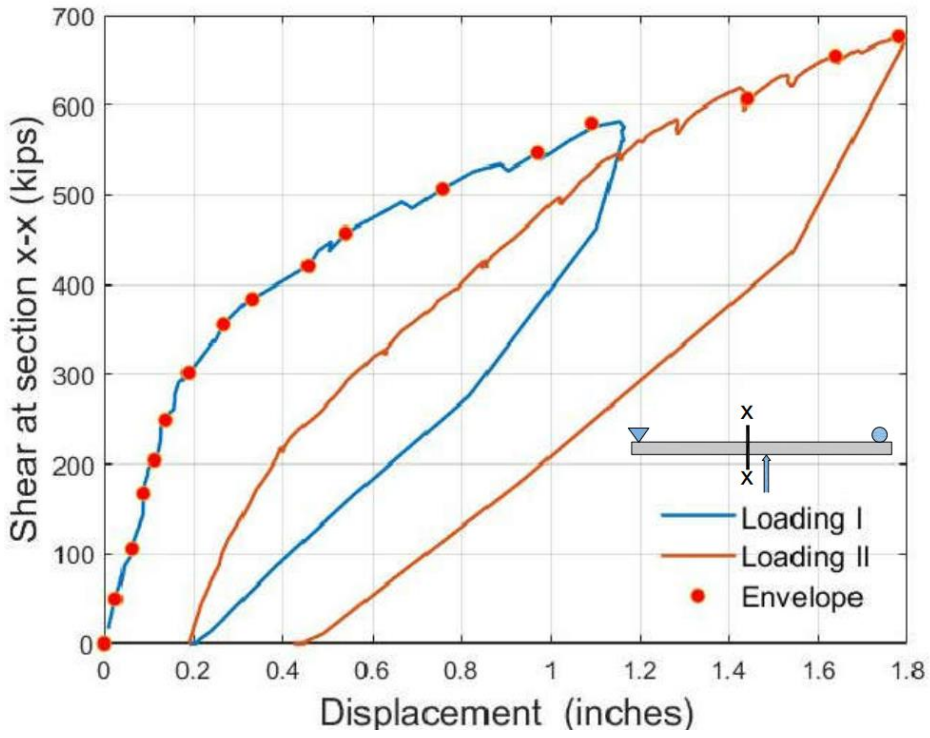

Figure 3.3: Shear-displacement response of specimen #1

The progression of measured strains in the stirrups as a function of the applied loading are shown in Figure 3.4. Also shown are the locations of the strain gauges. Two of the gauges, S3 and S4, were likely damaged during the concrete pour and did not record reasonable strain values. It is evident from the measured strains that all the stirrups experienced forces that resulted in their yielding.

Next, the strains monitored in the longitudinal bars are examined. One of the key parameters in establishing the AASHTO shear capacity of a girder cross-section is the strain at the centroid of the tension reinforcement, ε_s. Since there were no longitudinal bars at this precise location, it was necessary to interpolate the measured strains across the depth of the section to establish this strain measure. Four strain gauges were installed at different locations as displayed in Figure 3.5 (a). Two gauges were placed on two #10 bars located in the top flange (see also

Figure 2.6 which shows the cross-section of the girder with reinforcing details). The remaining two gauges were placed on the #8 bars above and below the duct (as displayed in Figure 2.6) separated by a distance of approximately 4 inches. The progression of strains across the depth of the section is shown in Figure 3.5 (b) wherein the linear distribution is approximated from the discrete strain measures at three points along the depth.

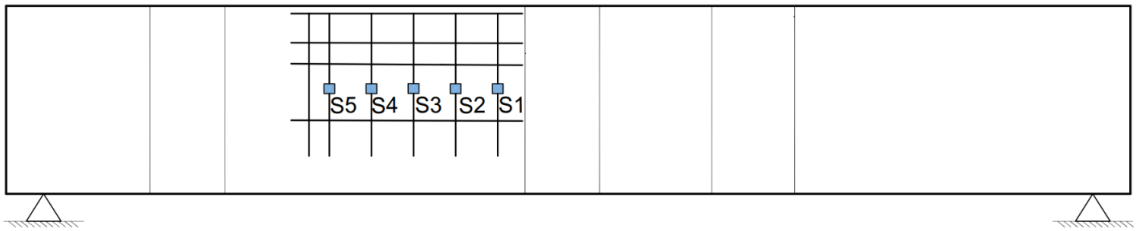

(a) Strain gauge locations

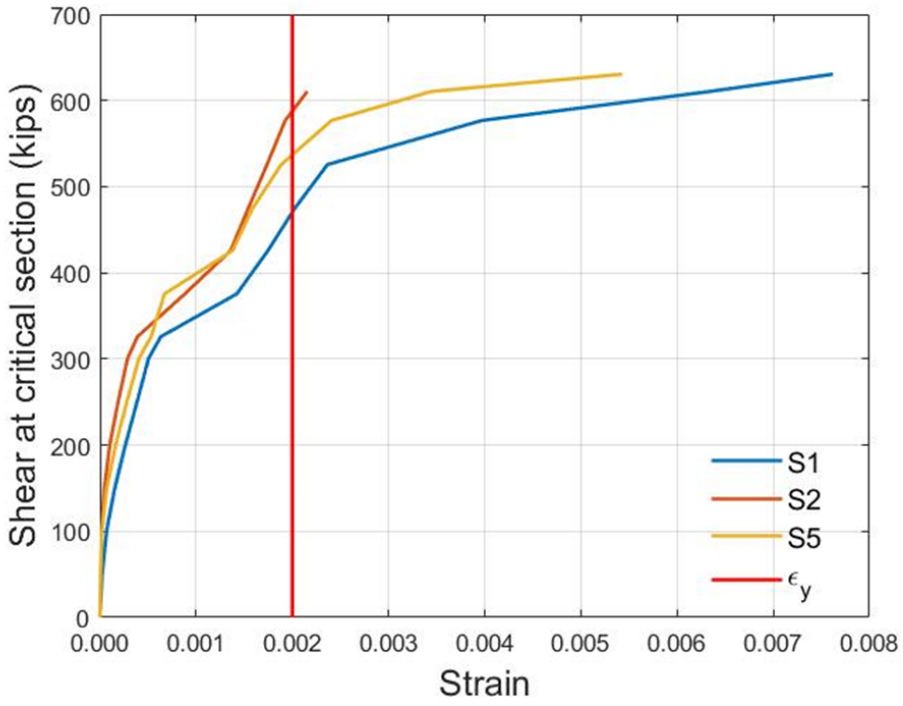

(b) Recorded strains

Figure 3.4: Evolution of strains in the shear reinforcement of specimen #1

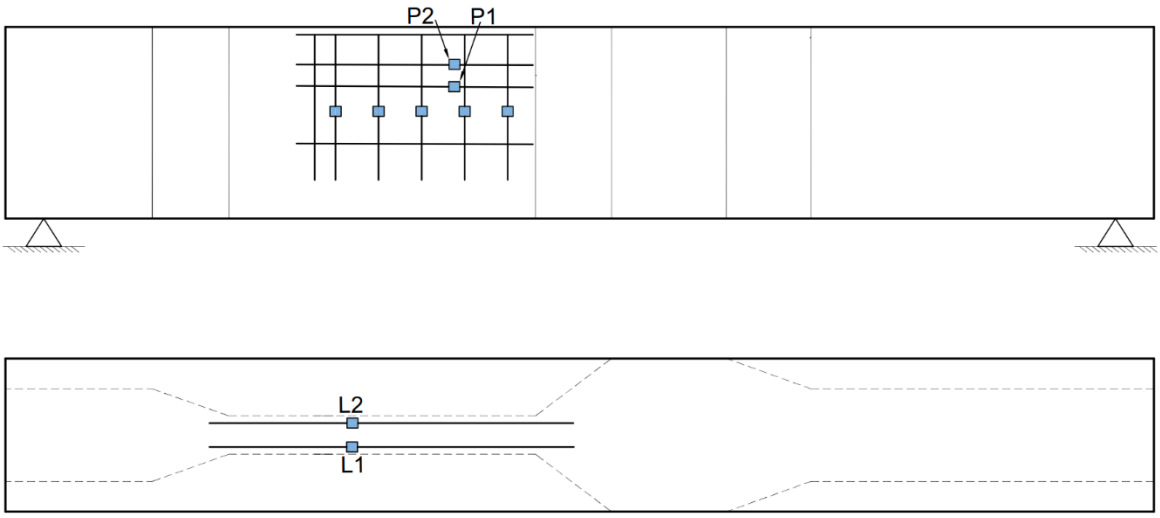

(a) Strain gauge locations

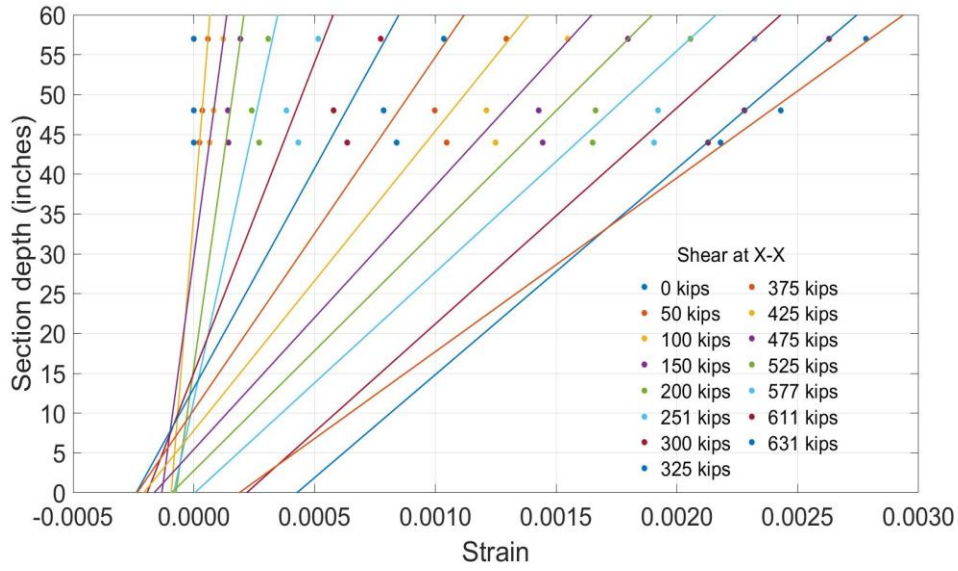

(b) Recorded strains and approximated distributions

Figure 3.5: Evolution of strains in the longitudinal reinforcement across section depth

It is important to note that the peak recorded strain in the longitudinal bar is approximately 0.00275 whereas the expected yield strain corresponding to a yield stress of 68 ksi was 0.0023 indicating that flexural yielding had likely commenced thereby inhibiting a complete shear failure of the specimen.

3.2 Specimen #2

The second specimen had an overall depth of 4.5 feet and consisted of four ducts: the top two ducts had diameters of 85 mm (3.5 inch) and 75 mm (3.0 inch) whereas the bottom ducts were 65 mm (~2.5 inch) each as shown in Figure 2.15. The specimen, supported on concrete blocks, is shown in Figure 3.6. Also seen in the figure is the hydraulic jack placed below the loading point and the reaction beams on top of the girder that transmit the reaction forces through high-strength rods to distribution beams located on the strong floor.

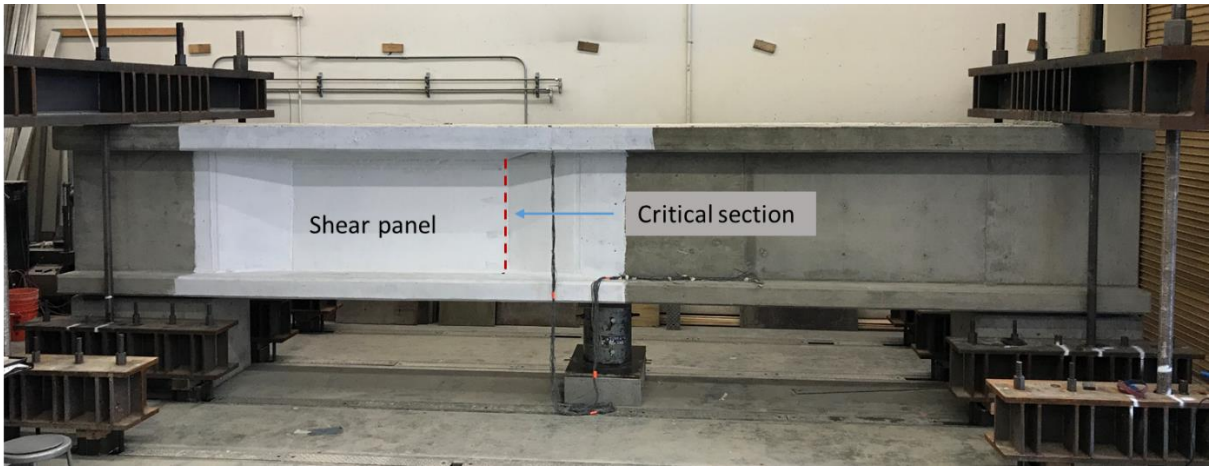

Figure 3.6: Girder specimen #2 ready for testing

3.2.1 Experimental Observations

As in the case of Specimen #1, a monotonically increasing load was applied on the specimen through the hydraulic jacks placed at the bottom of the girder resulting in tension on the top surface of the girder. The loading was increased in increments of approximately 100 kips up to a load of 400 kips. Following an applied load of 400 kips that resulted in a shear of approximately 180 kips at the critical section, hairline shear cracks were first observed at the upper right corner

as shown in Figure 3.7 (a). No additional cracking was observed till the applied load exceeded 600 kips. New cracks appeared during the loading phase 700 – 800 kips (corresponding to a shear in the critical section of 315 – 360 kips) and the extent of cracking at an applied load of 800 kips is shown in Figure 3.7 (c). Upon continued loading, additional cracking was seen in the panel region and both the crack width and crack length of existing cracks increased. The maximum crack width at this stage was approximately 1.5 mm (~ 0.05”). The state of damage at an applied load of 1000 kips (and a shear of 450 kips at the critical section) is displayed in Figure 3.7 (d). A dramatic shear failure occurred when the loading reached 1030 kips as shown in Figure 3.7 (e).

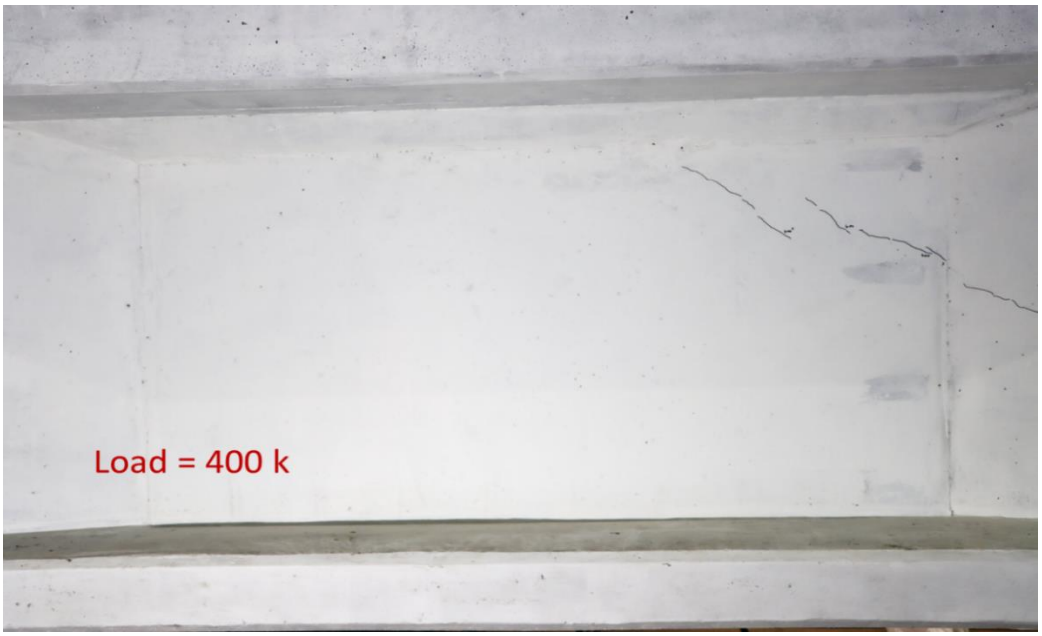

(a)

Figure 3.7: Evolution of damage in the shear-critical region of specimen #2

(b)

(c)

(d)

Figure 3.7 (continued): Evolution of damage in the shear-critical region of specimen #2

(e)

Figure 3.7 (continued): Evolution of damage in the shear-critical region of specimen #2

The resulting force-displacement curve is shown in Figure 3.8. At the failure load of 1030 kips, the shear at the critical section X-X was approximately 466 kips. The applied load was paused at the points highlighted by the red dots (labeled as the envelope points on the curve) while the panel region was examined for cracking. The hydraulic jacks show minor pressure drops when the load is sustained. The unloading curve when the pressure in the jacks were released is also shown in the figure.

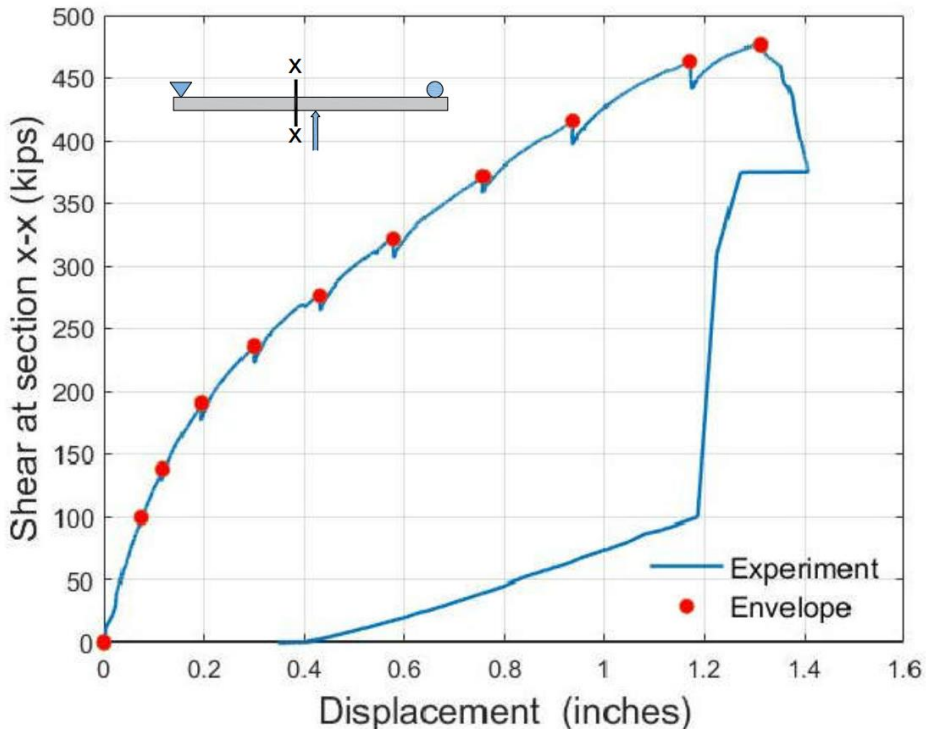

Figure 3.8: Shear force versus displacement response for specimen #2

The locations of the strain gauges placed in the stirrups of specimen #2 are displayed in Figure 3.9 (a) and the recorded strains in the stirrups as a function of the applied loading are shown in Figure 3.9 (b). It is evident from the measured strains that yielding occurred in all the stirrups. The strains in gauges S1A and S2A were below the yield strain suggesting localization of strains across a crack that were outside the location of the gauges.

Figure 3.10 shows the evolution of strains in some of the longitudinal bars across the section depth. Just as in the case of specimen #1, the measurement of longitudinal strains provides a means to determining the strain at the centroid of the tension reinforcement, ε_s. The average strain from four measurements of the top longitudinal bars was used to represent the longitudinal strain at a depth of approximately 3 inches from the extreme tension face. Once

again, the linear distribution is approximated from the discrete strain measures at three points along the depth. Based on the maximum recorded strain in the top longitudinal bars, it is concluded that flexural yielding was precluded and the specimen failed in shear.

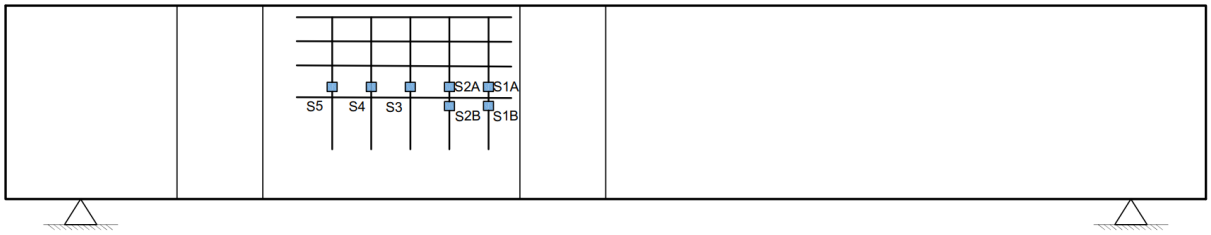

(a) Strain gauge locations

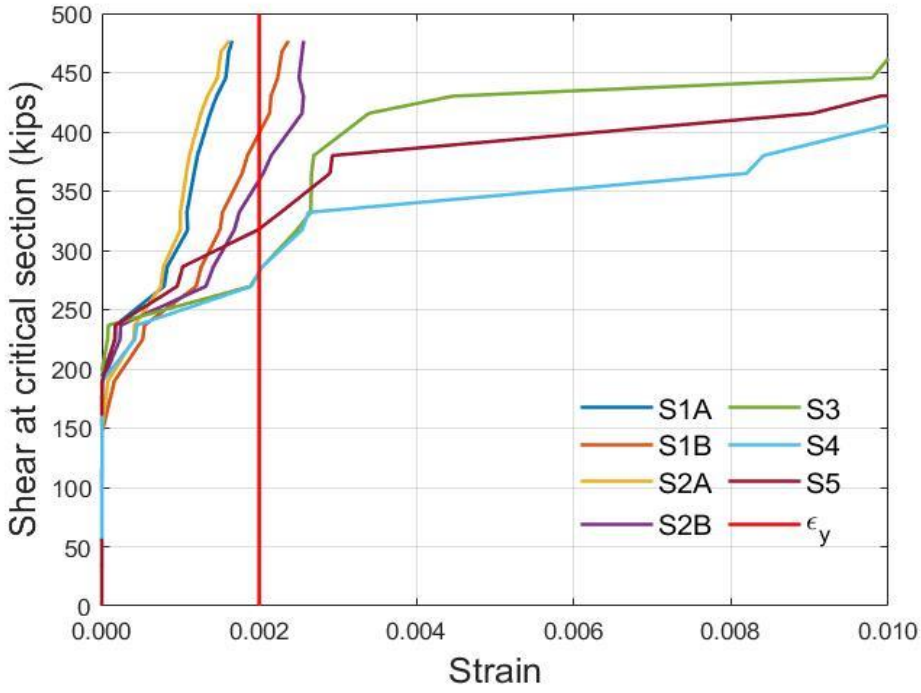

(b) Shear-strain response

Figure 3.9: Evolution of strains in the shear reinforcement of specimen #2

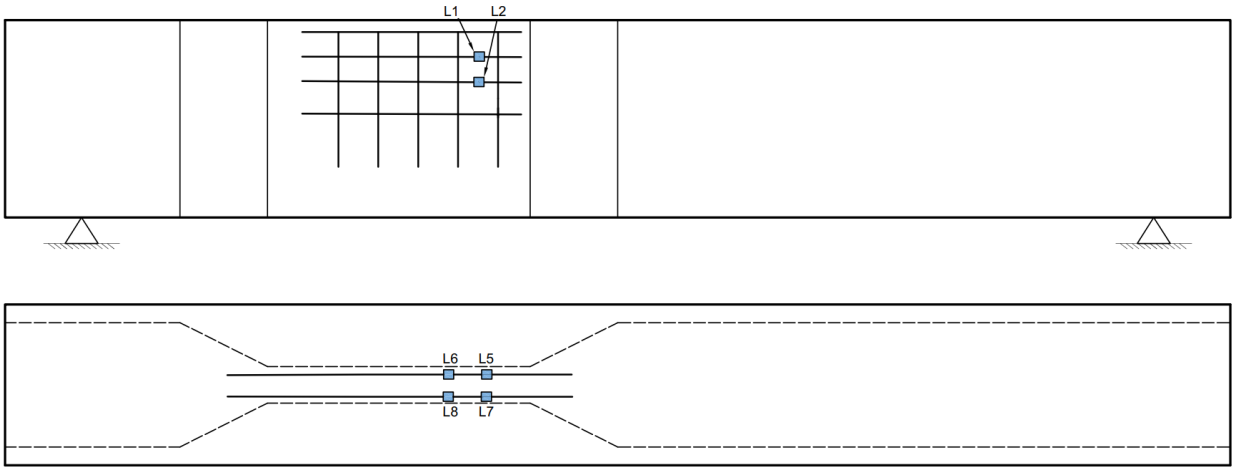

(a) Strain gauge locations

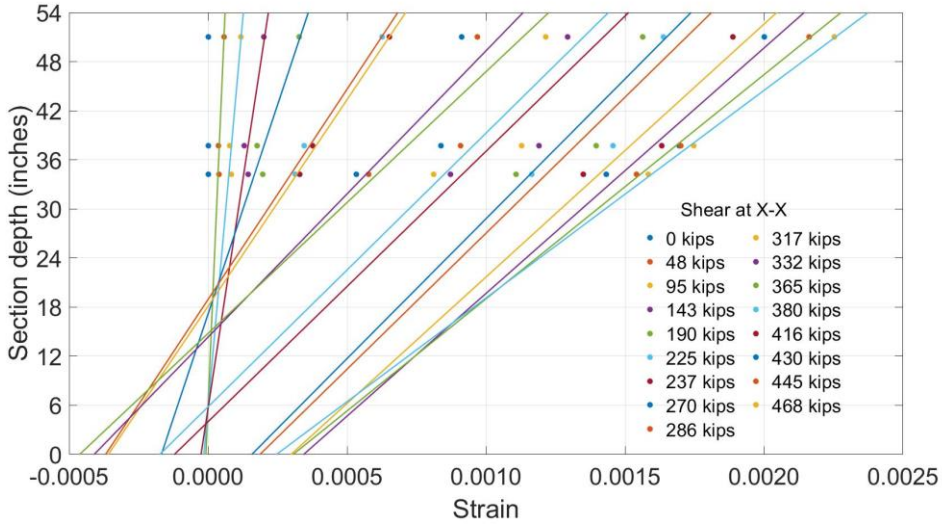

(b) Recorded strains and approximated distributions

Figure 3.10: Evolution of strains in the longitudinal reinforcement across section depth

3.3 Observed versus Predicted Shear Capacity of Specimens

As stated at the outset of this report, a primary goal of the project is to compare the shear capacity of a PT girder based on experimental testing to the expected shear capacity using the Caltrans procedure which comprises a slight modification to the AASHTO recommendation. The general AASHTO procedure for estimating the shear capacity of a PT girder is first summarized in this section followed by a description of the Caltrans amendment to the AASHTO methodology.

3.3.1 Shear Resistance of Post-Tensioned Girders

In general, Caltrans adopts the provisions in AASHTO for the design of PT box girders with several amendments based on California practice. Hence, the AASHTO methodology for estimating the shear strength of a girder is outlined in this section. First, the average stress in prestressing steel, f_{ps}, is estimated using:

$$f_{ps} = f_{pu}(1 - k\frac{c}{d_p}) \tag{3.1}$$

in which

$$k = 2(1.04 - \frac{f_{py}}{f_{pu}}) \tag{3.2}$$

In determining the flexural capacity of the section, it is necessary to check for T-action. The distance to the neutral axis *c* for rectangular section behavior is:

$$c = \frac{A_{ps}f_{pu} + A_s f_s - A'_s f'_s}{\alpha f'_c \beta_1 b_w + k A_{ps}\frac{f_{pu}}{d_p}} \tag{3.3}$$

For T-section behavior:

$$c = \frac{A_{ps}f_{pu}+A_s f_s - A'_s f'_s - 0.85 f'_c (b-b_w)h_f}{\alpha f'_c \beta_1 b_w + k A_{ps}\frac{f_{pu}}{d_p}} \quad (3.4)$$

The distance from the compression face to the centroid of the tension reinforcement d_e and the distance between the center of the compressive and tensile force blocks d_v are evaluated using:

$$d_e = \frac{A_{ps}f_{ps}d_p + A_s f_y d_s}{A_{ps}f_{ps} + A_s f_y} \quad (3.5)$$

$$d_v = \frac{M_n}{A_{ps}f_{ps} + A_s f_y} \quad (3.6)$$

The nominal flexural resistance is computed using:

$$M_n = A_{ps}f_{ps}(d_p - \frac{a}{2}) + A_s f_s (d_s - \frac{a}{2}) - A'_s f'_s (d'_s - \frac{a}{2}) + 0.85 f'_c (b - b_w) h_f (\frac{a}{2} - \frac{h_f}{2}) \quad (3.7)$$

where:

A_{ps} : area of prestressing tendons

f_{ps} : distance form extreme compression fiber to the centroid of prestressing tendons

A_s : area of non-prestressed tension reinforcement bars

f_s : stress in the mild steel tension reinforcement bars at nominal flexural resistance

d_s : distance from extreme compression fiber to the centroid of non-prestressed tensile reinforcement bars

A'_s : area of compression reinforcement bars

f'_s : stress in the mild steel compression reinforcement at nominal flexural resistance

d'_s : distance from extreme compression fiber to the centroid of compression reinforcement

f'_c : specified compressive strength of concrete at 28 days

b : width of the flange of the member

b_w : gross web width

h_f: compression flange depth

$a = c\beta_1$ equivalent depth of compressive stress block

The nominal shear resistance, V_n, is determined as the lesser of the following equations

$$V_n = V_c + V_s + V_p \tag{3.8}$$

The shear capacity, however, is limited by the following expression:

$$V_n \leq 0.25 f_c' b_v d_v \tag{3.9}$$

The effective width of the web, according to AASHTO, is:

$$b_v = b_w - k * \phi_{duct} \tag{3.10}$$

where:

k : web width reduction factor, 0.25 for grouted duct, 0.5 for ungrouted duct

ϕ_{duct}: duct diameter in the girder web

The net longitudinal tensile strain ε_s in the section at the centroid of the tension reinforcement:

$$\varepsilon_s = \frac{\frac{|M_u|}{d_v} + V_u - A_{ps} f_{po}}{(E_s A_s + E_p A_{ps})} \tag{3.11}$$

The above equation assumes that there is no applied load on the girder nor is there a vertical force component from the prestressing (as in the case of a horizontal duct). The above expression is valid for both specimens tested in this project since the ducts were horizontal across the critical section. The notation used in the above expressions are summarized below:

M_u: Factored moment in member

V_u: Factored shear in member

E_s: Young's modulus of reinforcement bars

E_{ps}: Young's modulus of prestressing tendons

The shear contribution from the concrete is determined from:

$$V_c = \beta\sqrt{f_c'}b_v d_v \tag{3.12}$$

where:

β: parameter related to resistance of slip across crack

$$\beta = \frac{4.8}{1+750\varepsilon_s} \tag{3.13}$$

The contribution of the shear reinforcement to the shear capacity is:

$$V_s = \frac{A_v f_v d_v cot\theta}{s} \tag{3.14}$$

where:

A_v: Reinforcement bars area within certain distance

θ: Angle of inclination of diagonal compressive stress $= 29 + 3500\varepsilon_s$

s: Transverse reinforcement bars longitudinal distance

The Caltrans procedure for estimating the shear capacity of a PT girder is identical to the AASHTO procedure outlined above with one exception. The effective width of the web for fully grouted ducts, per Caltrans amendment C 5.7.2.1, is:

$$b_v = b_w \tag{3.15}$$

The consequence of the above amendment is to slightly increase the concrete contribution V_c to the shear resistance of the girder.

3.3.2 Observed versus Predicted Shear Capacity of Tested Girders

The AASHTO procedure described in the previous section to determine the shear capacity is applied to the two girder specimens at the critical section of the girder. The revised

capacity applying the Caltrans amendment (Equation 3.15) is also computed and compared with experimental observations. Basic sectional data and key parameters for estimating the shear capacity are listed in Table 3.1 for both specimens.

Table 3.1: Data and computed parameters for both specimens

	Specimen #1	**Specimen #2**
A_s' (in.^{2})	12.2	10.68
A_s (in.^{2})	13.86	15.76
A_{ps} (in.^{2})	5.86	4.54
A_v (in.^{2})	0.62	0.4
k	0.28	0.28
f_{py} (ksi)	243	243
f_{pu} (ksi)	270	270
f_c' (ksi)	5.8	5.5
f_s' (ksi)	68	68
f_s (ksi)	68	68
b (in)	48	44
b_w (in)	12	10
b_v (in)	10.92	6.69
h_f (in)	6	6
d_p (in)	48	36.92
c (in)	8.7	8.7
a (in)	7.61	7.61
f_{ps} (kips)	256	248
M_n (k-ft.)	9,716	7,415

Two key parameters used in the estimation of the shear contribution of concrete are θ and β, which depend on the strain at the centroid of the tension reinforcement, ε_s. The centroidal strain was estimated during the experiments through linear interpolation of the measured strains across the depth of the section (see Figure 3.5 for specimen #1). The change in the strain as a function of the shear at the critical section is displayed in Figure 3.11. It is seen that the AASHTO-based estimate of the strain is reasonably close to the measured value as the applied load approaches the shear capacity of the section. The inclination of the diagonal cracking during testing varied between 25° and 31° as shown in Figure 3.12. The AASHTO estimate for the angle θ is significantly higher, as reported in Table 3.2.

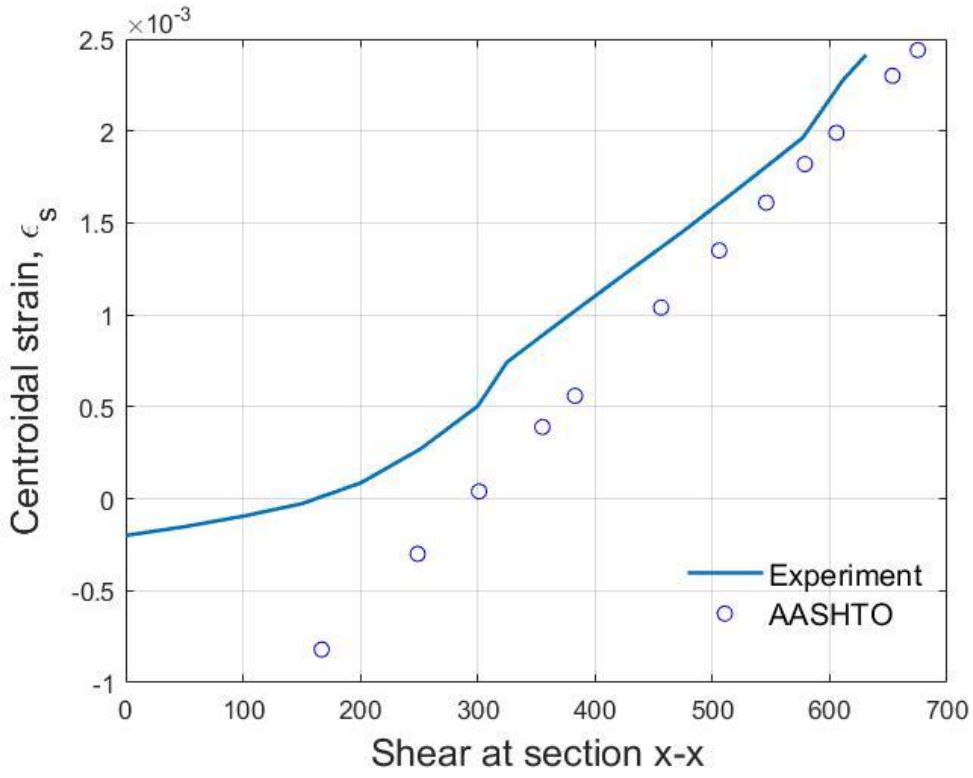

Figure 3.11: Measured centroidal strains versus AASHTO estimates (specimen #1)

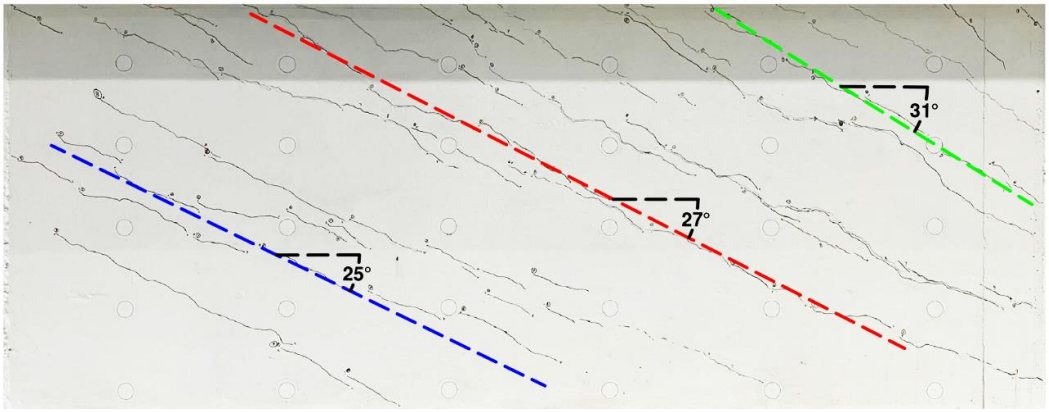

Figure 3.12: Observed inclination of diagonal cracks (specimen #1)

Table 3.2: Shear capacity estimate of specimen #1 with increasing load

Shear @ X-X (kips)	ε_s	θ	β	V_c	V_s	V_n
180	-0.0007	26.6	9.9	390.9	500.3	752.6
270	0.00006	28.8	5.01	198.0	455.6	653.6
360	0.00057	31.0	3.36	132.6	416.7	549.3
450	0.0012	33.2	2.52	99.7	382.6	482.2
540	0.00183	35.4	2.02	79.8	352.2	432.1
585	0.00215	36.5	1.84	72.6	338.3	410.9
630	0.00246	37.6	1.69	66.6	325.0	391.6
677	0.00278	38.7	1.56	61.5	312.3	373.8
720	0.00309	39.8	1.45	57.1	300.3	357.4

A summary of the key variables used in the computation of the shear capacity V_n of the critical section is presented in Table 3.2. The Caltrans estimate (as evident from Figure 3.13) is marginally higher because the concrete contribution to the shear capacity is based on the full width of the web without the reduction required by AASHTO (Equation 3-10). The shear resisted by the critical section with increasing load is plotted in Figure 3.13 along with the shear capacity estimates based on AASHTO and Caltrans specifications. The data indicates that there is a margin of safety of approximately 1.5 between the design equations used by Caltrans and measured capacity.

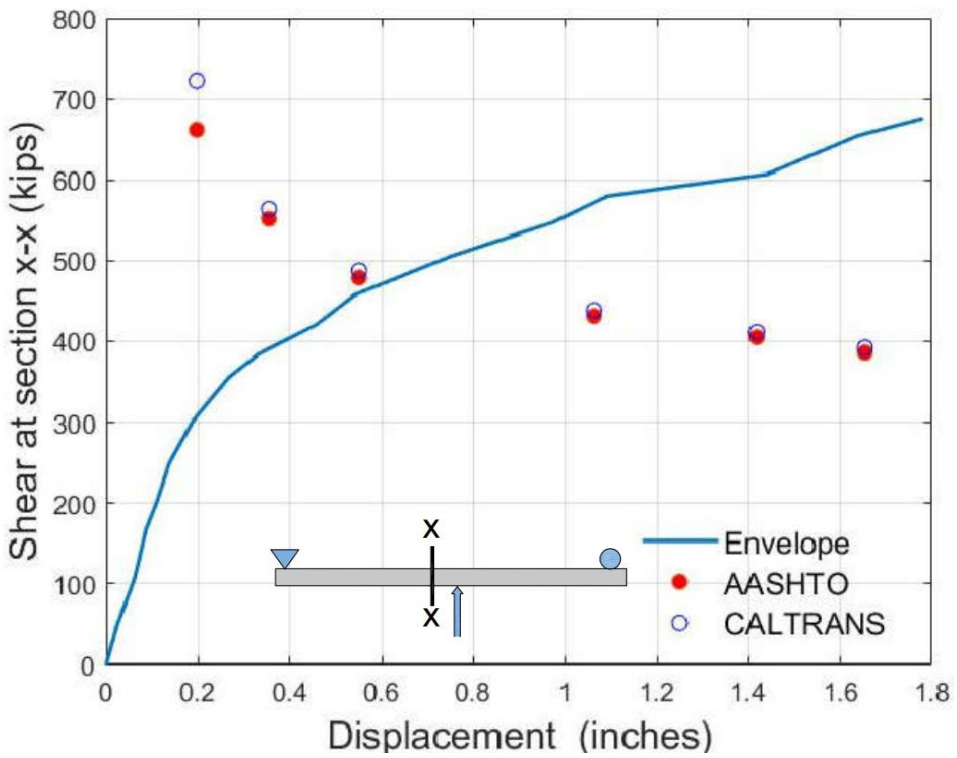

Figure 3.13: Shear capacity predictions versus actual shear resisted by specimen #1

Similar computations were carried out for specimen #2. As in the case of specimen #1, the centroidal strain ε_s was estimated during testing through linear interpolation of the measured strains across the depth of the section (see Figure 3.10 for specimen #2). The variation in the centroidal strain as a function of the shear at the critical section is displayed in Figure 3.14. Similar to the observation for the first specimen, it is evident that the AASHTO-based estimate of the strain converges to the measured value as the applied load approaches the shear capacity of the section. The inclination of the diagonal cracking during testing varied between 25° and 30° as shown in Figure 3.15. Once again, as was the case for the 1st specimen, the AASHTO estimate for the angle θ is significantly higher, as shown in Table 3.3.

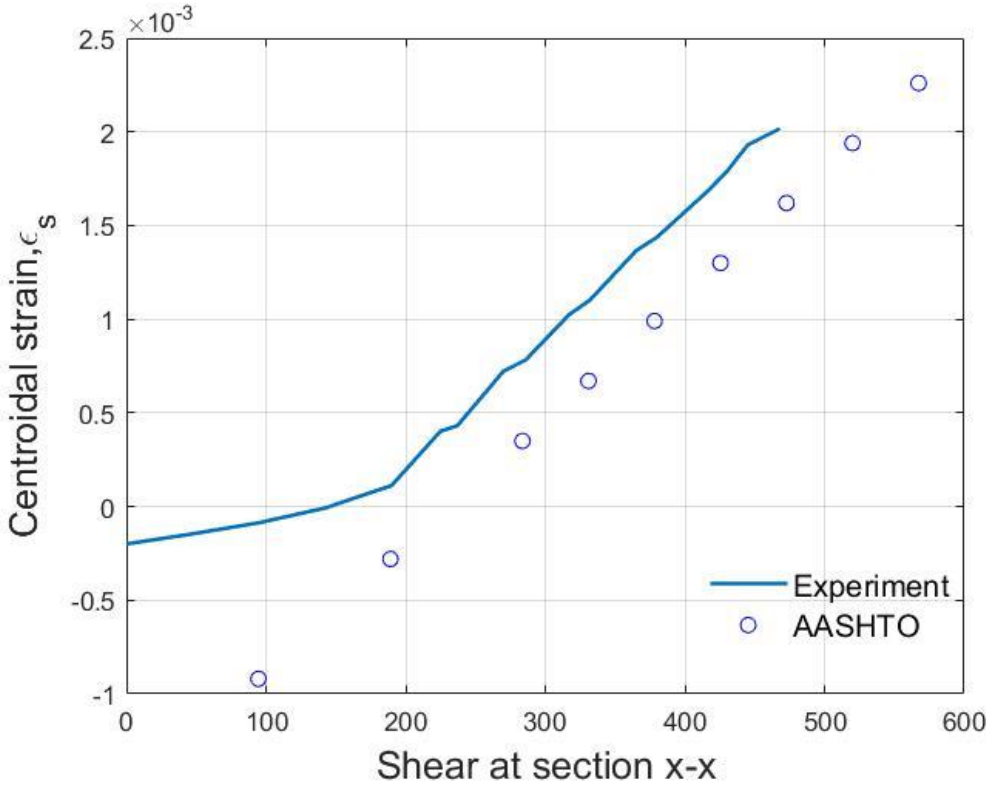

Figure 3.14: Measured centroidal strains versus AASHTO estimates (specimen #2)

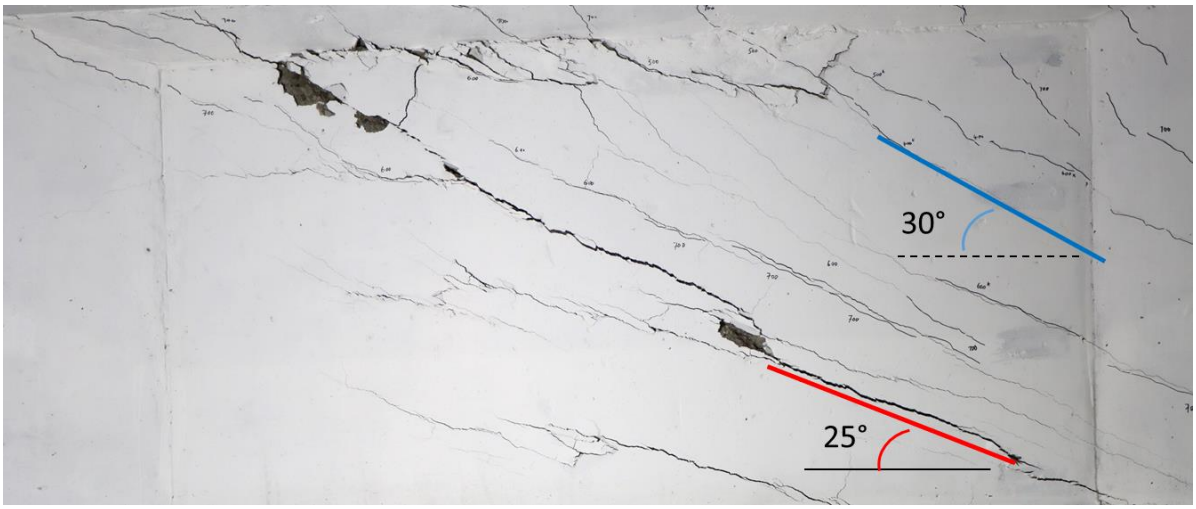

Figure 3.15: Observed inclination of diagonal cracks (specimen #2)

Table 3.3: Shear capacity estimate of specimen #2 with increasing load

Shear @ X-X	ε_s	θ	β	V_c	V_s	V_n
90	-0.0008	26.1	12.65	379.84	249.95	557.2
180	0.00019	28.3	5.61	168.47	227.2	395.67
270	0.00044	30.6	3.6	108.24	207.51	315.75
315	0.00076	31.7	3.06	91.82	198.61	290.44
360	0.00108	32.8	2.65	79.73	190.25	269.99
405	0.00139	33.9	2.35	70.45	182.38	252.84
450	0.00171	35.0	2.1	63.11	174.96	238.07
496	0.00203	36.1	1.9	57.15	167.93	225.08

A summary of the primary parameters used in the computation of the shear capacity V_n of the critical section is listed in Table 3.3. The Caltrans estimate is not shown in the table but is marginally higher for reasons mentioned in the discussion of specimen #1. The shear resisted by the critical section with increasing load is plotted in Figure 3.16 along with the shear capacity estimates based on both AASHTO and Caltrans specifications. The data from testing of specimen #2 suggest that the margin of safety between the Caltrans-based estimate and measured shear capacity is about 1.5, similar to the value obtained for specimen #1.

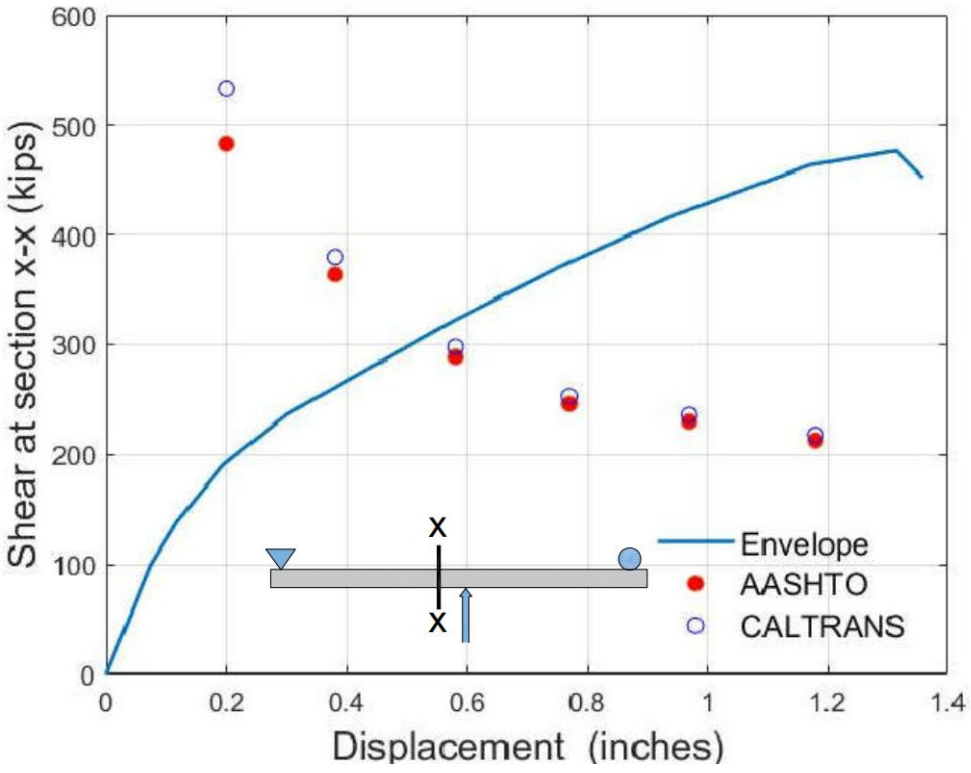

Figure 3.16: Shear capacity predictions versus actual shear resisted by specimen #2

4.0 NUMERICAL SIMULATIONS TO SUPPLEMENT EXPERIMENTAL STUDY

The commercial software ATENA (Cervenka et al.. 2020) was used in the numerical simulations. ATENA was developed to specifically simulate the behavior of concrete and reinforced concrete structures including concrete cracking, crushing and reinforcement yielding. Other features of the software that were also appealing for the present study was the ability to model reinforcing steel as discrete bars, incorporating bond failure and the ability to specify prestressing or post-tensioning. Additionally, when used with the GiD interface (https://gidhome.com), the development of the finite element mesh and post-processing capabilities are greatly enhanced. In this chapter, some of the salient features of ATENA are briefly described, followed by validation exercises and a parametric study to extend the findings of the experimental testing.

4.1 Constitutive Modeling

4.1.1 Concrete modeling

The concrete volume of the structural component is represented using continuum finite elements. As commonly done in structural concrete analyses, the elastic and inelastic behavior of the concrete under loading is modeled by stress versus strain relationships defined at the integration points of the finite elements. In ATENA, these constitutive relationships account for tensile fracture, plastic behavior in compression, and transitional behavior for intermediate stress conditions. Limiting surfaces are used to define the boundary between elastic and inelastic

behavior. The Menétrey-Willam failure surface is employed in the current version of the concrete material model in ATENA as shown in Figure 4.1.

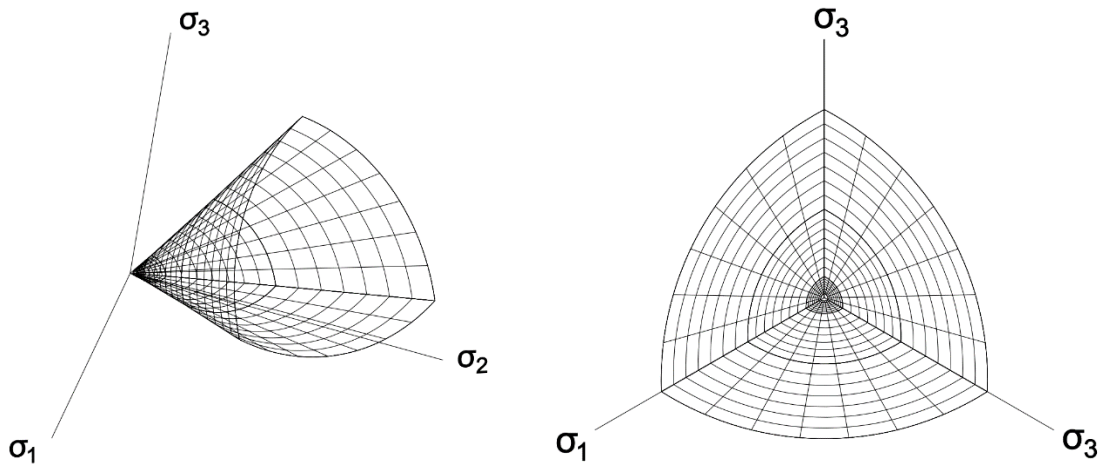

(a) **(b)**

Figure 4.1: Menétrey-Willam failure criterion in:
(a) 3D stress space; (b) deviatoric plane

The Menétrey-Willam failure surface function F_{3p}^{p} is represented in the Haigh-Westergaard coordinates with three parameters as:

$$F_{3p}^{p} = \left[\sqrt{1.5}\frac{\rho}{f_c}\right]^2 + m\left[\frac{\rho}{\sqrt{6}f_c}r(\theta,e) + \frac{\xi}{\sqrt{3}f_c}\right] - c = 0 \tag{4.1}$$

where $m = 3\frac{f_c^2 - f_t^2}{f_c f_t}\frac{e}{e+1}$ is the cohesive parameter of the material, and

$$r(\theta,e) = \frac{4(1-e^2)\cos^2\theta + (2e-1)^2}{2(1-e^2)\cos\theta + (2e-1)[4(1-e^2)\cos^2\theta + 5e^2 - 4e]^{\frac{1}{2}}} \tag{4.2}$$

represents an elliptical function. In above equations, f_c and f_t are the uniaxial compressive strength and tensile strength, respectively. The parameter $c \in (0,1)$ determines the evolution

direction of Menétrey-Willam failure surface towards either hardening or softening during the yielding/crushing process of the material. The parameter $e \in (0.5,1)$ defines the curvature of the surface, with a recommended value of 0.52 leading to an equivalent biaxial concrete strength of $1.14f_c$. The failure surface of Menétrey-Willam criterion will form angles (or discontinuities in slope) in the deviatoric plane if *e* is set as 0.5, whereas a continuous circle is obtained for $e = 1$ as shown in Figure 4.2.

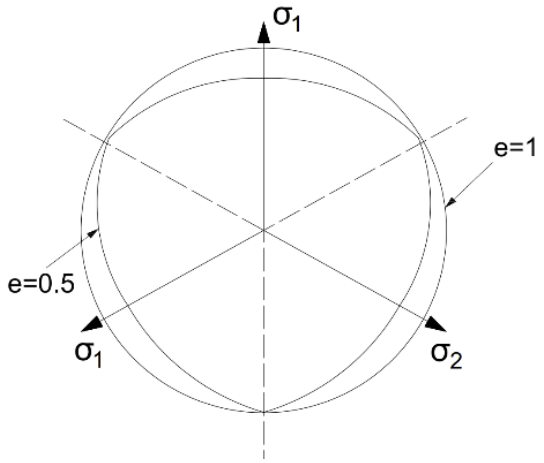

Figure 4.2: Effect of parameter *e* on the failure surface in the deviatoric plane

With respect to tensile fracture, a Rankine failure criterion is used, as shown in 3-D stress space in Fig. 4.3. When the major principal stress at a point within the concrete (i.e., at an integration point of the finite element model) violates the Rankine limiting surface, fracture occurs. The Rankine failure criterion can be written as:

$$F_k^f = \sigma_{ij} \cdot n_i \cdot n_j - f_t \leq 0 \tag{4.3}$$

In Haigh–Westergaard coordinates, this becomes:

$$F^f = \xi - \sqrt{2} \cdot \rho \cdot \cos\theta - \sqrt{3} \cdot f_t \leq 0 \tag{4.4}$$

where

$$\xi = \sqrt{3}I_1, \rho = \sqrt{2J_2}, \cos(3\theta) = \frac{3\sqrt{3}}{2}\frac{J_3}{J_2^{\frac{3}{2}}} \tag{4.5}$$

In above equations, the stress invariant $I_1 = \sigma_{ii} = \sigma_1 + \sigma_2 + \sigma_3$, denoting the summation of the principal stresses. The stress invariants J_2 and J_3 can be expressed in the unified form $J_i = \frac{1}{i}Tr(\sigma^i)$, with σ^i referring to the i^{th} order double dot product of the stress tensor σ_{ij}.

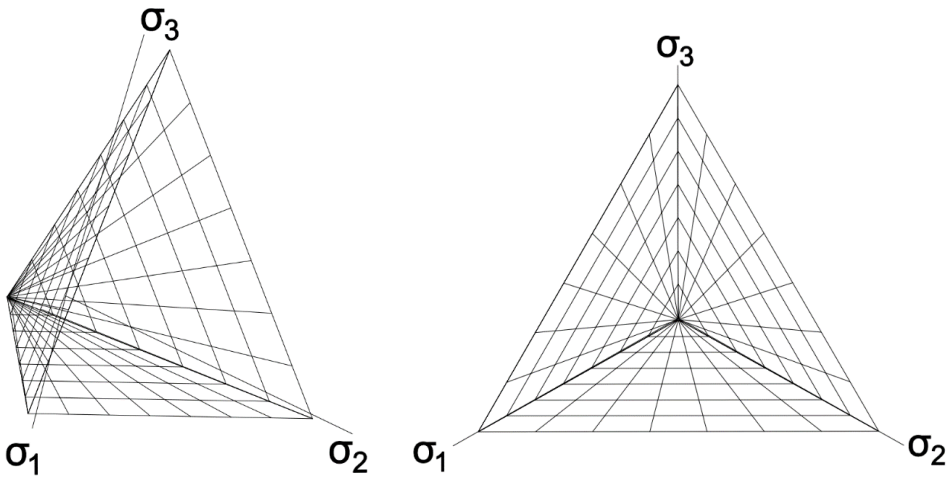

(a) (b)

Figure 4.3: Rankine failure surface: (a) 3D stress space; (b) deviatoric plane

ATENA combines the Rankine criterion and the Menétrey-Willam criterion in order to simulate fracture and plasticity states simultaneously as shown in Figure 4.4. The process can be described as solving a set of inequalities from the failure surface criteria for the two surfaces as indicated below.

For the Menétrey-Willam criterion, the following inequality is solved for $\Delta\varepsilon_{kl}^{p}$:

$$F^p\left({}^{(n-1)}\sigma_{ij} + E_{ijkl}\left(\Delta\varepsilon_{kl} - \Delta\varepsilon_{kl}^{f} - \Delta\varepsilon_{kl}^{p}\right)\right) \leq 0 \tag{4.6}$$

For the Rankine criterion the following inequality is solved for $\Delta\varepsilon_{kl}^{f}$:

$$F^f\left({}^{(n-1)}\sigma_{ij} + E_{ijkl}\left(\Delta\varepsilon_{kl} - \Delta\varepsilon_{kl}^{p} - \Delta\varepsilon_{kl}^{f}\right)\right) \leq 0 \tag{4.7}$$

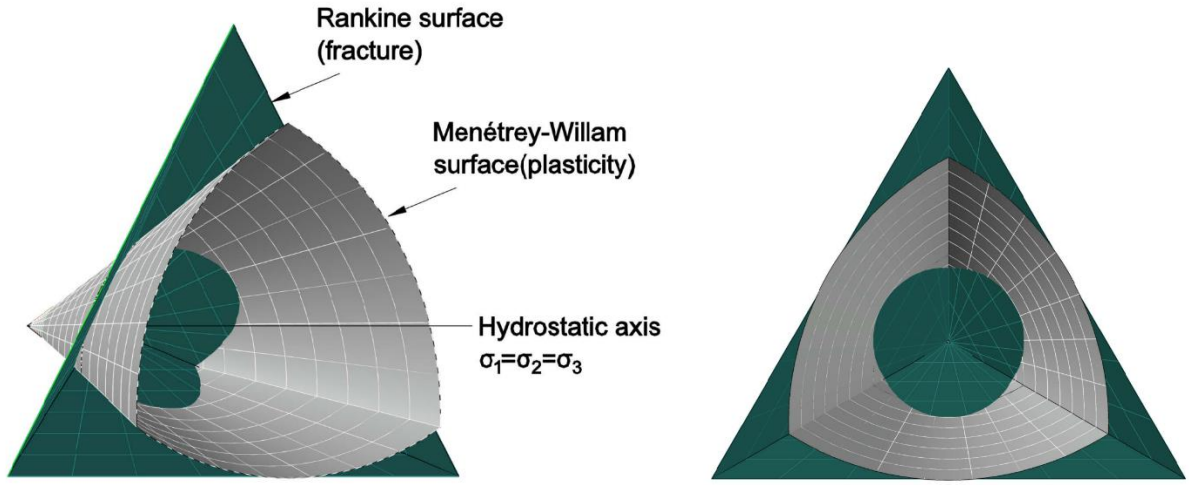

(a) (b)

Figure 4.4: Combined Rankine and Menétrey-Willam failure criteria: (a) 3D stress space; (b) deviatoric plane

In the above expressions, ${}^{(n-1)}\sigma_{ij}$ denote stress state from previous step, E_{ijkl} refers to elasticity matrix, and $\Delta\varepsilon_{kl}, \Delta\varepsilon_{kl}^{f}, \Delta\varepsilon_{kl}^{p}$ are defined as the total strain increment, fracture strain increment and plasticity strain increment, respectively. An iterative method is used to solve the above inequalities.

As a quasi-brittle material, concrete undergoes softening during tensile fracture. Such softening corresponds to a contraction of the limiting surface to the origin of the stress space. The contraction follows a prescribed softening relationship, as a function of crack width (as shown in Fig. 4.5). The stress vs. crack opening relationship employed by ATENA is:

$$\frac{\sigma}{f_1^t} = \left\{1 + \left(c_1 \frac{w}{w_c}\right)\right\} exp\left(-c_2 \frac{w}{w_c}\right) - \frac{w}{w_c}(1 + c_1^3) exp(-c_2) \qquad (4.8)$$

where $w_c = 5.14 \frac{G_f}{f_t^t}$

In the above expression, w is crack opening, w_c is the traction free crack opening and f_t is the uniaxial tensile strength of the concrete. The coefficients c_1 and c_2 are assigned values of 3.0 and 6.93, respectively, in accordance with experimental results (Hordijk, 1991). The area under the softening curve, G_f, is the so-called fracture energy, which is the energy required to form a unit area of traction-free crack.

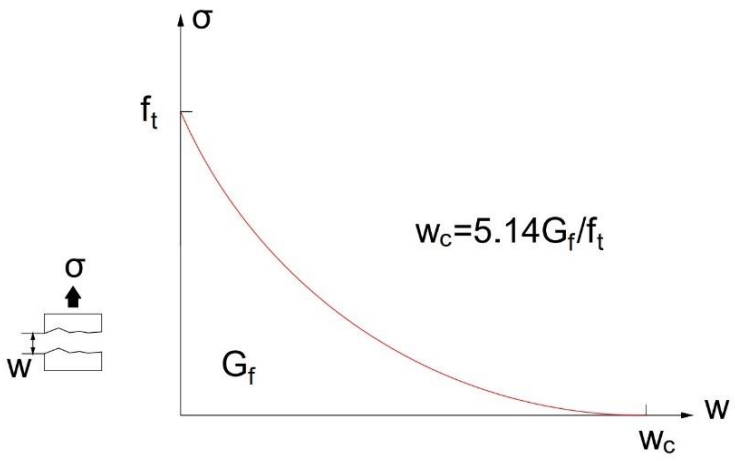

Figure 4.5: Tensile stress versus crack opening relationship

A smeared cracking approach is used to model fracture within the finite element formulation. In other words, the crack opening *w* is assumed to be uniformly distributed (or smeared) over the concrete region represented by a given integration point. The stress-strain constitutive relations are formulated such that the softening curve, and thus also fracture energy, are preserved during tensile fracture. In this way, the finite element results are objective with respect to changes in mesh size (Bazant and Oh, 1983). There are two common forms of the smeared cracking approach: 1) fixed crack model; and 2) rotating crack model. When using the fixed crack model, the direction of cracking is set normal to the direction of principal tensile stress at the instant of crack initiation. The direction of cracking does not change during the

course of the analysis, even though the directions of stress or strain may rotate. This situation is pictured in Fig. 4.6 a, where the cracked concrete element typically carries both normal stress and shear stress; axes m_1 and m_2 define the direction of material orthotropy.

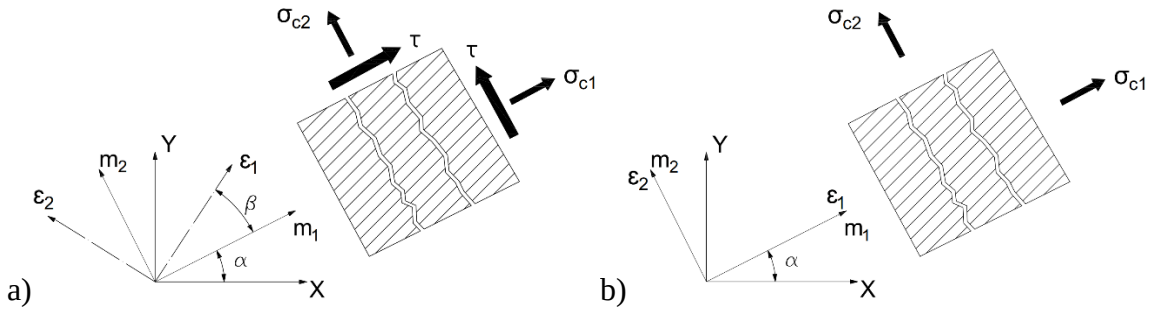

Figure 4.6: Conventional smeared cracking models:
a) fixed crack option; b) rotating crack option

In principle, the fixed crack option corresponds to the case of a physical crack, whose orientation remains fixed. However, two complications may arise when applying fixed crack models: 1) the ultimate direction of cracking at a given point might not coincide with the direction set at fracture initiation; and 2) there is a tendency for ensembles of integration points undergoing cracking to "stress lock", causing additional consumption of fracture energy (i.e., in excess of that defined by the softening relation). The rotating crack option (Fig. 4.6 b) offers an artificial means for addressing these concerns. The constitutive relations are formulated such that the local direction of cracking remains normal to the prevailing direction of principal tension. In this situation, the cracked element does not carry shear stress and the directions of principal strain and stress are coaxial.

ATENA offers a means for balancing both the want of physical basis and practical needs in simulating tensile fracture. Users may set a residual stress level at which the direction of

cracking is fixed, rather than having the direction fixed at the instant of fracture initiation. This allows for user specified transition between the two smeared cracking options. With respect to modeling the behavior of concrete in compression, and multi-axial stress states in general, ATENA employs a limiting surface to distinguish elastic and inelastic stress regimes. As indicated previously, the limiting surface is specified by the Menétrey-Willam criterion for concrete under triaxial states of stress (Menetrey and Willam, 1995). Cross-section views of the surface in 3-D stress space are shown in Fig. 4.7, where ξ is hydrostatic pressure, ρ is deviatoric stress, and angle θ indicates the position of the stress state in the deviatoric stress plane. Increments of stress within the limiting surface are assumed to be linear elastic; increments that violate the limiting surface are assumed to be elastic-plastic. ATENA uses conventional algorithms for returning the stress state to the limiting surface, such that the stress state stays on the limiting surface during plastic loading. Additional details are supplied by the ATENA documentation and the supporting literature.

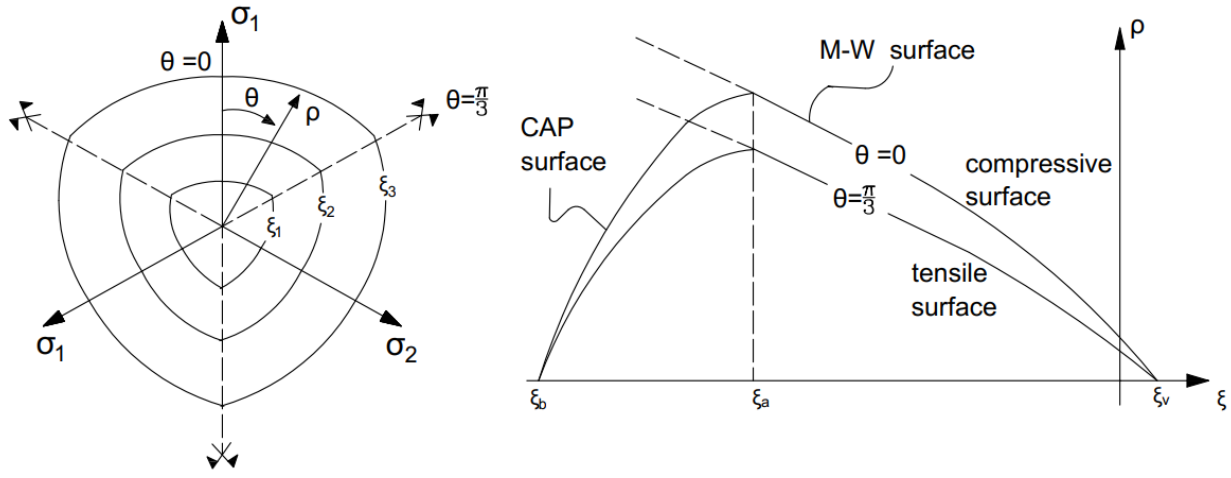

(a) (b)

Figure 4.7: Triaxial limiting surface of Menétrey-Willam with a cap:
a) deviatoric sections at three intermediate values of hydrostatic pressure;
b) compressive and tensile meridians in the Rendulic plane

4.1.2 Reinforcement modeling

Reinforcing steel bars are modeled using uniaxial truss elements with a multi-linear stress-strain relationship as shown in Figure 4.8. A yield plateau can be specified by setting f_1 and f_2 to have the same magnitude. The 4th point on the relationship can be omitted. The reinforcing bar is assumed to rupture at the maximum specified ultimate stress. Additionally, the same behavior is assumed in both tension and compression. Since bar buckling is not expected in the girder simulations, this assumption is reasonable for the present study.

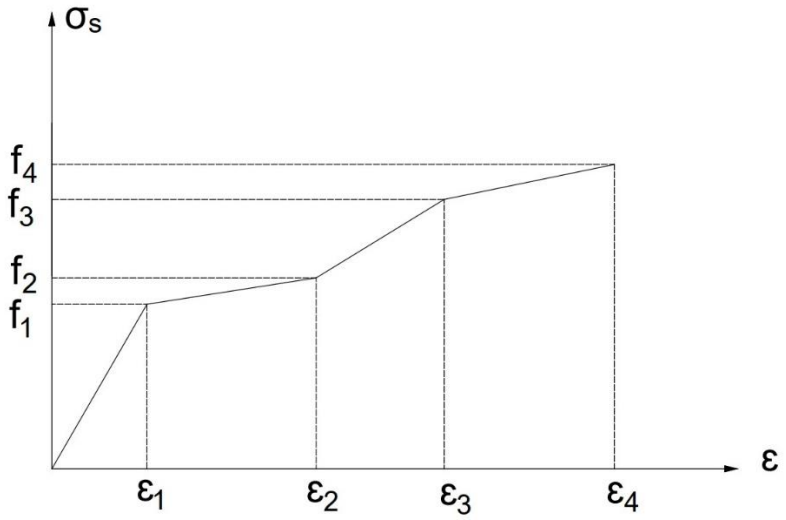

Figure 4.8: Multi-linear stress-strain relationship for reinforcing steel

4.1.3 Bond and Interface Modeling

Within the ATENA package, the nodes of the truss elements representing reinforcing steel bars are related to the concrete element nodes in a way that allows for the explicit modeling of bond slip (i.e., slippage between the steel bars and the surrounding concrete). This capability is particularly important in the neighborhood of cracks and in anchorage zones, where bond

stresses and the potential for slip are high. Program users specify a bond shear stress versus slip relationship, which can reflect details of the reinforcing steel bar, degree of bar confinement, and other relevant factors.

4.2 Panel Test Simulations

Panel tests have been used to assess the influence of post-tensioning ducts on the shear resistance of concrete bridge girders. The panel specimens represent a portion of the diagonal compression struts that form in the girder web due to shear-induced cracking. In one prominent study, Muttoni et al. (2006) conducted a series of tests on 16 panel specimens with dimensions of 23.6 x 23.6 x 4.9 in. (600 x 600 x 125 mm). The panels were subjected to pure compressive loading to investigate the effect of the presence of various types of post-tensioning ducts on the strength of the compression struts. Some of the tested panels were extracted from an actual bridge girder, which had been previously loaded, allowing investigation of the effect of web cracking on the ultimate strength. In the present study, however, only panels cast in the laboratory were considered. Cross-sectional details of the panel are shown in Figure 4.9.

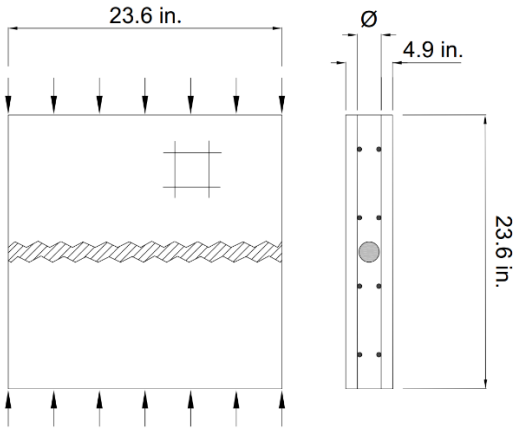

Figure 4.9: Panel specimen configuration

The panels constructed in the laboratory contained a reference specimen without a duct as well as specimens with various types of ducts: empty duct, grouted steel duct and grouted HDPE duct. The panels considered in the present study included: a reference panel without a duct (Panel W3), a panel with a grouted steel duct (Panel W5), a panel with an ungrouted (empty) duct (Panel W7), and a panel with a grouted HDPE duct (Panel W10). Finite element models of the different panels including the reinforcement details are displayed in Figure 4.10.

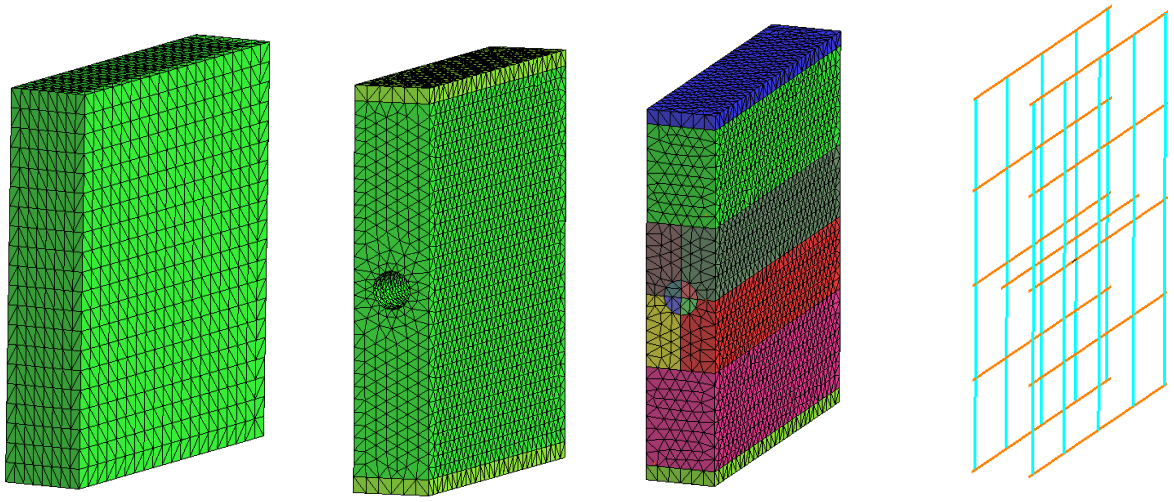

(a) (b) (c) (d)

Figure 4.10: ATENA models of the panels showing the FE mesh and reinforcement: (a) control panel; (b) panel with empty duct; (c) panel with grouted duct; (d) reinforcement

Material properties used in the simulation were taken from the paper by Muttoni et al. (2006) and are listed in Table 4.1. The following properties were specified for all the reinforcing steel: yield strength = 73.8 ksi, ultimate strength = 86.6 ksi and a Young's modulus of 29,300 ksi. An interface material was specified between the grout and concrete with a normal and tangential stiffness of 30,000 ksi, a tensile strength of 0.22 ksi, a material cohesion parameter of 0.435 and friction factor 1.3.

Results of the simulation are compared with experimental findings in Figure 4.12 where it is seen that the ATENA models satisfactorily reproduce the observed experimental responses. With the exception of Panel W7, the FE simulations tend to slightly overestimate the shear capacity of the panels. In general, these simulations provide confidence in the ability of ATENA and the selected material parameters to reasonably capture the overall behavior of reinforced concrete components failing in shear.

Table 4.1: Material properties specified in the panel simulations

Property	**Concrete**				**Grout**
	Panel W3	*Panel W5*	*Panel W7*	*Panel W10*	
Compressive strength (ksi)	5.30	5.40	5.30	5.40	4.67
Tensile strength (ksi)	0.38				0.35
Young's modulus (ksi)	4200				3900
Fracture energy (k/in)	0.00041				0.0006
Plastic strain (ε_{cp})	-0.0013				-0.0012
Onset of crushing, f_{co} (ksi)	-0.80				-0.735

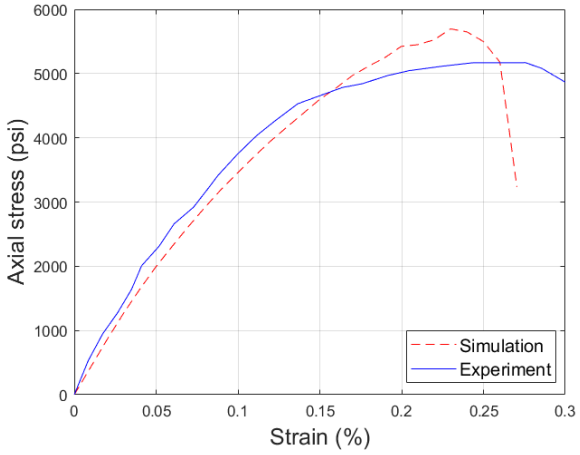

(a) Panel W3

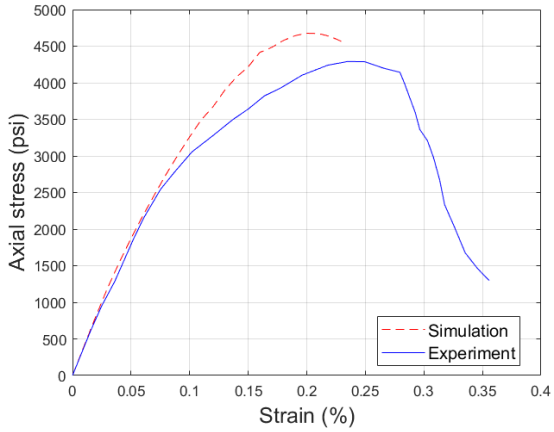

(b) Panel W5

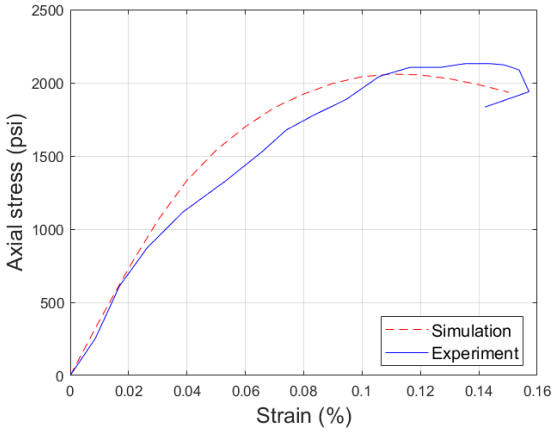

(a) Panel W7

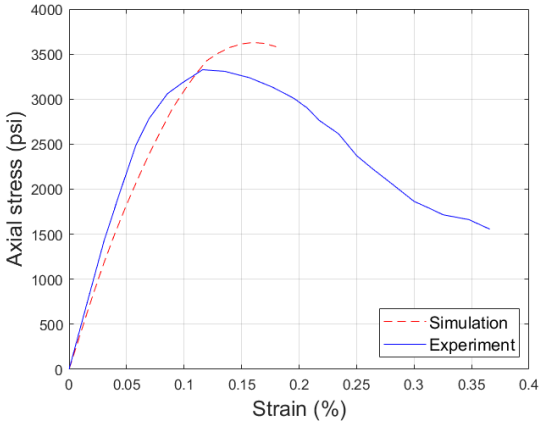

(b) Panel W10

Figure 4.11: Numerically simulated versus observed experimental responses from panel tests carried out by Muttoni et al. (2006).

4.2.1 Girder Test Simulations

The number of physical tests of the post-tensioned girder specimens, as described in the preceding sections, was limited to two by practical constraints, including the project duration. Herein, the ATENA finite element package is used to simulate each of the girder tests. After these benchmark comparisons with the physical test results, ATENA models are used for parametric study of the influences of duct size and the bundling of ducts within the girder web.

4.3.1 Girder Specimen #1

The finite element discretizations of girder specimen #1 are shown in Fig. 4.12. All steel reinforcement, including the post-tensioning system, are explicitly represented within the finite element model. Routines provided by ATENA were used to prestress the steel elements within the prestressing duct, based on the values measured during the post-tensioning operation. As done during the test program, loads are applied to the specimen via steel bearing plates, which are also represented by the finite element model. Upward loading is applied via displacement control near mid-span and the end supports restrain vertical movement, while allowing free rotation.

The simulated load-displacement response of specimen #1 is compared with the experimental response in Fig. 4.13. The shear force acting over the region of interest (i.e., the panel zone on the left side of the girder) is determined from the applied load and support reactions. The model captures the main features of the experimental response curve, including the initial elastic branch, the transition to nonlinear behavior, and the gradual loss of stiffness as the load is increased. As previously noted, the physical test was halted prior to specimen failure due to limitations in the capacity of the loading frame. The numerical model was loaded up to V = 667 kips, where the solution process failed to converge. Loss of convergence was due, in part, to extensive damage and loss of load carrying capacity in the shear panel zone.

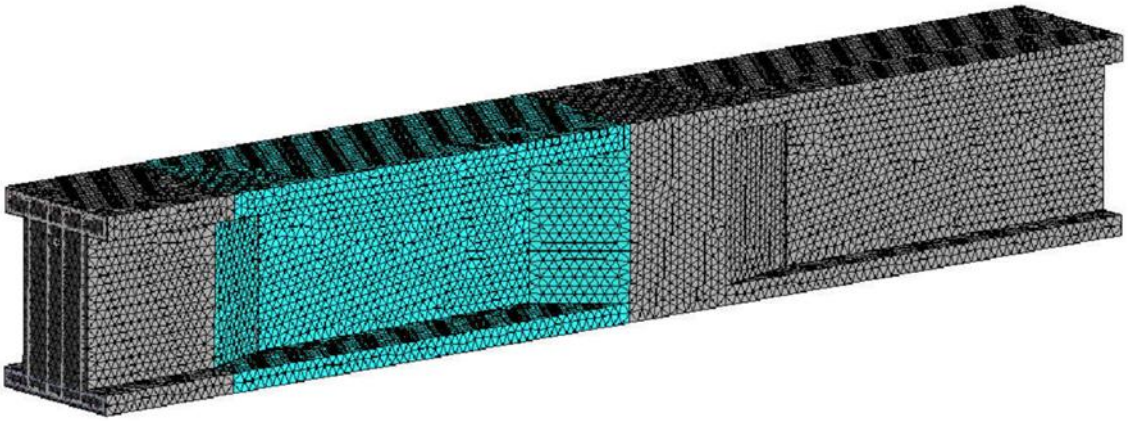

(a)

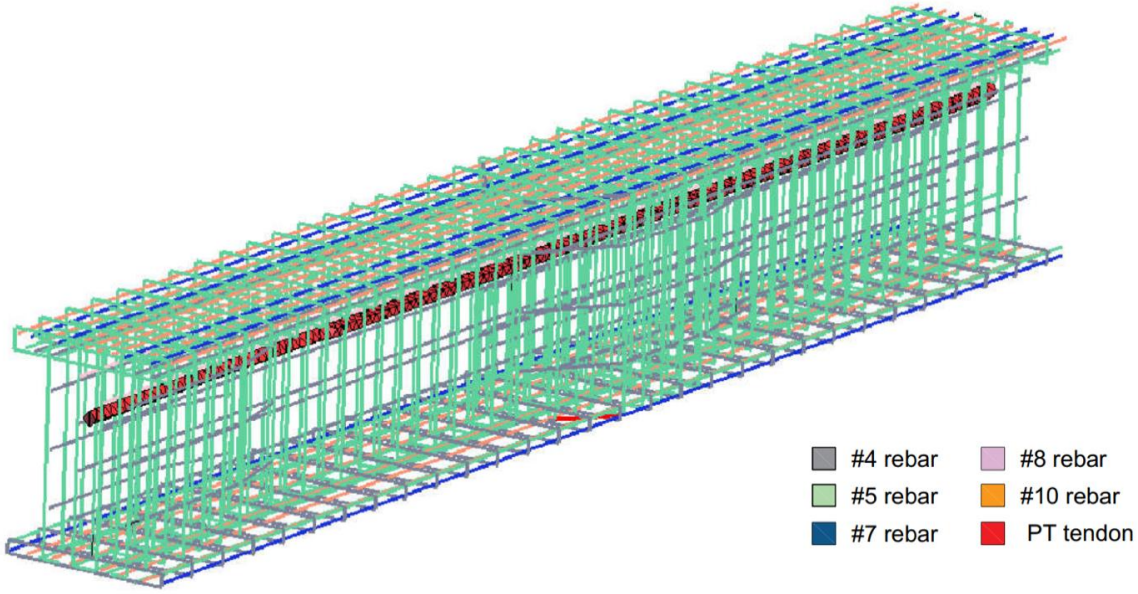

(b)

Figure 4.12: Discretization of: (a) post-tensioned girder specimen #1; and (b) reinforcing steel, including the post-tensioning system

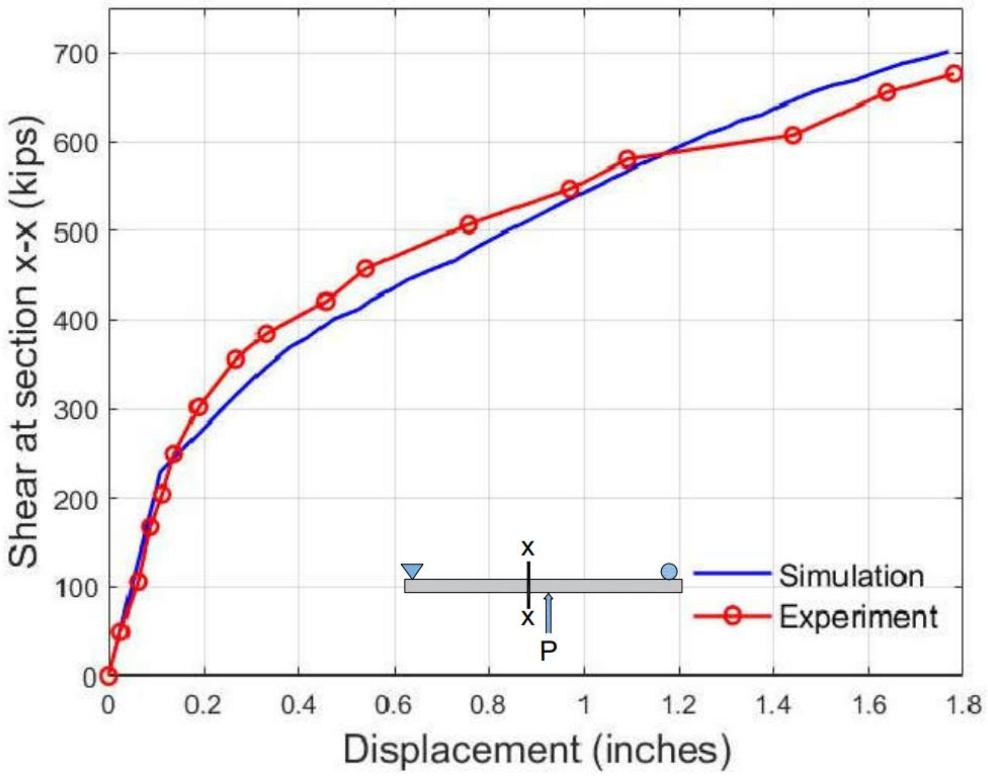

Figure 4.13: Observed and simulated load-displacement responses of specimen #1

Figure 4.14 presents simulated damage patterns at several stages of loading. Flexural cracking appears at about V = 250 kips. Flexural cracking developed over the mid-portion of the beam, both along the region of interest and the other side of the specimen, as observed during the physical test. The appearance of shear type cracking occurs around V = 440 kips (see Fig. 4.14 a). The crack indicators, shown on the deformed mesh, indicate crack strain at the integration points of the finite elements has exceeded a prescribed threshold value. With increased loading, shear cracking continues to develop throughout the region of interest, while the flexural cracking is relatively limited. The model eventually loses load carrying capacity due to accumulation of damage in the shear panel zone and its advancement toward the supports.

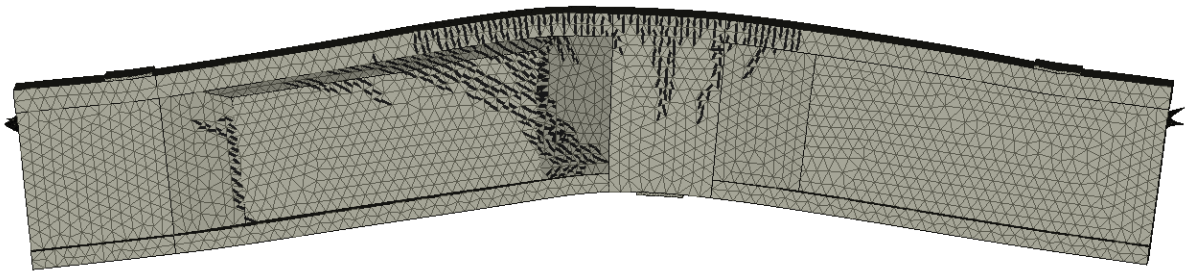

(a)

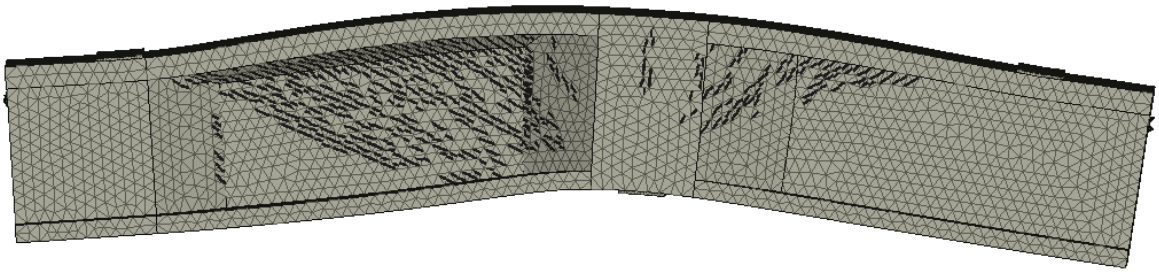

(b)

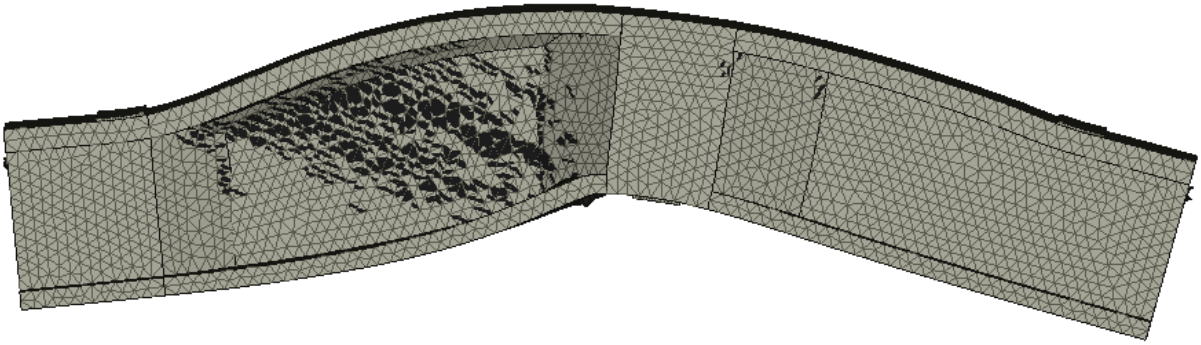

(c)

Figure 4.14: Deformed mesh showing damage patterns at several load stages: a) V = 440 kips; b) V = 608 kips; and c) V = 667 kips

The progression of damage in the girder model can also be seen in terms of crack width distributions, as presented in Fig. 4.15. Fracture strains calculated at the element integration points are integrated over the corresponding element volumes to obtain measures of crack width. Similarly to the information provided in Fig. 4.14, the crack width maps shown in Fig. 4.15 portray the advancement of diagonal cracking leading to shear failure of the girder. In both sets of results shown in Figs. 4.14 and 4.15, the positioning of the post-tensioning duct does not seem to significantly influence the damage patterns.

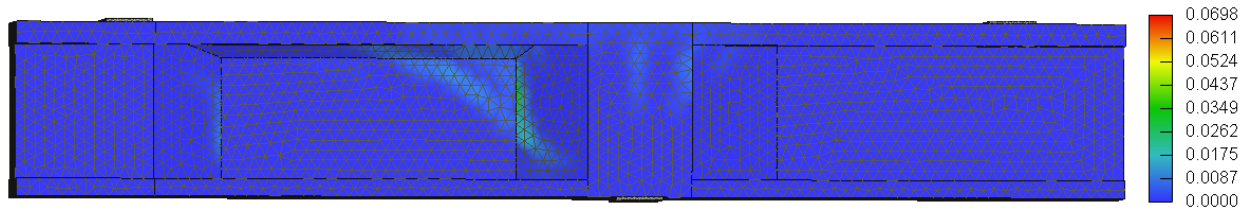

(a)

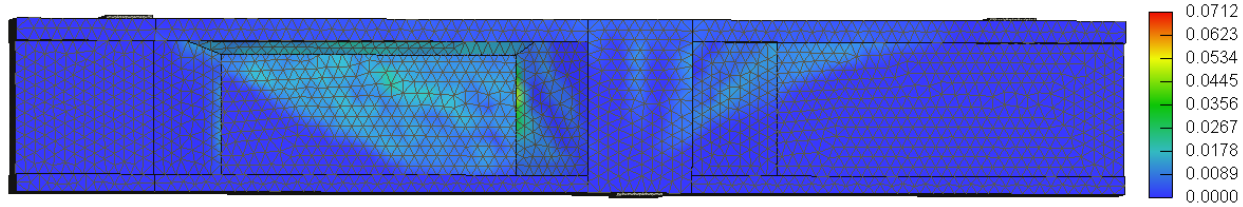

(b)

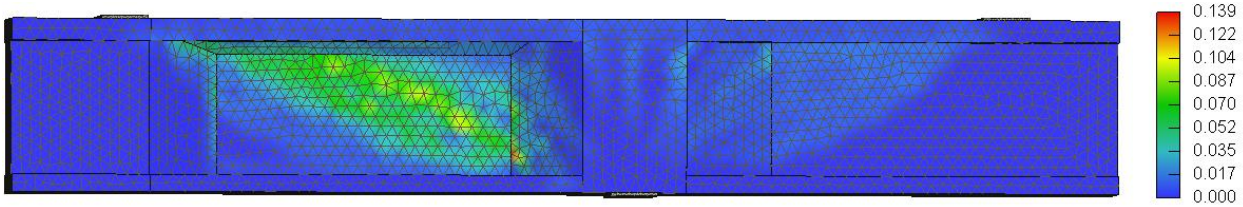

(c)

Figure 4.15: Distribution of crack width (in inches) at several load stages: a) *V* = 440 kips; b) *V* = 608 kips; and c) *V* = 667 kips

Figure 4.16 shown contours of minimum principal stress on a cross-section within the critical zone of the girder. At the intermediate load level of V = 450 kips, the distribution of stress meets expectations for flexural behavior with the lower portion of the girder carrying compression. Approaching the failure load, the localization of high compressive stress near the junction of the web and lower flange is evident in Fig. 4.16 b, as would be expected for shear failure.

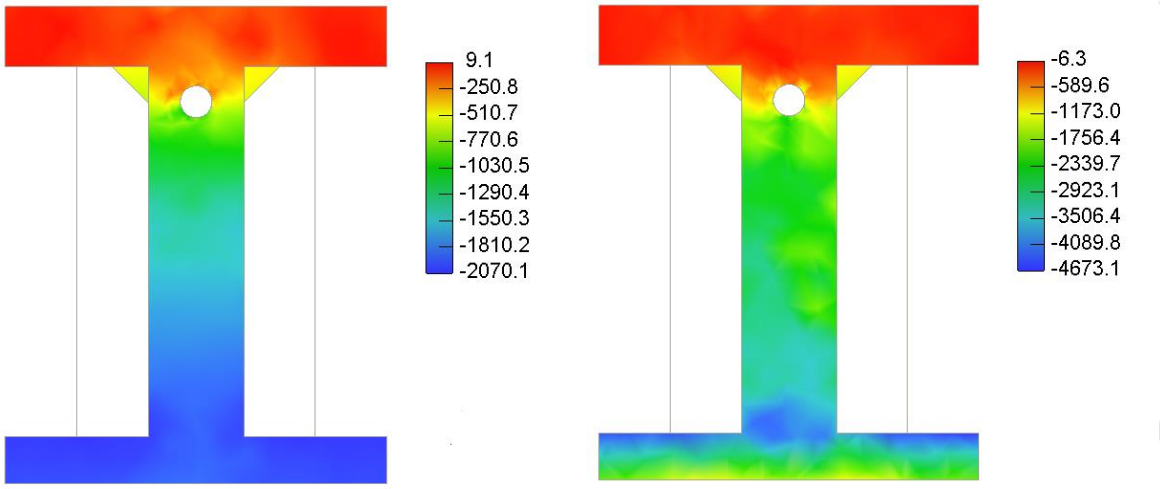

(a) (b)

Figure 4.16: Minor principal stresses (in psi) at critical section at: (a) V = 450 kips; and (b) V = 667 kips

4.2.2 Girder Specimen #2

The finite element discretizations of girder specimen #2 are shown in Fig. 4.17. As noted in Section 3, both the section depth and web thickness of Specimen 2 are reduced, relative to those

of specimen 1. In addition, specimen #2 included multiple post-tensioning ducts (though strands were included only in the top two ducts), as evident in Fig. 4.17 b.

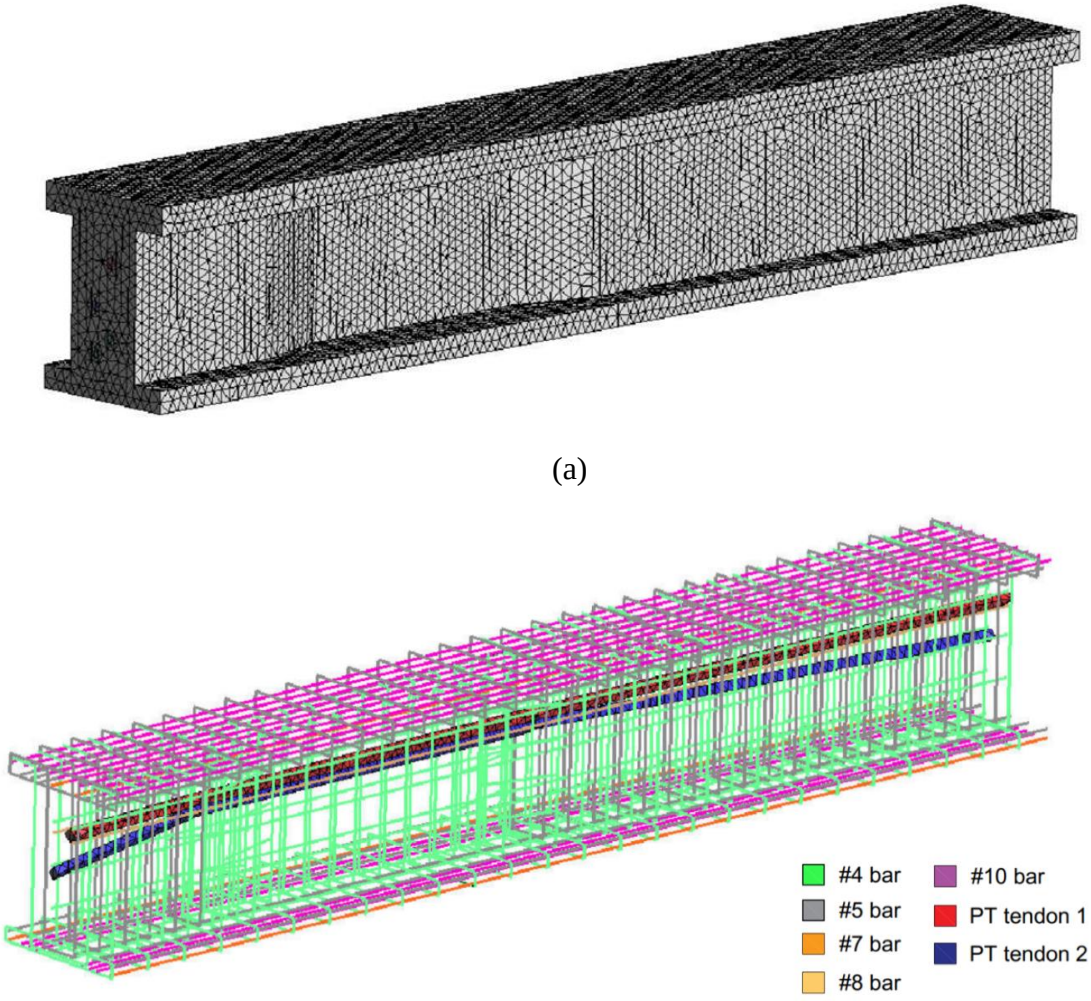

(a)

(b)

Figure 4.17: Discretization of: (a) post-tensioned girder specimen #2; and (b) reinforcing steel, including the post-tensioning ducts

Displacement controlled loading was applied to the numerical specimen, corresponding to what was done during the physical tests. The simulated load versus displacement response is compared with that of the test girder in Fig. 4.18. From this comparison, it can be said that the

numerical model captures the global load-displacement behavior of the girder, including the peak load.

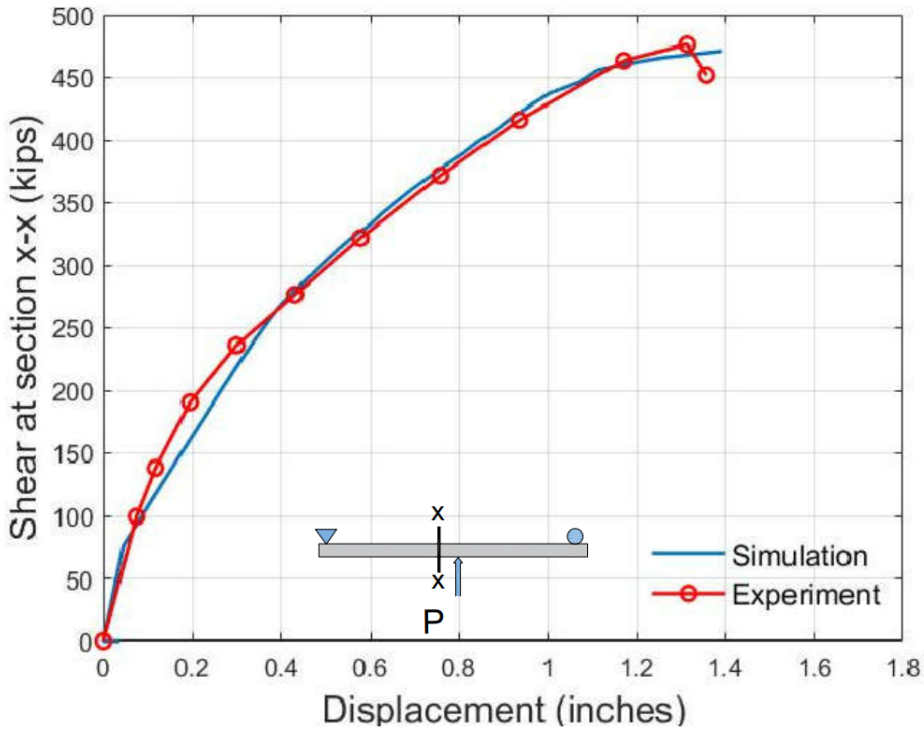

Figure 4.18: Observed and simulated load-displacement responses of specimen #2

Figure 4.19 shows the deformed mesh and crack strain indicators at several load stages. Both flexural and shear cracking are evident at intermediate levels of loading. As for the simulation of specimen #1, damage ultimately localizes within the panel region on the left side of the girder. The crack strain indicators appear when the crack strain values exceed a threshold value, set in relative terms, such that the damage on the right side of the specimen does not appear at higher load levels (Fig. 4.19 c). The localization of damage is also evident when looking at plots of crack opening, as shown in Fig. 4.20. Approaching peak load, the crack widths are roughly an order of magnitude greater than at intermediate load levels, with the highest openings occurring in the lower part of the web. Compared to the corresponding results

for the case of one post-tensioning duct within the girder section, in Figs. 4.14 and 4.15, these results for multiple ducts exhibit a qualitatively different damage pattern. In particular, the damage patterns seen in Figs. 4.19 and 4.20 are broader and, in some locations, appear to run along the tendon trajectories. However, it is difficult to make direct comparisons between the one- and multiple-duct cases, since the specimen cross-section dimensions are also different, with specimen 2 being significantly downsized relative to specimen #1.

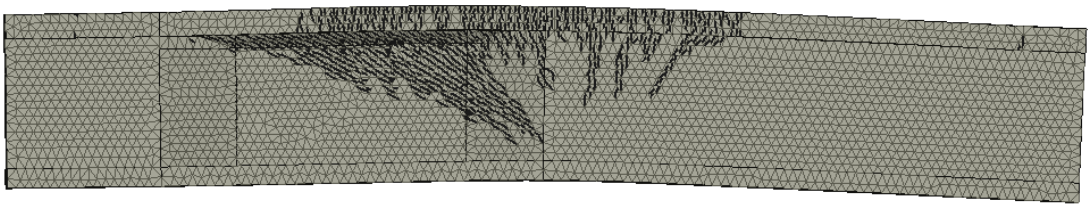

(a)

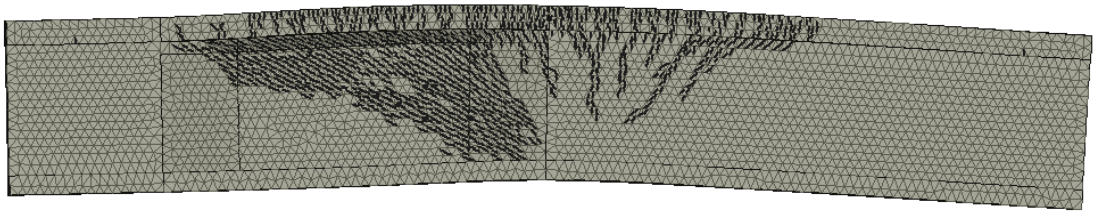

(b)

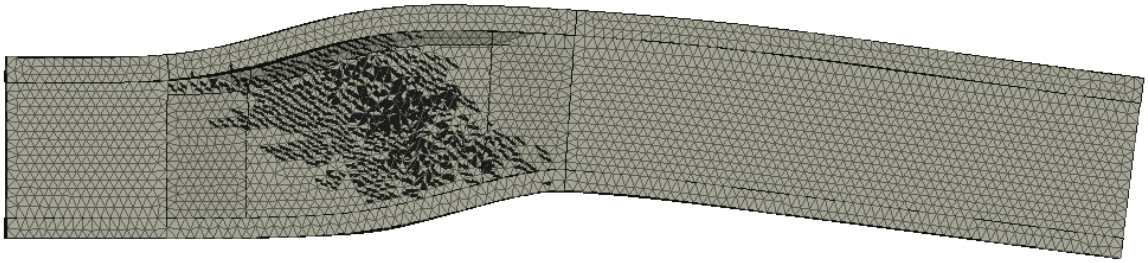

(c)

Figure 4.19: Deformed mesh showing damage patterns at several load stages: a) *V* = 335 kips; b) *V* = 380 kips; and c) *V* = 464 kips

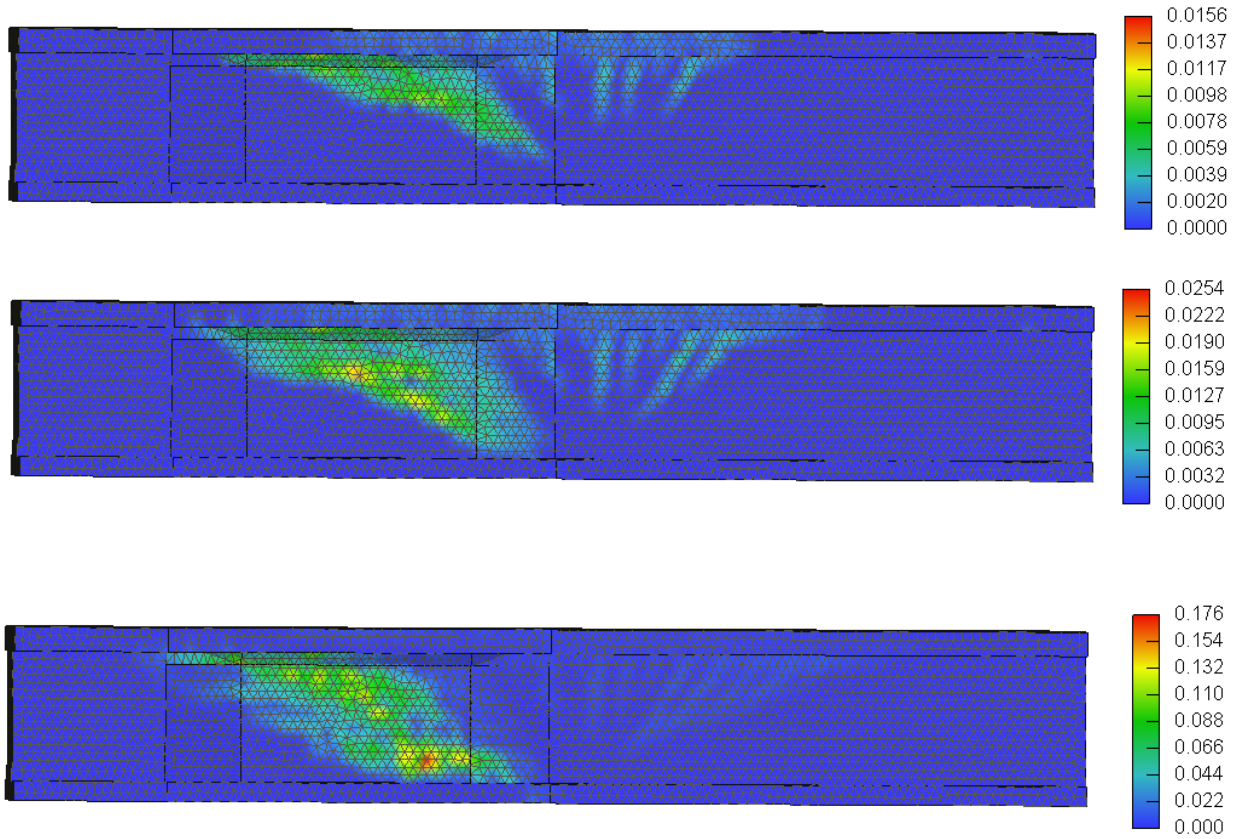

Figure 4.20: Distribution of crack width (in inches) at several load stages: a) *V* = 335 kips; b) *V* = 380 kips; and c) *V* = 464 kips

Figure 4.21 shows contours of minimum principal stress for a cross-section within the critical zone for two stages of loading. As seen for the simulations of specimen #1, large compressive stresses ultimately form local to the web-flange juncture. Moreover, these stress contours (and those of major principal stress, as well) do not indicate high stresses in the neighborhood of the post-tensioning ducts. This suggests a relatively low potential for distress local to the post-tensioning ducts, but additional modeling efforts are needed to confirm that characterization of behavior. As shown in the elevation views of panel damage in Fig. 4.19 c, for example, it appears that the presence of multiple post-tensioning ducts may affect the damage patterns approaching peak load.

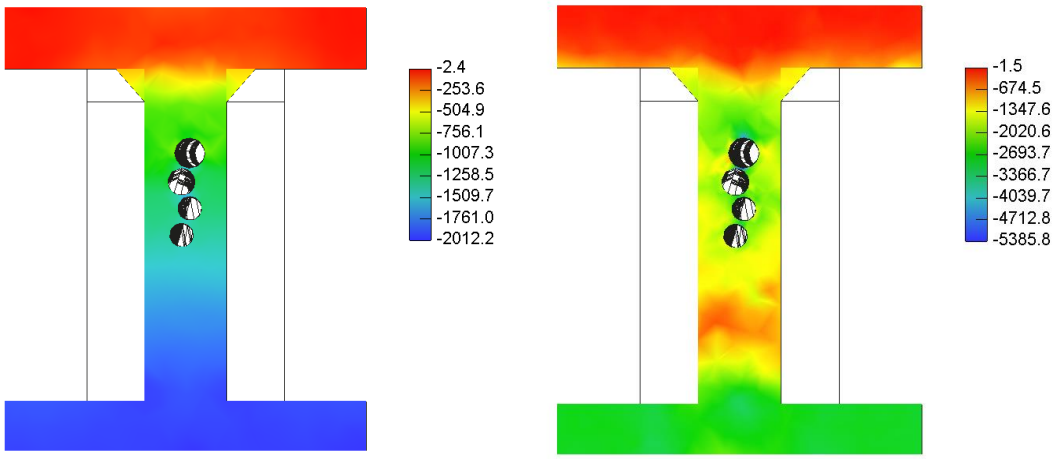

(a) (b)

Figure 4.21: Minor principal stresses (in psi) at critical section at: (a) V = 300 kips; and (b) V = 450 kips

4.3 Parametric Studies on Influences of Duct Size and Bundled Ducts

Accuracy of the finite element modeling approach, based on the ATENA software package, has been demonstrated through the preceding comparisons with experimental results. The modeling approach is now used for parametric studies of the influences of duct size and the bundling of ducts on the shear resistance of post-tensioned girders. As shown in Fig. 4.22, the girder configuration is similar to that of specimen 1, except that the flange widths have been increased to 90 in. (compared to 48 in. for specimen 1) and the total span length has been increased to 40 ft. (compared to 32 ft. for specimen 1). To accommodate the larger flange widths, the effective post-tensioning force was increased to maintain the value of about 0.2 $f_c A_g$.

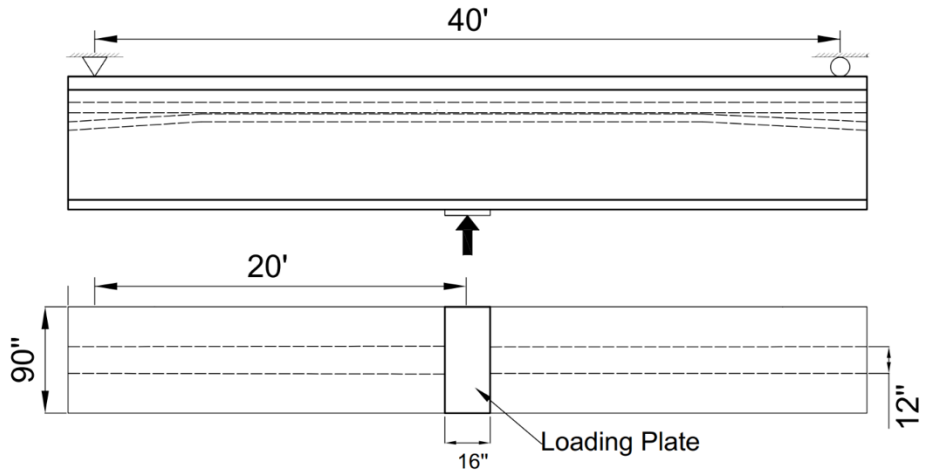

Figure 4.22: Elevation and plan view of girder specimen considered in parametric study

4.3.1 Effect of Number of Bundled Ducts

Three configuration (consisting of two, three and four bundled ducts) are considered. The duct layouts within the girder web are shown in Fig. 4.23. The duct arrangements follow those of current girder design practice. The prestressing tendons are distributed among the ducts of each configuration such that the total prestressing force of about $0.2\ f_c\ A_g$ is roughly the same between girder models. All ducts are assumed to be grouted.

When comparing the load-displacement responses in Fig. 4.24, one sees little differences between the results for each configuration. The cases of three and four post-tensioning ducts exhibit nonlinearity at a slightly lower load level, relative to that for one post-tensioning duct, as would be expected due to the slight lowering of the centroid of the prestressing force. Notably, the peak loads for each case are roughly the same. Additional analyses are needed for confirmation, but it appears that the peak loads are associated with failure of the diagonal compression struts, particularly in the lower part of the girder web. Distress local to the post-

tensioning ducts, as seen previously in Fig. 4.19 c for example, does not seem to be a primary factor in determining specimen failure.

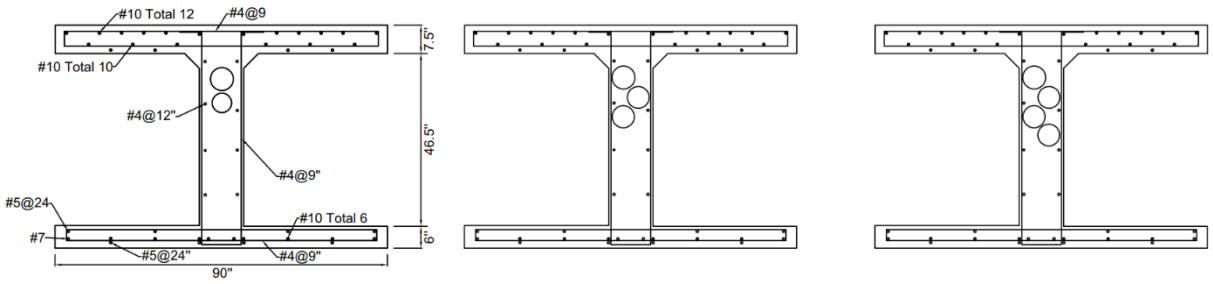

Figure 4.23: Cross-sections showing variation in number of ducts

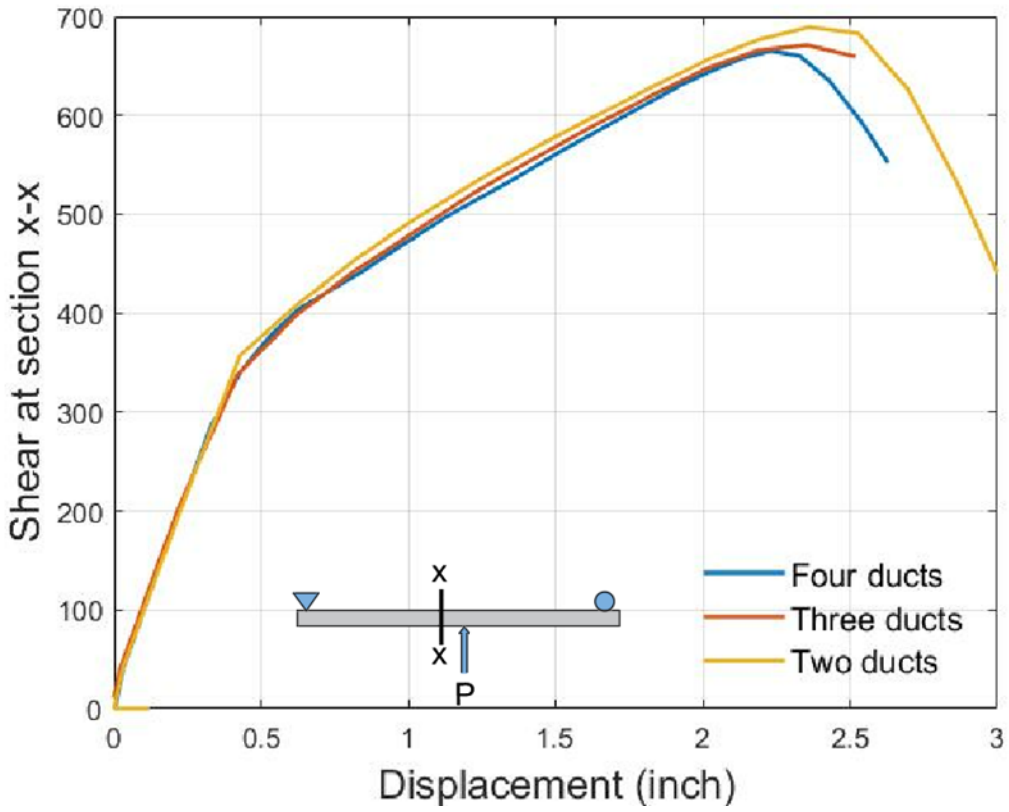

Figure 4.24: Shear-displacement response for girders with varying number of ducts

Plots of the tensile stresses at peak load at the critical girder section are shown in Figure 4.25. As observed for the experimentally tested girders, the stress contours do not high stresses in the neighborhood of the post-tensioning ducts.

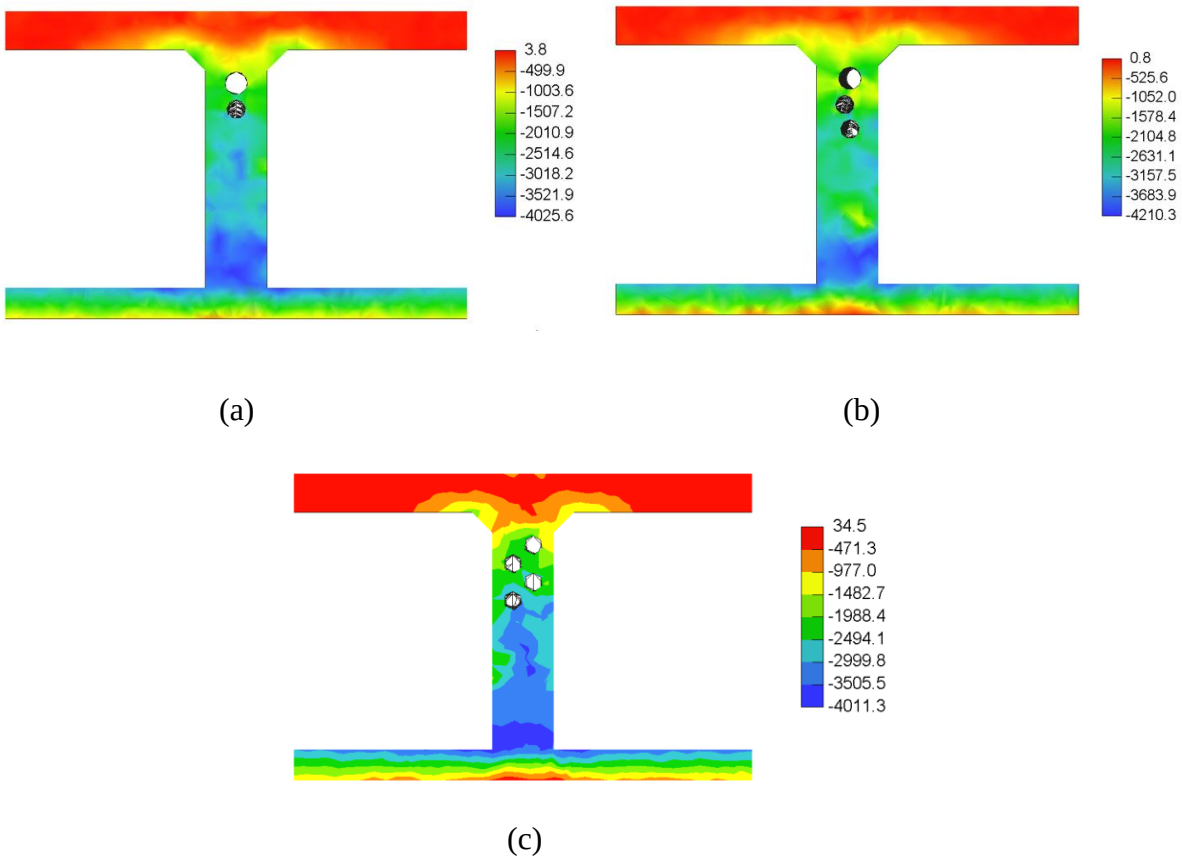

(a) (b)

(c)

Figure 4.25: Minor principal stresses (in psi) near peak load at the critical cross-section location for differing duct arrangements (a) 2 ducts; (b) 3 ducts; (c) 4 ducts

4.3.2 Effect of Duct Size

Duct size is varied to investigate whether it has an influence on the shear resistance of the girder models. In particular, three different duct sizes (D = 3, 4.5 and 6 in.) are considered in the four-duct configuration (Fig. 4.27). Apart from the size of the ducts, all parameters from section 4.3.1 have been adopted for the simulations.

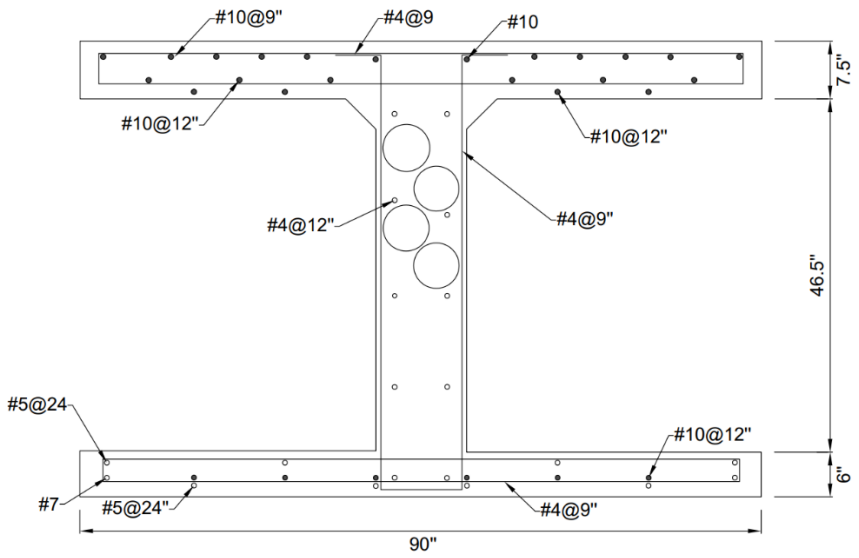

Figure 4.26: Four-duct arrangement (varying diameter *D*)

As seen when comparing the load-displacement responses in Fig. 4.27, duct diameter does not appear to influence the shear resistance behavior of the girder models. As observed in section 4.3.1, shear failure appears to be primarily governed by loss of resistance of the diagonal compression struts, particularly in the lower portion of the girder web (away from the post-tensioning ducts). This can also be seen in the contours of minimum principal stress presented in Fig. 4.28. Compressive stress is markedly higher in the lower portion of the web. A more complete analysis should consider contour plots at additional cross-section locations within the critical zone.

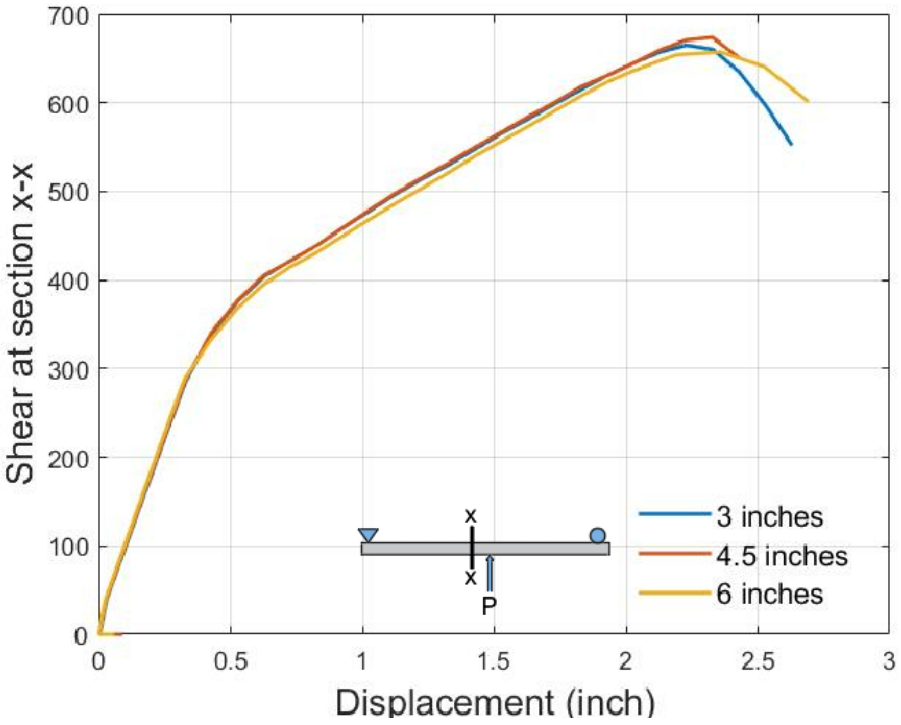

Figure 4.27: Effect of duct diameter on load-displacement behavior

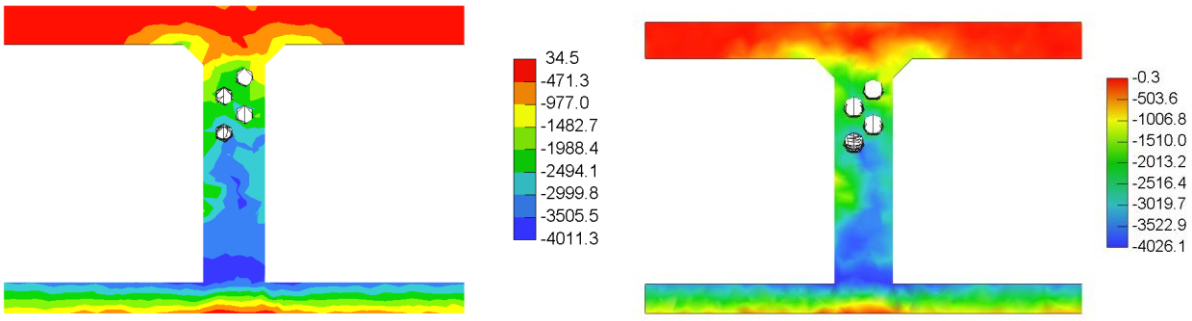

(a) (b)

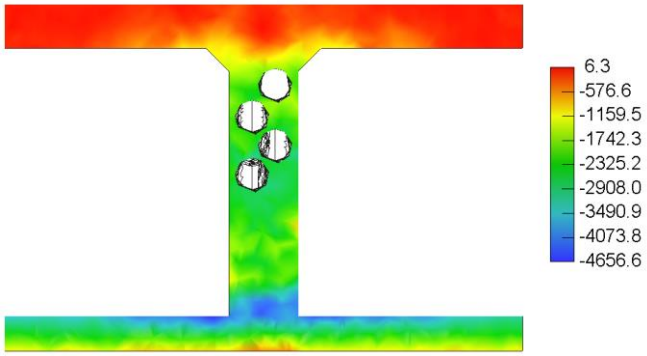

(c)

Figure 4.28: Minor principal stresses (in psi) near peak load at the critical cross-section location for varying duct diameters (a) 3 inch ducts; (b) 4.5 inch ducts; (c) 6-inch ducts

5.0 CONCLUSIONS

This research study was initiated to assess two amendments by the California Department of Transportation (Caltrans) of current AASHTO (2017) guidelines related to the determination of the shear resistance of post-tensioned (PT) concrete girders. It should be noted that Caltrans began making amendments to the AASHTO LRFD Bridge Design Specifications in 1999 to facilitate adoption of those specifications into California's bridge design practice. Two specific issues that arise from the Caltrans amendments concern the effective web width for fully grouted ducts and the number of ducts that can be bundled in a girder section. The first of these two issues directly affects the calculation of shear strength of the girder member whereas the second raises concerns about the potential adverse effects of increasing the number of ducts in a girder section.

The shear capacity of post-tensioned girders has been experimentally evaluated previously, however, the majority of these tests are either small-scale tests or comprise configurations that do not resemble typical Caltrans practice. The testing reported in this study was carried out on near full-scale cross-sections that represent typical Caltrans PT girders. Finally, given the physical and economical constraints associated with large-scale testing, it was necessary to supplement the experimental testing with numerical simulations to provide additional insight into the effect of grouted ducts in PT girders.

5.1 Summary of Research Tasks

The research objectives were accomplished through the following tasks:

(a) A prototype bridge was first identified following a review of the Caltrans bridge inventory. The selection was based on the ability of the UC Davis strong floor and reaction system to test a specimen whose depth represents either a full-scale or near full-scale bridge girder.

Reinforcing details of the specimen were modified so as to induce shear failure prior to flexural yielding of the specimen.

(b) Considering the physical constraints in the laboratory, considerable effort was dedicated to the design and construction of a reaction system, so that the imposed loading at shear failure of the specimen could be safely distributed to the strong floor.

(c) Two large-scale tests were conducted: in the first phase, the primary goal was to examine the consequence of the Caltrans amendment related to the effective web width in calculating the shear resistance of a PT girder; in the next phase, current Caltrans practice of bundling more than three ducts in some cases (which is disallowed by the AASHTO guidelines) was investigated. Additionally, given recent interest in Caltrans to reduce the standard web width of 12 inches, the testing in the second phase considered a duct with a web width of 10 inches.

(d) Finally, to further corroborate the experimental findings and extend the range of the investigations, numerical simulations were carried out using detailed finite element analysis of PT bridge girders with varying duct diameters as well as different configurations of bundled ducts.

5.2 Primary Research Findings

The primary findings from the combined experimental and numerical studies can be summarized as follows:

1. The shear resistances of both specimens were significantly higher than the corresponding shear capacities given by the AASHTO expressions for estimating the shear capacity of post-tensioned girders. As shown in Figures 3.13 and 3.16, the experimentally measured resistances are greater than the corresponding AASHTO estimates by a factor of approximately 1.65.

2. For the specimen configurations considered, the concrete contribution V_c to shear resistance varies between 15 – 25% of the nominal shear capacity (see Tables 3.2 and 3.3). The difference in V_c resulting from the Caltrans amendment and the AASHTO requirement for establishing the effective width of the web affects the nominal shear capacity of the girder by less than 5% and consequently has a minor effect in the design of PT girders with fully grouted ducts.
3. There was no visible distress around the duct region at the end of testing for specimen #1 indicating that the corrugated metal duct bonds well to the concrete and remains intact even at loads approaching shear failure of the girder. Minor to moderate distress was observed on the concrete surface along the duct lines for specimen #2, which experienced a dramatic shear failure.
4. The inclination of shear cracks for both specimens during testing varied between 25° - 30° with the angle of newly forming cracks tending to decrease with increasing load. The range of AASHTO estimates for θ, which corresponds to the angle of crack inclination at the limit state, is somewhat higher at 36° - 38° for the cases considered herein.
5. The estimates of the centroidal strain ε_s based on strain gauge measurements at various locations across the depth of the section (see Figures 3.11 and 3.14) were in reasonable agreement with the corresponding AASHTO estimates.
6. Numerical simulations using the ATENA software package were successful in reproducing the observed shear-displacement response of both specimens.
7. The numerical simulations substantiated experimental observations that there was either minor or no distress around the duct region at failure of the specimens. Based on

such post-loading observations of the test specimens, the perfect bond between the metal duct(s) and concrete appears to be a reasonable assumption in the simulations.

8. The numerical simulations appear to indicate stirrup yielding and concrete crushing within the diagonal compression field within the girder web as primary contributors to specimen failure. However, concrete crushing within the webs was not physically observed at the end of testing for both specimens. The degree of correspondence between the physically observed and numerically simulated failure mechanisms needs further examination.

5.3 Future Work

In the present study, the testing program was limited to two large-scale specimens. The specimen dimensions, reinforcement details, and boundary conditions were chosen to represent the conditions of a continuous, multi-span girder local to an interior support. Finite element modeling exercises were conducted to substantiate the experimental findings and investigate the influences of duct sizing and bundling. However, there remain needs for future work regarding the shear resistant design of PT concrete girders. These needs include:

1. Additional large-scale testing that extends the range of the investigations. By populating the test database with results from other sectors of the design parameter space, more general statements can be made regarding the resistance of PT concrete girders to shear failure. At least indirectly, additional large scale test results would allow for statistical analyses and conclusions on the repeatability of these tests.
2. Investigation of the performance of alternative duct materials for housing the prestressing steel. In particular, there is interest in using non-corrosive, flexible materials (e.g., high

density polyethylene – HDPE – materials) as smooth or corrugated ducts. Bonding between such duct materials and the surrounding concrete is one of the issues to be studied.

3. Understanding girder behavior within the bridge superstructure, including load redistribution to adjacent girders.
4. Continued validation of numerical modeling techniques (e.g., the ATENA software package used herein) through comparisons with large-scale test results. These validations should be conducted for all relevant aspects of the models and their physical counterparts (i.e., both global and local behaviors should be accurately simulated.) Such efforts provide confidence in the models and their use for parametric study. In some cases, such as the aforementioned study of the bridge superstructure, computational modeling is a rational means for understanding girder performance in its structural settings.

6.0 REFERENCES

AASHTO (2017). AASHTO LRFD Bridge Design Specifications, 8th Edition. American Association of State Highway and Transportation Officials, Washington, D.C.

Bazant, Z.P. and Oh, B.H. (1983). Crack Band Theory for Fracture of Concrete. *Materials and Structures*, RILEM 16 (3), 155–177.

Campbell, T. I. and Batchelor, B. (1981). Effective Width of Girder Web Containing Prestressing Duct. *Journal of the Structural Division,* ASCE, V. 107 (5), 733-744.

Campbell, T. I., Batchelor, B. and Chitnuyanondh, L. (1979). Web Crushing in Concrete Girders with Prestressing Ducts in the Web. *PCI Journal*, V. 24 (5), 71-87.

Červenka V, Jendele L, Červenka J. (2020), ATENAProgram documentation – Part 1: Theory. Praha: Cervenka Consulting, www.cervenka.cz.

Collins, M. P., E. C. Bentz, E. G. Sherwood, and L. Xie (2008). An Adequate Theory for the Shear Strength of Reinforced Concrete Structures." *Magazine of Concrete Research*, 60 (9): 635–650.

Hordijk, D.A. (1991). Local Approach to Fatigue of Concrete. Ph.D. Thesis, Delft University of Technology, The Netherlands.

Leonhardt, F (1969). Abminderung der Tragfähigkeit des Betons infolge stabförmiger, rechtwinklig zur Druckrichtung angeordnete Einlagen (Reduction of Concrete Compressive Strength due to Rods Inserted Perpendicularly to the Loading). Festschrift Rüsch, Berlin, Germany, 1969, pp. 71-78. (in German).

Menetrey, P. and Willam, K.J. (1995). Triaxial Failure Criterion for Concrete and its Generalization. *ACI Structural Journal,* 92 (3), 311–318

Moore, A., Williams, C., Al-Tarafany, D., Felan, J., Massey, J., Nguyen, T., Schmidt, K., Wald, D., Bayrak, O., Jirsa, J and Ghannoum, W. (2015). Shear Behavior of Spliced Post-Tensioned Girders. *Report FHWA/TX-14/0-6652-1*, University of Texas, Austin.

Muttoni, A., Burdet, O.L. and Hars, E. (2006). Effect of Duct Type on Shear Strength of Thin Webs. *ACI Structural Journal*, V. 103, No. 5, 729-735.

Ruiz, F. and Muttoni, A (2008). Shear Strength of Thin-Webbed Post-Tensioned Beams. *ACI Structural Journal*, V. 105, No. 3, 308-317.

Vecchio, F. J., and M. P. Collins (1986). The Modified Compression-Field Theory for Reinforced Concrete Elements Subject to Shear. *ACI Journal*, 83 (2): 219–231.

Wald, D.M. (2012). Experimental Investigation of Crushing Capacity of I-Girder Webs Containing Post-Tensioning Ducts. MS Thesis, University of Texas, Austin.